

AD-A281 301



ADOSR-TR 94 0411

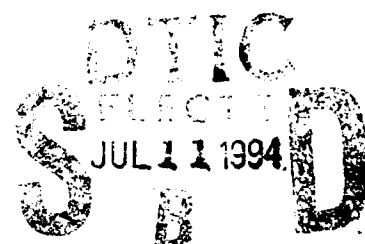
Approved for public release;
distribution unlimited.

**STRUCTURAL INTEGRITY OF INTELLIGENT
MATERIALS AND STRUCTURES**

Constitutive Modeling of Shape Memory Alloys

Final Report

May 1994



Prepared by:

Berkeley Applied Science and Engineering, Inc.
5 Third Street, Suite 530
San Francisco, CA 94103-3206
(415) 543-1600

108 20

94-20936

B A S E

DTIC QUALITY INSPECTED 2

94 2 8 046

REPORT DOCUMENTATION PAGE

Form Approved
OMB No. 0704-0160

Public reporting burden for this collection of information is estimated to average 1 hour per response, including the time for reviewing instructions, searching existing data sources, gathering and maintaining the data needed, and completing and reviewing the collection of information. Send comments regarding this burden estimate or any other aspect of this collection of information, including suggestions for reducing this burden, to Washington Headquarters Services, Directorate for Information Operations and Reports, 1215 Jefferson Davis Highway, Suite 1204, Arlington, VA 22202-4302, and to the Office of Management and Budget, Paperwork Reduction Project (0704-0160), Washington, DC 20503.

1. AGENCY USE ONLY (Leave blank)	2. REPORT DATE	3. REPORT TYPE AND DATES COVERED	
	May 1994	Technical - 93Aug01 thru 94Mar31	
4. TITLE AND SUBTITLE		5. FUNDING NUMBERS	
Structural Integrity of Intelligent Materials & Structures Constitutive Modeling of Shape Memory Alloys (u)		F49620-93-C-0028	
6. AUTHOR(S)		8. PERFORMING ORGANIZATION REPORT NUMBER	
M. Panahandeh A. Masud F. Auricchio			
7. PERFORMING ORGANIZATION NAME(S) AND ADDRESS(ES)		9. SPONSORING/MONITORING AGENCY NAME(S) AND ADDRESS(ES)	
Berkeley Applied Science & Engineering, Inc. 5 Third Street, Suite 530 San Francisco, CA 94103-3206 (415) 543-1600		Air Force Office of Scientific Research 110 Duncan Ave., Suite B115 Bolling AFB, DC 20332-0001	
11. SUPPLEMENTARY NOTES		10. SPONSORING/MONITORING AGENCY REPORT NUMBER	
12a. DISTRIBUTION/AVAILABILITY STATEMENT		12b. DISTRIBUTION CODE	
Unlimited Approved for public release; distribution unlimited.			
13. ABSTRACT (Maximum 200 words)			
<p>A full-scale application of shape memory alloys in intelligent structures requires that the complex interaction between active elements (sensors, actuators, processors) and the host material be investigated and a modeling tool to simulate the behavior of these structures be developed. This research is an effort toward this direction with the following objectives:</p> <ul style="list-style-type: none"> I) Development of a constitutive theory for pseudoelastic behavior of shape memory alloys based on phase transformation in these alloys. II) Extension of the theory to finite kinematics and developments of numerical algorithms for solution of the nonlinear pseudoelastic system. III) Formulation of a multi-director shell theory for finite element modeling of composite laminates. IV) Numerical implementation of the theory in a suitable finite element program with nonlinear capabilities. V) Simulation of cyclic loading and partial loading/unloading in shape memory alloys. 			
14. SUBJECT TERMS		15. NUMBER OF PAGES	
Sensors, Actuators, Shape Memory, Constitutive Model, Composite Laminate, Large Deformation			
16. PRICE CODE			
17. SECURITY CLASSIFICATION OF REPORT	18. SECURITY CLASSIFICATION OF THIS PAGE	19. SECURITY CLASSIFICATION OF ABSTRACT	20. LIMITATION OF ABSTRACT
UNCLASSIFIED	UNCLASSIFIED	UNCLASSIFIED	UL (UNLIMITED)

NSN 7540-01-280-5500

Standard Form 298 (Rev 2-89)
Prescribed by ANSI Std Z39-18
298-102

B A S E

**STRUCTURAL INTEGRITY OF INTELLIGENT
MATERIALS AND STRUCTURES**

Constitutive Modeling of Shape Memory Alloys

Final Report

Prepared for:

AIR FORCE OFFICE OF SCIENTIFIC RESEARCH

Contract #F49620-93-C-0028

Prepared by:

M. Panahandeh
A. Masud
F. Auricchio

Berkeley Applied Science and Engineering, Inc.
5 Third Street, Suite 530
San Francisco, CA 94103-3206
(415) 543-1600

May 1994

BASE

ACKNOWLEDGEMENT

The present research was sponsored by the Air Force Office of Scientific Research (AFOSR) under contract No. F49620-93-C-0028. The financial support of AFOSR is gratefully acknowledged. The authors are indebted to Dr. Walter F. Jones, the program manager in AFOSR for his encouragement and interest in the work. The helpful discussions with Professor Robert L. Taylor and Professor J. Lubliner of the University of California at Berkeley are gratefully acknowledged.

Accession For		137
RTIS	CRM&I	<input checked="" type="checkbox"/>
DTAC	CAB	<input type="checkbox"/>
Date Received		<input type="checkbox"/>
JUL 1 1972		<input type="checkbox"/>

RECEIVED
FEDERAL BUREAU OF INVESTIGATION
U.S. DEPARTMENT OF JUSTICE
JULY 1 1972
FBI - LOS ANGELES
A-1

BASE

CONTENTS

Abstract	i
Chapter 1: Introduction	1
1.1 Introduction	1
1.2 A brief account of thermomechanical behavior of SMA	6
Chapter 2: A Constitutive Model of SMA; Pseudoelastic Behavior and its Algorithmic Implementation	17
2.1 Introduction	17
2.2 Basic Assumptions and Continuous Time Model	17
2.3 Austenite-Martensite Phase Transformation	20
2.4 Martensite-Austenite Phase Transformation	21
2.5 Internal Loop Descriptions	21
2.6 The Kuhn-Tucker Conditions	22
2.7 Discrete Time Model and Algorithmic Implementation	24
2.7.1 Discrete equations and integration algorithm	24
2.7.2 Discrete phase transformations	26
2.7.3 Conditions for phase transformation in the discrete model	27
2.7.4 Discrete tangent tensor	27
2.7.5 Linearization of phase transition equations	29
2.8 Numerical Examples	30
Chapter 3: Finite Deformation Formulation for Shape Memory Alloys	33
3.1 Introduction	33
3.2 Phase Transformation Flow Rule	34
3.3 Constitutive Relations	35
3.4 Radial Return Algorithm	37

3.5 Boundary Value Problem	39
3.5.1 Strong Form of the Problem	40
3.5.2 Weak Form of the Problem	41
3.6 Stress Update Strategy	42
3.7 Derivation of the Consistent Tangent	43
3.8 Numerical Results	52

Chapter 4: A Finite Element Theory for Composite Laminates

 Specialized to Flat Geometries	65
4.1 Introduction	65
4.2 New Ideas Proposed in the Present Theory	67
4.3 Assumptions of the Layer-wise Shear Deformable Shell Theory	68
4.4 Kinematic Description of Multi-layered Shells	69
4.4.1 Kinematics in the context of finite element method	71
4.5 Geometric Description of Multi-layered Shells	72
4.5.1 Geometric description in the context of the finite element method	73
4.5.2 Lamina coordinate system	74
4.6 Constitutive Relations	76
4.7 Finite Element Formulation	78
4.7.1 Strong form of the problem	78
4.7.2 Weak form of the problem	79
4.7.3 Finite element stiffness matrices and load vectors	80
4.7.3.1 Stress vectors	80
4.7.3.2 Strain vectors	81
4.7.3.3 Matrix differential operators	82
4.8 Numerical Examples	84
4.9 Conclusions	91

Chapter 5: Future Research and Potential Post Applications 93

5.1 Potential Applications	94
-----------------------------------	----

References	96
-------------------	----

CHAPTER 1

1.1 Introduction

Development of intelligent material systems and structures has been followed by various government agencies and private corporations in the last decade. Intelligent structures are defined as the ones which incorporate actuators and sensors that are highly integrated into the structure and have structural functionality, as well as highly integrated control logic, signal conditioning, and power amplification electronics. Such actuating, sensing, and signal processing elements are incorporated into a structure for the purpose of influencing its mechanical, thermal, optical, chemical, electrical or magnetic characteristics.

Several technical developments have been combined to establish the potential feasibility of intelligent structures. The first is a transition to laminate materials. In the past, structures were built from large pieces of monolithic materials which were machined, forged, or formed to a final structural shape, making it difficult to incorporate any active element inside the structure. However, in the past thirty years a transition to laminated material technology has occurred. Laminated materials allow for the easy incorporation of active elements within the build up of structural forms.

Exploitation of the off diagonal terms in the material constitutive relations is a second trend which makes the development of intelligent structures promising. The full constitutive relations of a material which include characterizations of its mechanical, optical, electromagnetic, chemical, physical, and thermal properties. Normally, researchers have focused only on block diagonal terms. For example, those interested in exploiting a material for its structural benefits have focused only on the mechanical characterization, and those interested in exploiting its electrical properties have focused on the electrical characterization. However, much gain can be made by exploiting the off block diagonal terms in

the constitutive relations, which for example, couple the mechanical and electrical properties or couple mechanical and thermal properties. The characterization and exploitation of these off diagonal material relations had led to much of the progress in the creation of intelligent structures.

The third and perhaps most obvious advance has been in the electrical engineering and computer science disciplines. These include the development of microelectronics, bus architectures, switching circuitry, and fiber optic technology. Also central to the emergence of intelligent structures is the development of information processing, artificial intelligence, and control disciplines. The sum of these three developing technologies (the transition to laminated materials, the exploitation of the off-diagonal terms in material constitutive relations, and the advances in microelectronics) has created the enabling infrastructure based on which intelligent structures can develop.

A wide variety of applications exist for intelligent structure technologies. These include aeroelastic, control and maneuver enhancement, reduction of vibrations and structure borne noise, jitter reduction in precision pointing systems, shape control of plates, trusses and lifting surfaces, isolation of offending machinery and sensitive instruments, and robotic control.

For a review of the status of smart structures and technology overview, the following references may be consulted: Agnes & Silva [1992], "Aircraft Smart Structures Research in the USAF Wright Laboratory"; Crawly [1992], "Intelligent Structures, a Technology Overview and Assessment"; Lazarus & Napolitano [1993], "Smart Structures, an Overview."

Three main development areas that require further research are: (1) basic materials, (2) component devices, and (3) modeling techniques. There is a need to develop basic smart materials with improved properties and characteristics. Some of the more important features to be improved include fatigue life, fracture toughness, structural weight, required voltage, linearity, and anisotropy. These materials should be developed in order

to create improved intelligent structure component devices such as actuators and sensors. An emphasis should be placed on the use of actuator and sensor components for structural control. Accurate models need to be developed so that smart material components may be utilized effectively. Work is needed in developing constitutive relations as well as full non-linear models to meet these needs. This research is directed toward addressing some of these needs as discussed in the following sections.

In an intelligent structure, the presence of active elements (actuators, sensors, and processors) impact the host structure by increasing the mass of the system and interfering with the load path and potentially introducing new structural discontinuities which must be accommodated. This may potentially change the fatigue and fracture toughness characteristics of the host material.

The complex microscale interactions between sensors, actuators, and the host materials, and in particular the inherent material and geometric nonlinearities within intelligent material systems, must be characterized before the technology can reach its full potential.

Initial experimental investigations have indicated high strain concentration at interface between sensors and host materials. Czarnek et al. [1988] at Virginia Tech have used interference imaging for a cross-ply graphite/epoxy laminate, fabricated with a jacketed glass fiber waveguide embedded between and perpendicular to the center two plies. Strains of approximately 0.05 were indicated at the fiber-matrix boundary for an applied load equal to half the failure load of specimens tested. They concluded that these large interface strain concentrations may pose significant limits on the long term structural integrity of materials containing embedded sensor fibers.

Singh H. et al. [1991] combined Moiré interferometry and the Fourier transform fringe interpretation method to produce high resolution displacement measurement system for laminated composites with embedded sensors. Their findings show stress concentrations factors as much as 8.8 in the vicinity of fiber-host material interface. The largest character-

istic length of the influence was found to be about 11.5 times fiber diameter. These strain concentrations at sensor-host material interface warrant concern regarding micro-cracking due to various in-use loading conditions.

Other studies, Jenson [1992], have measured reduction in compression strength due to embedment, for the worst orientation, of up to 70 %. This reduction would seem to be due to the bending of load-bearing longitudinal fibers around a transverse sensory fiber, creating a prebuckled site.

These experimental results indicate the need for research work to address the mechanics that govern the complex interactions between sensors, actuators, and the host materials for smart structures. The research should consider the inherent material and geometric nonlinearities at micro and macro-scales. Fundamental understanding of these interactions will provide opportunities for further developments of intelligent materials and structures.

Shape Memory Alloys (SMA) are among candidate materials suitable for wide application in smart structures. They have the unusual material property of being able to sustain and recover large strains (of the order of 10 %) without inducing irreversible plastic deformation and to "remember" a previous configuration and return to it with a temperature change. These interesting material characteristics arise due to distinctive internal crystalline transformations with temperature and applied stress (Delaey et al. [1974]; Perkins et al. [1976]; Funakubo [1987]; Wayman and Duerig [1990]).

The growing global interest in smart material and smart structure technology in particular has prompted an increasing number of investigations of SMAs in the past decade. The result of the research has been increasingly detailed information regarding the crystalline structure of SMA materials, a greater understanding of macroscopic SMA material behavior, the development of new alloys and processing techniques, and a dramatic increase in the number of applications studied, which now span a wide range of products and devices.

The most established commercial application of SMAs, that of connectors for hydraulic

tubing in aircraft, is currently being overshadowed by the incorporation of SMAs into critical roles in a large array of applications including active vibration control of structures, heat engines, orthodontic wire and automatic switches in household appliances (Banks & Weres [1976]; Funakubo [1987]; Rogers et al. [1989]; Falcioni [1992]).

Since Nitinol's discovery in the late 1950's, a great deal of research has been reported on the behavior of shape memory alloys, possible application and the physics associated with shape memory effect. Rodgers & Robershaw [1988] have demonstrated that SMA materials can be embedded in composite structures to actively control and modify the dynamic and structural behavior of SMA hybrid composite laminates. Wayman [1990,1992,1993] discusses various practical applications. There have been several attempts to construct phenomenological models capable of representing the SMA macrobehavior. Representative works are by: Abeyaratne and Knowles [1993], Brandon and Rogers [1992], Brinson [1993], Cory and McNichols Jr. [1985], Falk and Konopka [1990], Ivshin and Pence [1993a, 1993b], Liang and Rogers [1990,1992], Muller and Xu [1991], Patoor, Eberhardt and Berveiller [1988], Tanaka et al. [1982,1985,1986,1992], Tobushi et al. [1991], Wilmanski [1993].

In a recent review article Huo and Muller [1993] discussed the nonequilibrium thermodynamics of pseudoelasticity. Finite element analysis of SMA behavior for one-dimensional applications was discussed by Brinson & Lammering [1993].

One advantage of shape memory alloys over other types of mechanical or electrical devices is that their physical configuration can be easily, precisely and repeatedly controlled by often small temperature changes. In some applications, where temperature change is in itself the motivation for movement of a mechanical device, the SMAs can be designed such that no power source is needed to activate their motion. In other cases, a single or series of SMA wires can easily and inexpensively be given a small temperature change which initiates a phase transformation and consequently results in the desired motion and/or stress. Their ability to achieve large strains near instantaneously enables the design of

structures capable of extremely large, recoverable deflections. In addition, shape memory alloys are relatively lightweight, biocompatible, easy to manufacture and have a high force to weight ratio (Wayman [1980]).

Given the variety of potential uses for SMAs and the high interest in developing new applications, the ability to accurately model and analyze structures containing SMA components via a finite element procedure is extremely attractive, and we are unaware of any existing numerical package capable of addressing 3-D thermomechanical behavior of shape memory alloys. The incorporation of the SMA numerical simulation procedure into the design stages of new products could reduce development times and costs dramatically. Since the properties of a particular alloy can be easily and drastically altered in the manufacturing process, the properties of the SMA component in a given design can be varied systematically in an automated analysis before production. This optimization procedure will enable use of shape memory alloy components with specifically tailored properties that will realize their full potential in each individual application.

1.2 A brief account of thermomechanical behavior of Shape Memory Alloys (Huo, Muller [1993])

Shape memory alloys in uniaxial tensile tests exhibit a strongly temperature-dependent behavior. At high temperatures a typical load-deformation curve is schematically shown in Figure 1.1. The behavior characterized by this (P,d) curve is called pseudoelasticity. It is elastic, because the tensile specimen returns to the origin after unloading, but it is only "pseudo" elastic, because there is a hysteresis loop.

A hysteresis loop indicates *energy dissipation* or *entropy production*, in the loading-unloading process, and therefore — from the thermodynamic point of view — the process is irreversible. In other words, during the process the specimen does not remain in equilibrium; rather it runs through non-equilibrium states for part of the process.

In the well-developed non-equilibrium thermodynamic theory, four "mechanisms" of

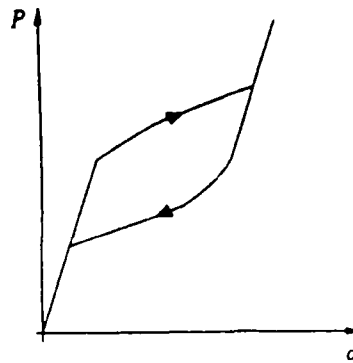


Fig. 1.1 (P,d) diagram of shape memory alloy (schematic picture)

energy dissipation are commonly investigated: *heat conduction, viscosity, diffusion and chemical reaction*. None of these is present here to a significant degree, but there is a phase transition, the so-called martensitic transformation. In the unloaded body at high temperature the crystal structure is cubic and the phase is called austenite (A). The low temperature phase has less symmetry, and it is called martensite (M). A load can force a specimen to become martensitic even at high temperatures and Figure 1.1 demonstrates this phenomenon: The specimen is in the A-phase on the elastic branch through the origin and in the M-phase on the straight steep branch on the right. The energy dissipation, or entropy production, indicated by the hysteresis occurs during the transition from one phase to the other.

Most of the works on phase transitions have been concerned with equilibrium conditions of the phase mixture. Therefore hysteresis is not considered.

Close observation of the phase transition indicates that a specimen consisting of a mixture of phases is composed of several regions of pure phase. Figure 1.2 shows a typical schematic picture of a single crystal sample of shape memory alloy in a tensile test. During the transition from one phase to the other, more and more regions of the new phase are being created and grow. At the same time the regions of the old phase decrease in number

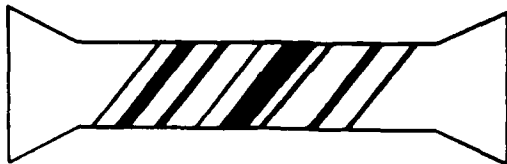


Fig. 1.2 Single crystal sample of shape memory alloy composed of regions of different phases (schematic picture)

and size and eventually they disappear completely. Therefore the transition proceeds by nucleation and growth of the new phase within the old one. Since the crystal structures and the macroscopic shapes of the two phases are different, adjacent regions of two phases do not fit each other well. Therefore additional energy is required for the coexistence of phases, similar to the surface tension of a droplet surrounded by its vapor.

In the stage of *nucleation*, this energy may be calculated approximately by the use of Eshelby's solution of inclusions [1957], if the shape of the nucleus is known, see e.g. the works of Ling & Owen [1981] and of Deng and Ansell [1990] for the case of a shape memory alloy and the work of Liu [1992] for a general discussion. Grujicic [1983], Olson & Cohen [1986] studied the motion of a single interface in a load controlled experiment and determined the influence of the defects at the interface and inside the specimen on the motion of such an interface.

However, during the transition process the places of nucleation are many, typically of order 10^3 , and they are rather randomly distributed in the sample. Therefore it is extremely difficult to obtain relevant results for the macroscopic behavior directly from the study of a single nucleus or interface and approximations are unavoidable.

Load-deformation diagrams of pseudoelasticity reported in the literature are quite different, even for single crystals of the same composition. Different authors obtain very

different results, possibly because of different methods of preparation of the specimen especially concerning the heat treatment. Therefore it seems that at the present state, it is not realistic to expect a good model which can cover all experimental results.

For an *ideal* pseudoelastic behavior the elastic branches of the two pure phases are parallel linear functions of the deformation and the hysteresis loop is composed of horizontal yield and recovery lines. Figure 1.3 shows a typical experimental plot of hysteresis and its idealized form.

We believe that ideal pseudoelasticity should be studied first, and that its study should help us to understand the essential features of pseudoelasticity. A similar situation has occurred in the field of plasticity; the linearly elastic, perfectly plastic material has the simplest plastic behavior and its study was the first step for a satisfactory description of plasticity.

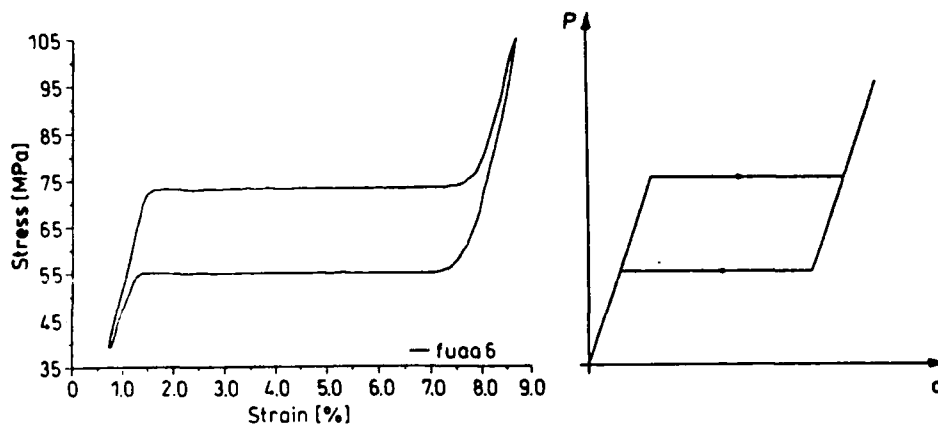


Fig. 1.3 Pseudoelasticity, left: experimental, right: ideal

1.2 The Phenomena in Ideal Pseudoelasticity

In order to fix ideas about the problems we want to investigate, we give a brief summary of the experimental results obtained by Fu and Xu [1992].

A SMA single crystal specimen (Cu Zn Al) undergoes phase transitions from austenite to martensite by cooling and from martensite to austenite by heating. Let A_f (austenite finish) denote the temperature above which the unloaded body is in the A-phase. An isothermal uniaxial deformation-controlled tensile test at $T < A_f$ exhibits ideal pseudoelastic behavior in (P,d), (d,T) and (P,T) diagrams. We proceed to discuss all three of them.

First the (P,d) diagram: In this diagram the loading-unloading curve consists of two parallel, linearly elastic branches and horizontal yield and recovery lines in-between. If we interrupt the yield before it arrives at the second elastic branch and proceed to decrease deformation, the state of the specimen first moves down steeply into the hysteresis loop along a line parallel to the two elastic branches, and then begins to recover at a constant load as shown in Figures 1.4.a and 1.4.c. Similarly Figures 1.4.b and 1.4.d show the internal yield after the recovery process was interrupted. It seems that there exists a diagonal line inside the hysteresis loop, as indicated by the dashed lines in Figures 1.4.c and 1.4.d which determines the turning points of the internal loading-unloading process. We shall call this line the *diagonal*.

If we interrupt the yield or the internal yield and unload, but reload before we arrive at the diagonal, the reloading line is identical to the unloading line. The specimen will resume the yield however when it returns to the load where the yield was interrupted before, as if it had remembered that load. A similar behavior is recorded when we interrupt the recovery process. We call the steep lines inside the hysteresis loop the *internal elastic lines* and the fact that the specimen yields or recovers only at the load at which it previously crossed the diagonal we shall refer to as history dependence. Figure 1.5 illustrates this complex behavior inside the hysteresis loop.

When the temperature is increased both the yield and recovery loads, P_y and P_r , respectively, increase linearly with temperature. However, the difference, $P_y - P_r$, and

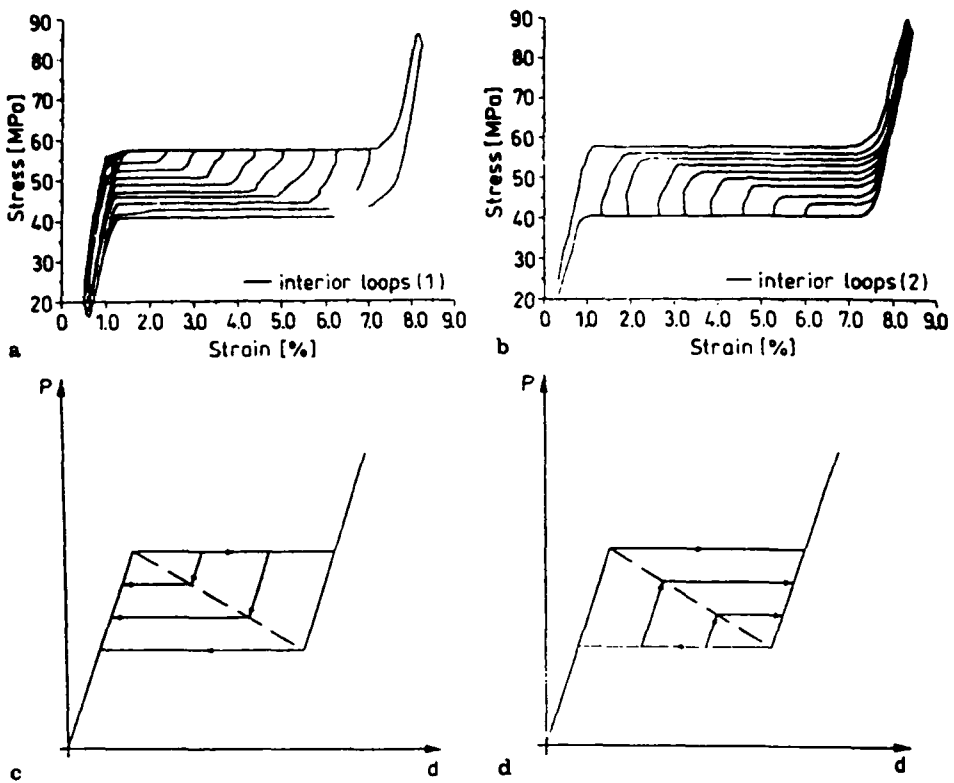


Fig. 1.4 Internal recovery and yield. The diagonal. Top: experimental, bottom: ideal

the transformation strain ε_L , which is the horizontal distance of the two elastic branches, remain constant. Thus the size of the hysteresis, i.e., $(P_y - P_r)\varepsilon_L$, is independent of the temperature, see Figure 1.6.

Figure 1.7 illustrates how the history dependence is influenced by a change of temperature. The state of the specimen has first arrived at the point X_3 by yield and elastic unloading at temperature T_1 , through $X_1 \rightarrow X_2 \rightarrow X_3$. Then the specimen is heated to T_2 at fixed deformation and it remains at X_3 . Now upon increasing the deformation the state moves first elastically to X_4 and then begins to yield at a load higher than the previous one. The dashed lines indicate the yield and recovery lines of the body at T_2 .

Second the (d,T) diagram: This diagram is taken by changing the temperature of the specimen which is under a fixed load. We neglect thermal expansion, so that the

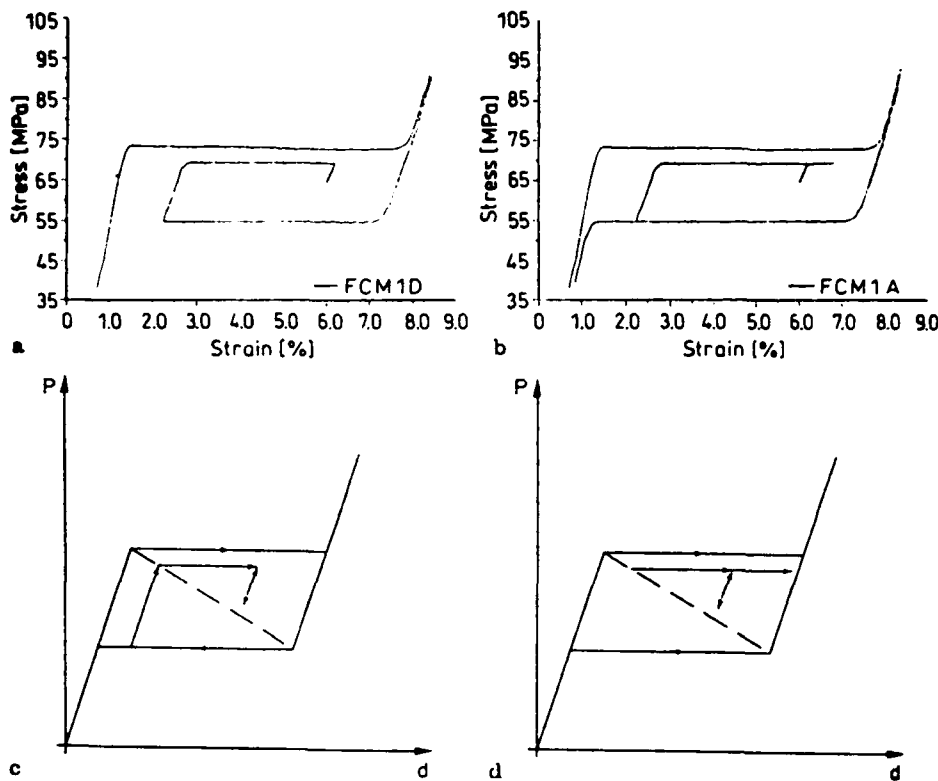


Fig. 1.5 Internal elasticity and history dependence. Top: experimental, bottom: ideal.

(d,T) diagram exhibits two horizontal lines, of which the higher one is for the M-phase and the lower one for the A-phase, and two vertical jumps where the phase transitions occur. Similar to the (P,d) diagram, internal jumps are observed as shown in Figures 1.8.a and 1.8.c, and they determine a line, the dashed line in the figure, inside the hysteresis loop, which corresponds to the diagonal in Figure 1.4. Figures 1.8.b and 1.8.d show the thermal path which is obtained by interrupting the jump from the A-phase to the M-phase, then heating and re-cooling the sample before it arrives at the diagonal. The state of the specimen moves back and forth along the same horizontal path.

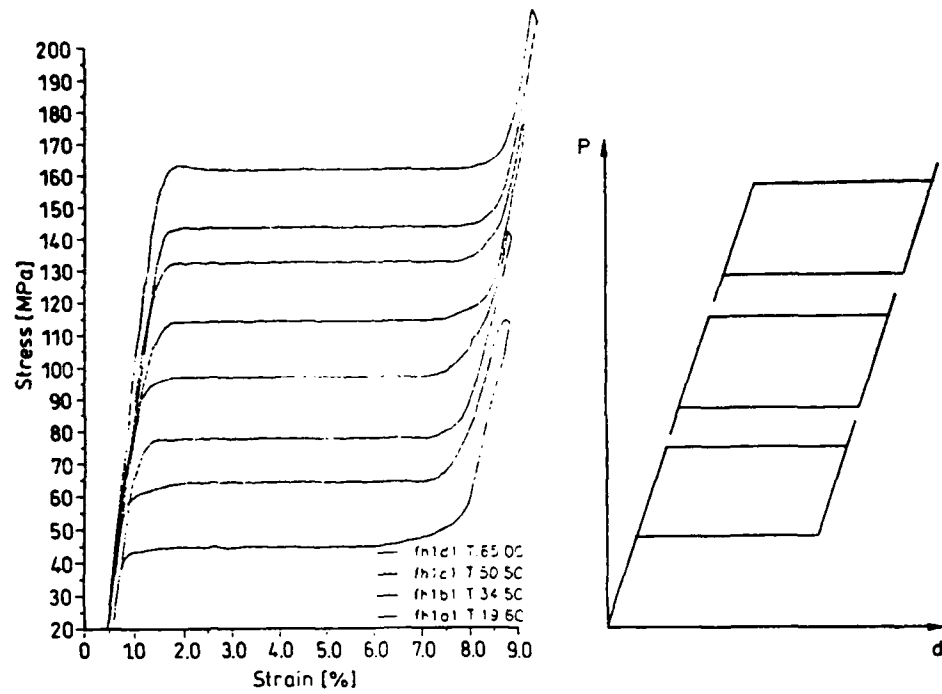


Fig. 1.6 Temperature dependence of the hysteresis, left: experimental, right: ideal

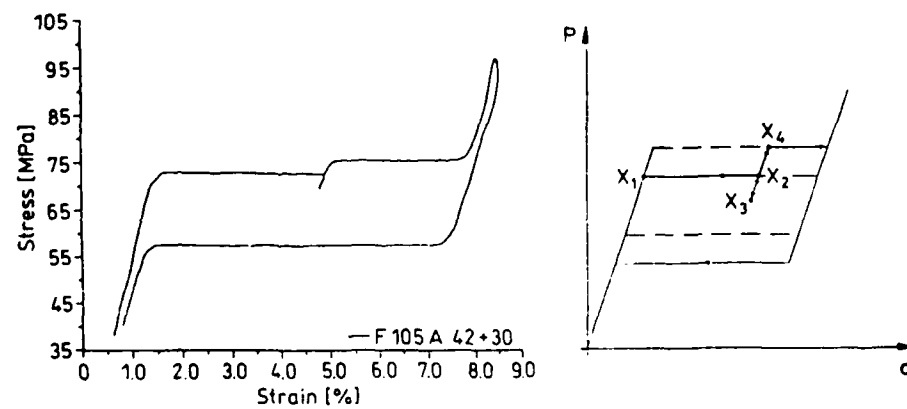


Fig. 1.7 History dependence of a temperature change, left: experiment, right: ideal

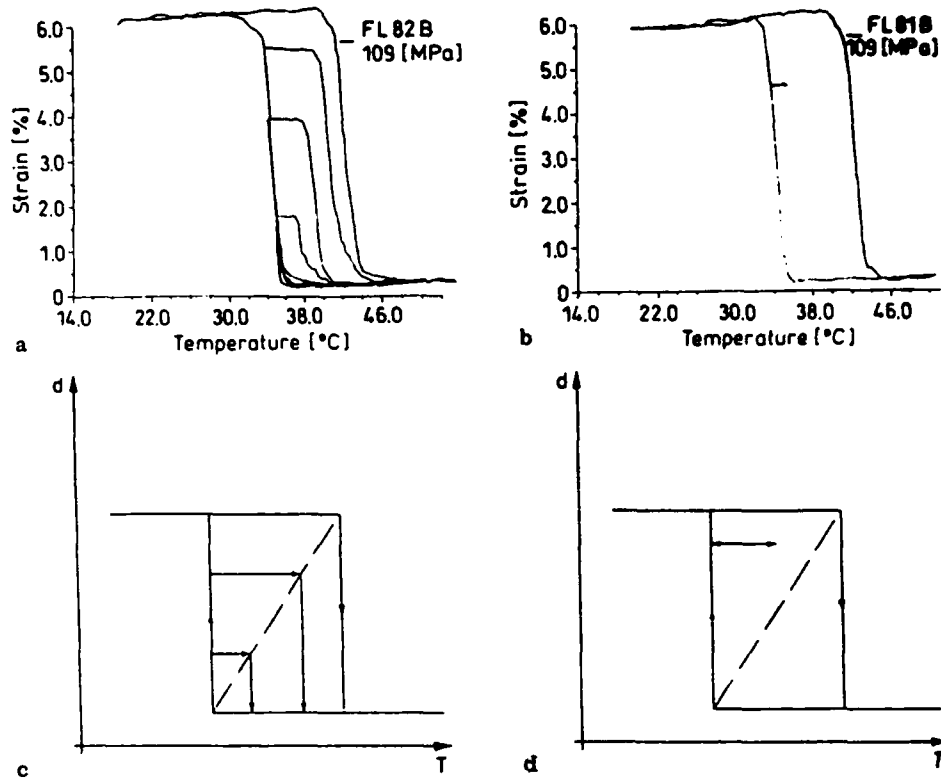


Fig. 1.8 Internal jumps and thermal path. Top: experiment, bottom: ideal

Third, the (P,t) diagram: Here we keep d constant and monitor the load as the temperature is changed. Again, ignoring the tendency for thermal expansion we obtain two horizontal lines; the lower one is for the M-phase, while the higher one is for the A-phase. The transition from M to A with increasing temperature is a straight line inclined to the T-axis, and there is a higher parallel line for the reverse transition, see Figure 1.9.

By interrupting the $A \rightarrow M$ transition and increasing temperatures the state of the specimen moves horizontally into the hysteresis loop on a reversible path as indicated in Figures 1.9.b and 1.9.d. When the temperature is lowered, interrupting the $M \rightarrow A$ transition, and the lowering proceeds far enough, there is again evidence of a line dashed

in Figures 1.9.c and 1.9.d, which corresponds to the diagonal of Figure 1.4. On that line the specimen begins the phase transition inside the hysteresis loop and parallel to the outer transition lines as shown in Figures 1.9.a and 1.9.c.

The word pseudoelasticity often refers only to the behavior in the (P,d)-diagrams obtained by $T - > A_f$. However, if the load is reasonably big, the M-phase obtained in a (d,T) experiment is of only one variant, and we may treat (d,T)-diagrams and (P,T)-diagrams by using the same approach as for the (P,d)-diagrams. We may even construct the (d,T)- and (P,t)-diagrams directly from a series of (P,d)-diagrams obtained at different temperatures.

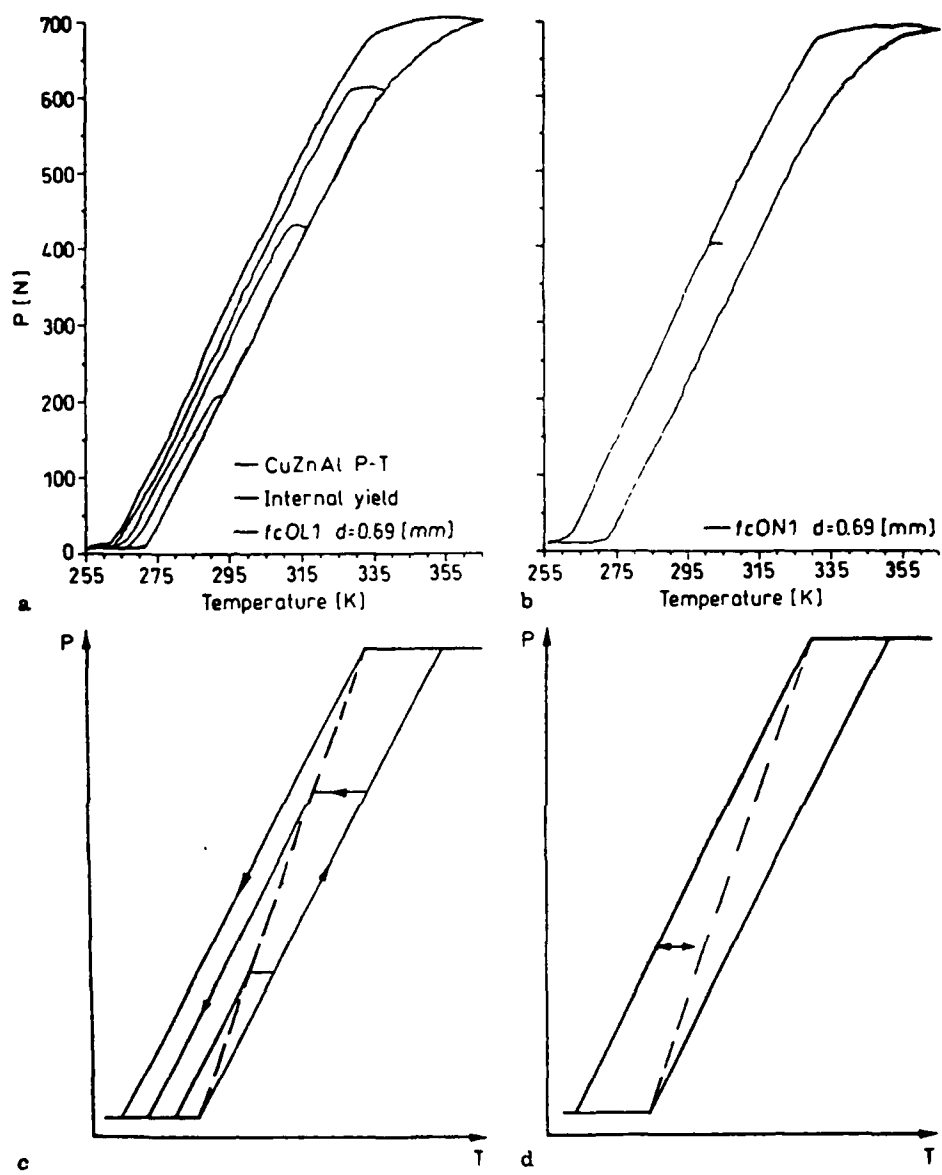


Fig. 1.9 The (P,T)-diagram. Top: experiment, bottom: ideal.

CHAPTER 2

A CONSTITUTIVE MODEL OF SHAPE MEMORY ALLOYS: PSEUDOELASTIC BEHAVIOR AND ITS ALGORITHMIC IMPLEMENTATION

2.1 Introduction

The purpose of the present development is to model the so-called pseudo-elastic behavior, represented in Figures 1.3 and 1.4 which occurs in shape memory alloys (SMA) under stress loading-unloading pattern at constant temperature. In particular we will present a constitutive model able to predict the stress-induced phase transformation from austenite to martensite during loading and the reverse transformation from martensite to austenite under unloading. We are also concerned with an appropriate description of the material behavior when incomplete transformations occur. These incomplete transformations usually induce internal loops, as qualitatively represented in Figures 1.4 and 1.5.

Since the present discussion is limited only to the pseudo-elastic behavior of shape memory alloys, we consider only iso-thermal processes.

The present section is organized as follow: we start discussing the basic assumptions and describing the continuous model, with the appropriate phase transitions. We present the corresponding discrete time model and discuss the relative algorithmic implementation, based on the use of a radial return map scheme for the integration of the constitutive equations. We also present the form the algorithmic tangent consistent with the discrete model. We conclude the paper with some numerical examples.

2.2 Basic Assumptions and Continuous Time Model

Limiting the discussion to the realm of small deformations, we may split the total strain

ϵ into an elastic component ϵ^{el} , and an inelastic component ϵ^i :

$$\epsilon = \epsilon^{el} + \epsilon^i \quad (2.1)$$

The inelastic component ϵ^i is assumed to be induced by possible phase transformations the material may undergo. To simplify the notation, the dependency of the variables on the time t is not explicitly stated. As usual, we may also split the stress σ and the strain ϵ in the volumetric and the deviatoric components:

$$\sigma = s + p \mathbf{1} \quad (2.2)$$

$$\epsilon = e + \frac{1}{3} \theta \mathbf{1} \quad (2.3)$$

where: $p = \frac{1}{3} \text{tr}(\sigma) \mathbf{1}$ is the pressure and $\theta = \text{tr}(\epsilon)$ is the volume change. In particular, recalling equation 2.1 we may split both the elastic and the inelastic strain into the volumetric and the deviatoric components:

$$\epsilon = (e^{el} + e^i) + \frac{1}{3} (\theta^{el} + \theta^i) \mathbf{1} \quad (2.4)$$

Basic assumptions under which we develop the model are:

- the phase transformations depend only on the deviatoric part of the stress and affect only the deviatoric part of the strain,
- in the absence of phase transformations the material has a linear elastic behavior.

Accordingly, $\theta^i = 0$ and the elastic relations may be written as:

$$p = K \theta \quad (2.5)$$

$$s = 2G e^{el} = 2G (e - e^i) \quad (2.6)$$

where K is the bulk modulus and G is the shear modulus. To be consistent with the notation usually adopted in the development of uniaxial model for SMA (Liang & Rogers [1990], Brinson[1993]), we rescale the inelastic contribution:

$$e^i = e_L^i x \quad (2.7)$$

where e_L^t is a material parameter, measurable experimentally and related to the so-called *maximum residual strain under uniaxial state* ε_L through the relation:

$$e_L^t = \sqrt{\frac{3}{2}}\varepsilon_L \quad (2.8)$$

The evolutionary equation for \dot{x} is assumed in the form:

$$\dot{x} = \dot{\xi} n \quad (2.9)$$

where:

$$n = \frac{s}{\|s\|} \quad (2.10)$$

is a unit vector in the stress direction. In plasticity literature, n is a unit vector perpendicular to the yield function. ξ is a scalar internal variable representing the martensite fraction. A super-posed dot indicates time derivative. Due to the interpretation of ξ , we require that $0 \leq \xi \leq 1$ and

$$\begin{cases} \xi = 0 \Leftrightarrow \text{the material is all austenite,} \\ \xi = 1 \Leftrightarrow \text{the material is all martensite,} \end{cases} \quad (2.11)$$

We are now left with the need of describing the kinetics of the phase transformations, i.e. we have to specify the rules for the activation and evolution of the phase transformations. Clearly, we have two different transformations to consider:

1. production of martensite, which means conversion of austenite into martensite ($A \rightarrow M$),
2. production of austenite, which means conversion of martensite into austenite ($M \rightarrow A$).

It has been shown experimentally that under uniaxial loading conditions, each phase transformation occurs within an appropriate range of stresses; in particular, indicating with σ the uniaxial stress, we have:

$$\begin{aligned} \sigma_{M_0} \leq \sigma \leq \sigma_{M_f}, \quad \dot{\sigma} > 0 &\Rightarrow A \rightarrow M \\ \sigma_{A_f} \leq \sigma \leq \sigma_{A_0}, \quad \dot{\sigma} < 0 &\Rightarrow M \rightarrow A \end{aligned} \quad (2.12)$$

where it is clearly stated that the conversion of austenite into martensite ($A \rightarrow M$) occurs during loading, while the conversion of martensite into austenite ($M \rightarrow A$) occurs under unloading.

Recalling that the transformations are assumed to be only function of the deviatoric part of the stress, we may generalize the concept of uniaxial stress range using a J2-type norm where J_2 is the second invariant of the deviatoric part of the stress. In particular, we set:

$$S = \|s\| = \sqrt{s \cdot s} = \sqrt{2 J_2} \quad (2.13)$$

and as conditions for the phase transformations we require:

$$\begin{aligned} S_{M_f} \leq S \leq S_{M_s}, \quad \dot{S} > 0 &\Rightarrow A \rightarrow M \\ S_{A_f} \leq S \leq S_{A_s}, \quad \dot{S} < 0 &\Rightarrow M \rightarrow A \end{aligned} \quad (2.14)$$

The three-dimensional S-bounds are related to the uniaxial σ -bounds through the relations:

$$\begin{aligned} S_{M_f} &= \sqrt{\frac{3}{2}\sigma_{M_f}}, \quad S_{M_s} = \sqrt{\frac{3}{2}\sigma_{M_s}} \\ S_{A_f} &= \sqrt{\frac{3}{2}\sigma_{A_f}}, \quad S_{A_s} = \sqrt{\frac{3}{2}\sigma_{A_s}} \end{aligned} \quad (2.15)$$

2.3 Austenite-Martensite Phase Transformation

We assume a linear variation of the martensite fraction ξ from 0 to 1 within the stress range $[S_{M_s}, S_{M_f}]$, under loading conditions. Accordingly, the following equation must be identically satisfied:

$$\mathcal{F}_{AM}(\xi) = \xi - \frac{1 - \xi^p}{2} \left[\frac{2S - K_{AM}}{H_{AM}} \right] - \frac{1 + \xi^p}{2} = 0 \quad (2.16)$$

where:

$$K_{AM} = S_{M_f} + S_{M_s}$$

$$H_{AM} = S_{M_f} - S_{M_s}$$

and ξ^p is the maximum value obtained by the martensite fraction during the previous (reverse) martensite-austenite transformation.

2.4 Martensite-Austenite Phase Transformation

We assume a linear variation of the martensite fraction ξ from 1 to 0 within the stress range $[S_{A_f}, S_{A_i}]$, under unloading conditions. Accordingly, the following equation must be identically satisfied:

$$\mathcal{F}_{MA}(\xi) = \xi - \frac{\xi^p}{2} \left[\frac{-2S + K_{MA}}{H_{MA}} + 1 \right] = 0 \quad (2.17)$$

where:

$$K_{MA} = S_{A_f} + S_{A_i}$$

$$H_{MA} = S_{A_f} - S_{A_i}$$

and ξ^p is the maximum value obtained by the martensite fraction during the previous austenite-martensite transformation:

2.5 Internal Loop Descriptions

In order to have a correct description of the internal loops for the case in which incomplete transformations occur, we modify the range of the transformation depending on the value of the martensite fraction during the previous transformation.

For example (referring to Figures 2.5.1 and 2.5.2) for the case of conversion of austenite into martensite, we set the range within which the transformation occurs as:

$$V_{M_s} = \xi^p S_{A_i} + (1 - \xi^p) S_{M_s}, \quad (2.18)$$
$$V_{M_f} = \xi^p S_{A_f} + (1 - \xi^p) S_{M_f},$$

where ξ^p is the value attained by the martensite fraction during the previous reverse transformation (i.e., during the conversion of martensite into austenite). For the case of conversion of martensite into austenite we similarly set:

$$V_{A_s} = \xi^p S_{A_f} + (1 - \xi^p) S_{M_s}, \quad (2.19)$$
$$V_{A_f} = \xi^p S_{A_i} + (1 - \xi^p) S_{M_f},$$

where ξ^p is the value attained by the martensite fraction during the previous reverse transformation (i.e. during the conversion of austenite into martensite).

2.6 The Kuhn-Tucker Conditions

Let functions $\mathcal{F}_{AM}(\xi)$ and $\mathcal{F}_{MA}(\xi)$ be the criteria for ($A \rightarrow M$) and ($M \rightarrow A$) phase transformations, respectively, similar to yield function in plasticity. In the rate independent constitutive relations for SMA, the requirement that $\dot{\xi} < \infty$ necessitates:

$$\mathcal{F}^*(\xi) = 0 \leftrightarrow \mathcal{F}_{n+1}^* = 0 \quad (2.20)$$

where

$$\mathcal{F}^*(\xi) = \begin{cases} \mathcal{F}_{MA}(\xi) & \Leftrightarrow \text{for } M \rightarrow A, (\dot{S} > 0) \\ \mathcal{F}_{AM}(\xi) & \Leftrightarrow \text{for } A \rightarrow M, (\dot{S} < 0) \end{cases} \quad (2.21)$$

and $S = \|s\| = \sqrt{s : s} = \sqrt{2 J_2}$. This is the transformation criteria of rate-independent SMA. The transformation criteria and the loading/unloading conditions can be expressed in Kuhn-Tucker form as follows.

CASE 1. Austenite \rightarrow Martensite transformation

$$\mathcal{F}_{AM}(\xi) \leq 0, \dot{\xi} \geq 0; \text{ iff } \dot{\sigma} > 0 \text{ and } \sigma \leq \sigma^* \quad (2.22)$$

where

$$\sigma^* = \sigma_M, \quad (\text{complete transformation})$$

$$\sigma^* = V_M, \quad (\text{incomplete transformation})$$

σ_M , and V_M , are critical stresses for austenite to martensite transformations corresponding to outer and inner hysteresis loops respectively.

CASE 2. Martensite \rightarrow Austenite transformation

$$\mathcal{F}_{MA}(\xi) \geq 0, \dot{\xi} \leq 0; \text{ iff } \dot{\sigma} < 0 \text{ and } \sigma \geq \hat{\sigma} \quad (2.23)$$

where

$$\hat{\sigma} = \sigma_A, \quad (\text{complete transformation})$$

$$\hat{\sigma} = V_A, \quad (\text{incomplete transformation})$$

σ_A , and V_A , are critical stresses for martensite to austenite transformations corresponding to outer and inner hysteresis loops respectively.

Combining the above expressions, we have

$$|\mathcal{F}^*(\xi)| > 0 \Rightarrow \dot{\xi} = 0 \quad (2.24)$$

and

$$|\dot{\xi}| > 0 \Rightarrow \mathcal{F}^*(\xi) = 0 \quad (2.25)$$

These two conditions (as in plasticity) express the physical requirements that the stress must be admissible and the phase transformation, in the sense of a non-zero martensite fraction rate $\dot{\xi} \neq 0$ can take place only on the phase transformation surfaces $\partial\mathcal{F}^*(\xi)$. Within the context of plasticity, these conditions are classical in the convex mathematical programming literature and go by the name of Kuhn-Tucker conditions. These two equations, (2.24, 2.25) result in

$$\mathcal{F}^*(\xi) \dot{\xi} = 0 \quad (2.26)$$

In computational plasticity literature, this equation is referred to as the “consistency condition.”

We can define the phase transformation surface (known as the yield surface in plasticity) as

$$\partial\mathcal{F}^*(\xi(s)) = \{\boldsymbol{\sigma} \in \mathcal{R} | \mathcal{F}^*(\xi(s)) = 0\} \quad (2.27)$$

For the case when the state lies on the phase transformation surface

$$|\dot{\xi}| > 0 \text{ only if } \dot{\mathcal{F}}^*(\xi(s)) = 0 \quad (2.28)$$

and set

$$|\dot{\xi}| > 0 \text{ if } \begin{cases} \dot{\mathcal{F}}_{AM}(\xi) & < 0 \\ \dot{\mathcal{F}}_{MA}(\xi) & > 0 \end{cases} \text{ or} \quad (2.29)$$

We have an additional condition.

$$\dot{\mathcal{F}}^*(\xi) \dot{\xi} = 0 \quad (2.30)$$

This condition is referred to as the "persistency condition," and corresponds to the physical requirement that in order for $\dot{\xi}$ to be non-zero (i.e., $|\dot{\xi}| > 0$), the stress state $\sigma \in \partial\mathcal{F}^*(\xi(s))$ must "persist" on $\partial\mathcal{F}^*(\xi(s))$ so that $\dot{\mathcal{F}}^*(\xi) = 0$.

2.7 Discrete Time Model and Algorithmic Implementation

We now present the discrete time counterpart for the model discussed above, paying particular attention to an implementation within a radial return map algorithm. The form of the tangent tensor consistent with the discrete model is also addressed.

2.7.1 Discrete Equations and Integration Algorithm

From a computational standpoint we treat the non-linear behavior of a material as a *strain driven* problem, since in a finite element implementation the stress history is computed from the strain history by an integration technique, such as a return mapping algorithm. Accordingly, we now introduce a discrete counterpart of the equations presented earlier and review the integration algorithm.

Let $[0, T] \subset \mathcal{R}$ be the time interval of interest and consider two time values within it, say t_n and $t_{n+1} > t_n$, such that t_{n+1} is the first time value of interest after t_n . To minimize the appearance of subscripts (and to make the equations more readable), we introduce the convention:

$$\mathbf{a}_n = \mathbf{a}(t_n), \quad \mathbf{a} = \mathbf{a}(t_{n+1})$$

where \mathbf{a} is any generic quantity. Accordingly, in the discrete time setting the subscript n indicates a quantity evaluated at time t_n , while no subscript indicates a quantity evaluated at time t_{n+1} .

We assume that the solution is known at time t_n and given by the state:

$$\{\mathbf{s}_n, \mathbf{e}_n, \mathbf{x}_n\} \quad (2.31)$$

We wish to compute the solution at time t_{n+1} , given the strain \mathbf{e} . Using a backward Euler integration formula for the scaled inelastic strain, we obtain:

$$\mathbf{x}_{n+1} = \mathbf{x}_n + \lambda \mathbf{n} \quad (2.32)$$

where

$$\lambda = \int_{t_n}^{t_{n+1}} \dot{\xi} dt \Rightarrow \xi = \xi_n + \lambda \quad (2.33)$$

Substitution of equations (2.29) and (2.30) into equation (2.5) yields:

$$\mathbf{s} = 2G[\mathbf{e} - e_L^t \mathbf{x}_n] - 2Ge_L^t \lambda \mathbf{n} \quad (2.34)$$

In the above, λ is an unknown quantity and is computed by means of an integration algorithm, such as a return mapping. Initially suggested by Maenchen and Sack [1964], the return mapping algorithm provides an efficient and robust integration scheme, based on a discrete enforcement of the limit equation. It belongs to the family of elastic-predictor inelastic-corrector algorithms and, hence, is a two part algorithm. In the first part, a purely elastic trial state is computed; in the second, if the trial state violates the material model constitutive equation, a correction is computed using the trial state as initial condition and applied such that the final state is fully consistent with the discrete model. The algorithm has been widely studied (Nagtegaal [1982], Simo & Taylor [1985], Simo & Hughes [1993]) as has its stability (Krieg & Krieg [1977], Simo & Govindjee [1991]). Additional discussion of the algorithm and its theoretical implication can be found in the literature.

We shall now discuss the two steps of the algorithm in more details.

- *Trial state:* we assume that in the interval $[t_n, t_{n+1}]$ no phase transformation occurs (i.e. $\mathbf{x} = \mathbf{x}_n$, which implies: $\lambda = 0$). As a result, we have as trial values:

$$\lambda^{tr} = 0 \quad (2.35)$$

$$\mathbf{x}^{tr} = \mathbf{x}_n \quad (2.36)$$

$$\mathbf{s}^{tr} = 2G[\mathbf{e} - e_L^t \mathbf{x}_n] \quad (2.37)$$

If the elastic trial state is admissible, i.e. it does not satisfy the conditions for a phase transformation, then it represents the new solution at t_{n+1} and the second part of the algorithm is skipped. If the elastic trial state is not admissible, a correction has to be performed, i.e. the phase transformation must be taken into account to determine the real solution state.

- *Inelastic correction:* enforcing the satisfaction of the phase transformation model, the parameter λ may be computed, as shown for both transformations ($A \rightarrow M$ and $M \rightarrow A$) later. Equations (2.32) and (2.34) can be now rewritten in terms of the trial state and λ :

$$\mathbf{z} = \mathbf{z}^{tr} + \lambda \mathbf{n} \quad (2.38)$$

$$\mathbf{s} = \mathbf{s}^{tr} - 2G e_L^t \lambda \mathbf{n} \quad (2.39)$$

which allow us to compute the inelastic solution. Since the phase transformations occur within specific upper and lower bound, before updating the solution with the inelastic one described in equations (2.31) and (2.32), it is important to test that such solution is still in the range of the phase transformation.

For both transformations considered in this work, the parameter λ may be computed solving only a scalar equation. In fact, we observe that \mathbf{s} is by definition in the \mathbf{n} -direction, i.e., $\mathbf{s} = \|\mathbf{s}\| \mathbf{n}$. Consequently, a scalar relation between the norms of \mathbf{s} and \mathbf{s}^{tr} may be generated:

$$S = \|\mathbf{s}\| = \|\mathbf{s}^{tr}\| - 2G e_L^t \lambda = S^{tr} - 2G e_L^t \lambda \quad (2.40)$$

2.7.2 Discrete Phase Transformations

Substitution of equations 2.30 and 2.34 into the constitutive equations for both the transformations returns the corresponding discrete models in the form:

$$\mathcal{F}_{AM} = \xi_n + \lambda - R_{AM} (S^{tr} - 2G e_L^t \lambda) + \frac{R_{AM} K_{AM}}{2} - \frac{1 + \xi^p}{2} = 0 \quad (2.41)$$

$$\mathcal{F}_{MA} = \xi_n + \lambda - R_{MA} (S^{tr} - 2G e_L^t \lambda) + R_{MA} S_{A_f} = 0 \quad (2.42)$$

where:

$$R_{AM} = \frac{1 - \xi^p}{H_{AM}}, \quad R_{MA} = -\frac{\xi^p}{H_{MA}} \quad (2.43)$$

Due to the linearity of such equations, the parameter λ may be computed in closed form for both the transformations and it is given by:

$$A \rightarrow M \Rightarrow \lambda = \frac{R_{AM} S^{tr} + \frac{1+\xi^p}{2} - \frac{R_{AM} K_{AM}}{2} - \xi_n}{1 + 2 G e_L^t R_{AM}} \quad (2.44)$$

$$M \rightarrow A \Rightarrow \lambda = \frac{K_{MA} (S^{tr} - S_{A_f}) - \xi_n}{1 + 2 G e_L^t R_{MA}} \quad (2.45)$$

2.7.3 Conditions for the Activations of the Phase Transformations in the Discrete Model

The conditions for the activations of the phase transformations described in Section 2.5 for the continuous time model must now be rewritten for the corresponding discrete time model. The first test we perform is a check on the loading-unloading condition, which in a discrete model can be rewritten as:

$$\begin{aligned} S^{tr} > S_n &\Rightarrow \text{loading} \Rightarrow \text{possible } A \rightarrow M \text{ transformation} \\ S^{tr} < S_n &\Rightarrow \text{unloading} \Rightarrow \text{possible } M \rightarrow A \text{ transformation} \end{aligned} \quad (2.46)$$

After checking which transformation is possibly active, we compute the corresponding λ parameter (accordingly to equations 2.38 or 2.39) and check that the final inelastic candidate state still satisfied, it means that the final state is still in a phase transition range and we can update the solution.

2.7.4 Discrete Tangent Tensor

We address the form of the tangent tensor, consistent with the discrete model. The use of a consistent tangent tensor preserves the quadratic convergence of a Newton method, which we adopt for the incremental solution of a finite element scheme. We start from the

linear elastic relation between s and e :

$$s = 2G [e - e_L^t \mathbf{x}_n] - 2G e_L^t \lambda n \quad (2.47)$$

and by linearization we obtain:

$$ds = 2G de - 2G e_L^t d\lambda n - 2G e_L^t \lambda dn \quad (2.48)$$

Keeping in mind that:

$$\mathbf{n} = \frac{s}{\|s\|} = \frac{s}{[(s : s)^{\frac{1}{2}}]} \quad (2.49)$$

we can compute its variation:

$$dn = \frac{1}{\|s\|} [\mathbf{I} - (\mathbf{n} \otimes \mathbf{n})] ds = \frac{\mathbf{N}}{\|s\|} ds \quad (2.50)$$

where the fourth order tensor \mathbf{N} is the orthogonal projection operator on the plane with unit normal n , such that:

$$\mathbf{N}n = 0, \quad \mathbf{N}\mathbf{N} = \mathbf{N} \quad (2.51)$$

Accordingly, equations 2.41 can be rewritten as:

$$[\mathbf{I} + a\mathbf{N}] ds = 2G de - 2G e_L^t d\lambda n \quad (2.52)$$

where:

$$a = \frac{2G e_L^t \lambda}{\|s\|}$$

The equation can be solved for ds :

$$ds = 2G [\mathbf{I} + b\mathbf{N}] de - 2G e_L^t d\lambda n \quad (2.53)$$

where:

$$b = -\frac{a}{1+a}$$

Assuming that from the linearization of the phase transformation equation we obtain a relation of the type $d\lambda = A[\mathbf{n} : de]$ (as we will prove in the next section), we can get the

incremental relation between the total stress σ and the total strain ϵ , consistent with the discrete model:

$$d\sigma = D_{disc} d\epsilon \quad (2.54)$$

where the algorithmic tangent tensor is given by:

$$D_{disc} = K(\mathbf{1} \otimes \mathbf{1}) + 2G(1 - C)\mathbf{I}_{dev} + 2G(C - A)(\mathbf{n} \otimes \mathbf{n})$$

where

$$\mathbf{I}_{dev} = \mathbf{I} - \frac{1}{3}(\mathbf{1} \otimes \mathbf{1}) \quad (2.55)$$

We recall that A comes from the linearized limit equation for the specific material model, while:

$$C = \frac{2Ge_L^t \lambda}{S^{tr}}$$

2.7.5 Linearization of the Phase Transition Equations

We start form the discrete equation for the austenite-martensite phase transformation:

$$\mathcal{F}_{AM}(\xi) = \xi_n + \lambda - R_{AM} S + \frac{R_{AM} K_{AM}}{2} - \frac{1 + \xi^p}{2} = 0 \quad (2.56)$$

and by linearization we get:

$$d\mathcal{F}_{AM} = d\lambda - R_{AM} dS = 0 \quad (2.57)$$

Since:

$$dS = 2G\mathbf{n} : d\epsilon - 2Ge_L^t d\lambda \quad (2.58)$$

we get:

$$d\lambda = \frac{2GR_{AM}}{1 + 2Ge_L^t R_{AM}} \mathbf{n} : d\epsilon \quad (2.59)$$

Similarly, starting from:

$$\mathcal{F}_{MA} = \xi_n + \lambda - R_{MA} - S = 0 \quad (2.60)$$

by linearization we get:

$$d\lambda = \frac{2GR_{MA}}{1 + 2Ge_L^t R_{MA}} \mathbf{n} : d\epsilon \quad (2.61)$$

2.8 Numerical Examples

To test the integration algorithm for our model, we run some uniaxial test under displacement control. The material properties are:

$$E = 10 \text{ kPa}, \quad \nu = 0.3 \quad (2.62)$$

while the transformation range are:

$$\sigma_{M_f} = 10, \sigma_{M_s} = 15, \sigma_{A_s} = 20, \sigma_{A_f} = 25 \quad (2.63)$$

with:

$$C_M = 1, C_A = 1, \epsilon_L = 3 \quad (2.64)$$

The test are organized as follow:

- **Test 1:** we run a loading-unloading test with incomplete $A \rightarrow M$ transformation and complete $M \rightarrow A$ transformation (see Figure 2.8.1);
- **Test 2:** we run a loading-unloading test with complete $A \rightarrow M$ transformation and incomplete $M \rightarrow A$ transformation (see Figure 2.8.2);
- **Test 3:** we run a loading-unloading test with incomplete $A \rightarrow M$ transformation and incomplete $M \rightarrow A$ transformation (see Figure 2.8.3);

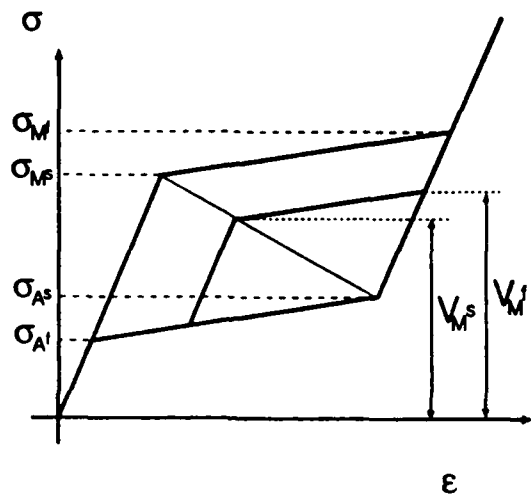


Figure 2.5.1 Pseudo-elastic behavior: modification of the σ -range for the conversion of austenite into martensite.

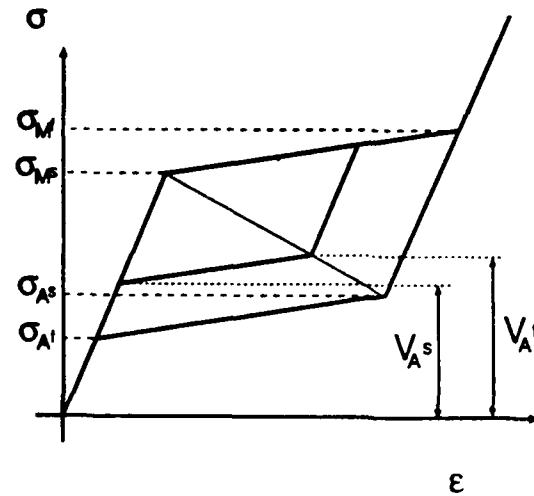


Figure 2.5.2 Pseudo-elastic behavior: modification of the σ -range for the conversion of martensite into austenite.

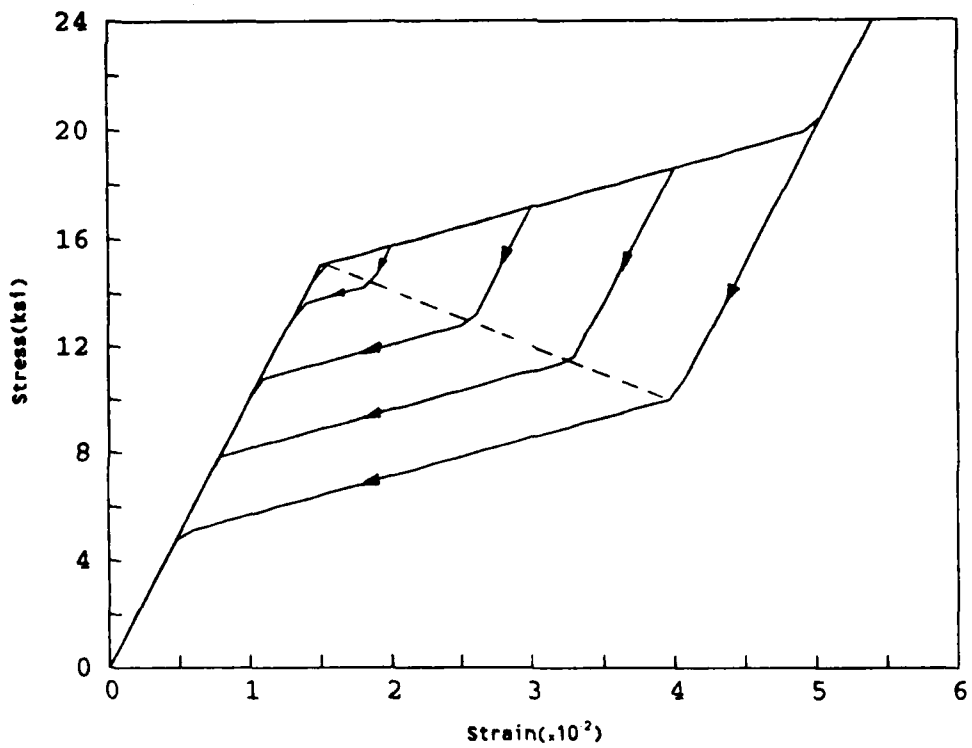


Fig. 2.8.1 Stress Vs strain plot. Complete $M \rightarrow A$ and incomplete $A \rightarrow M$ transformation.

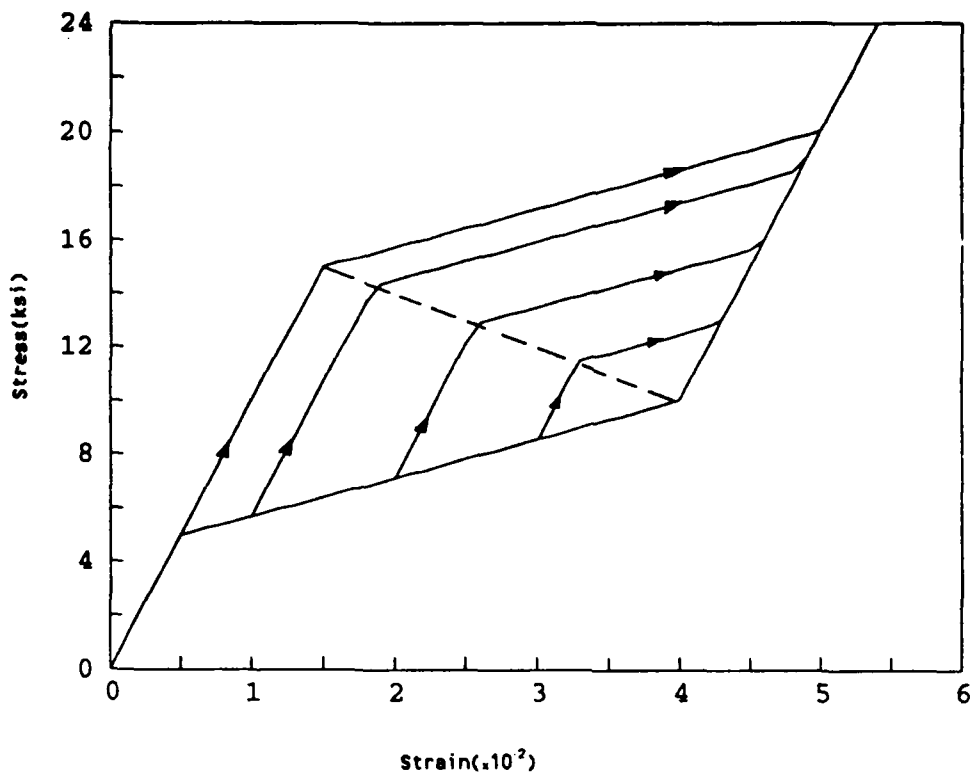


Fig. 2.8.2 Stress Vs strain plot. Incomplete $M \rightarrow A$ and complete $A \rightarrow M$ transformation.

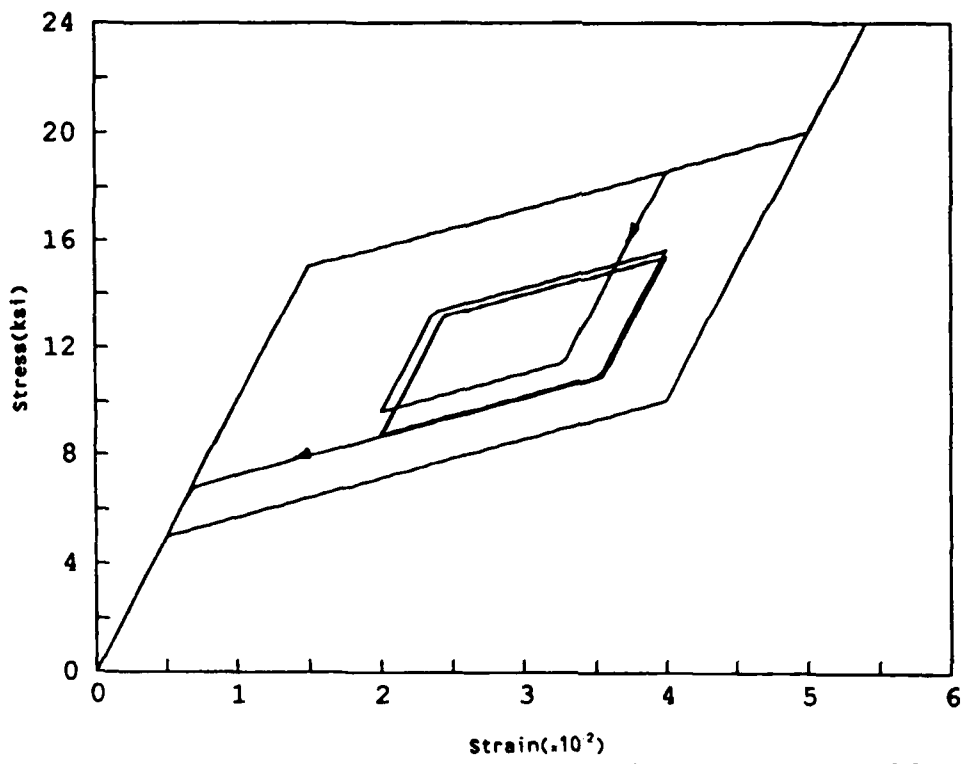


Fig. 2.8.3 Stress Vs strain plot. Incomplete $M \rightarrow A$ and incomplete $A \rightarrow M$ transformations.

CHAPTER 3

FINITE DEFORMATION FORMULATION FOR SHAPE MEMORY ALLOYS

3.1 Introduction

This chapter presents a finite deformation formulation for shape memory alloys. Let

$$\mathbf{F} = \frac{\partial \Phi(\mathbf{X}, t)}{\partial \mathbf{X}} = \frac{\partial \Phi_t}{\partial \mathbf{X}} \quad (3.1)$$

be the deformation gradient, where \mathbf{X} is the reference configuration and Φ_t is the mapping from reference to current configuration, i.e., $\mathbf{x} = \Phi(\mathbf{X}, t) = \Phi_t(\mathbf{X})$. \mathbf{F} is assumed to be sufficiently smooth, orientation preserving, invertible and subject to the constraint

$$J = \det \mathbf{F} > 0 \quad (3.2)$$

to ensure that the material volume element remains positive, and

$$dv = \det \mathbf{F} dV = J dV \quad (3.3)$$

where dV is a volume element in the reference or the material configuration and dv is the corresponding form in the current or the spatial configuration.

In the present formulation a multiplicative decomposition of the deformation gradient into elastic and inelastic parts is assumed

$$\mathbf{F} = \mathbf{F}^e \mathbf{F}^i \quad (3.4)$$

where the superscripts e and i represent elastic and inelastic parts of the deformation gradient, respectively. The inelastic part is associated with phase transformation. See Simo [1988] for details. The inelastic part of the deformation gradient defines an additional configuration $\bar{\mathbf{B}}_t$, or intermediate configuration. The discretized form of (3.4) is

$$\mathbf{F}_{n+1} = \mathbf{F}_{n+1}^e \mathbf{F}_{n+1}^i \quad (3.5)$$

3.2 Phase Transformation Flow Rule

We can derive the flow rule for inelastic or *phase transformation* strain by taking the time derivative of the inelastic deformation gradient.

$$\begin{aligned}
 \dot{\mathbf{F}}^i(\mathbf{X}, t) &= \frac{\partial}{\partial t} \left(\frac{\partial \Phi^i(\mathbf{X}, t)}{\partial \mathbf{X}} \right) \\
 &= \text{GRAD } \mathbf{V}^i(\mathbf{X}, t) \\
 &= \text{grad } \mathbf{v}^i(\mathbf{x}, t) \mathbf{F}^i \\
 &= \frac{d}{dt} \text{grad } \mathbf{u}^i(\mathbf{x}, t) \mathbf{F}^i \\
 &= \dot{\xi} e_L^t \bar{\mathbf{N}}(\bar{\mathbf{S}}) \mathbf{F}^i
 \end{aligned} \tag{3.6}$$

where \mathbf{V}^i is the inelastic material velocity, \mathbf{v}^i and \mathbf{u}^i are the inelastic spatial velocity and displacement fields, respectively. In the above equation $\text{GRAD } \mathbf{V}^i$ is the inelastic material velocity gradient, while $\text{grad } \mathbf{v}^i$ is the inelastic spatial velocity gradient. Furthermore we have used the finite strain counterpart of the small deformation inelastic strain (2.7) to arrive at eq. (3.6). We can write (3.6) as

$$\begin{aligned}
 \dot{\mathbf{F}}^i \mathbf{F}^{i-1} &= \dot{\xi} e_L^t \bar{\mathbf{N}}(\bar{\mathbf{S}}) \\
 \frac{d}{dt} \ln \mathbf{F}^i &= \dot{\xi} e_L^t \bar{\mathbf{N}}(\bar{\mathbf{S}})
 \end{aligned}$$

Integrating both sides from t_n to t_{n+1} we get

$$\begin{aligned}
 \int_{t_n}^{t_{n+1}} d \ln \mathbf{F}^i &= \int_{t_n}^{t_{n+1}} \dot{\xi} e_L^t \bar{\mathbf{N}}(\bar{\mathbf{S}}) dt \\
 \ln \mathbf{F}_{n+1}^i - \ln \mathbf{F}_n^i &= \lambda^* e_L^t \bar{\mathbf{N}}(\bar{\mathbf{S}})
 \end{aligned} \tag{3.7}$$

where we have used eq. (2.33) on the right hand side for λ^* . Equation (3.7) can be written as

$$\begin{aligned}
 \ln \mathbf{F}_{n+1}^i \mathbf{F}_n^{i-1} &= \lambda^* e_L^t \bar{\mathbf{N}}(\bar{\mathbf{S}}) \\
 \mathbf{F}_{n+1}^i \mathbf{F}_n^{i-1} &= \exp(\lambda^* e_L^t \bar{\mathbf{N}}(\bar{\mathbf{S}}))
 \end{aligned}$$

Consequently,

$$\mathbf{F}_{n+1}^i = \exp(\lambda^* e_L^t \bar{\mathbf{N}}(\bar{\mathbf{S}})) \mathbf{F}_n^i \tag{3.8}$$

where λ^* is the increment in the martensite fraction ξ and is obtained through a return mapping algorithm via satisfaction of the corresponding phase transformation criteria, i.e.,

$$\lambda^* = \begin{cases} \lambda^{AM} & \Rightarrow \text{enforcing } \mathcal{F}^{AM}(\xi) = 0 \\ \lambda^{MA} & \Rightarrow \text{enforcing } \mathcal{F}^{MA}(\xi) = 0 \end{cases} \quad (3.9)$$

The manner in which the flow-rule is discretized is an essential part of the method of extension, and consists of taking the inelastic flow direction \bar{N} to be constant throughout the increment and equal to its final value \bar{N}_{n+1} . This reduces the phase transformation flow rule to a system of linear equations for the inelastic deformation gradient \mathbf{F}^i with initial condition \mathbf{F}_n^i , with an exact solution given by the exponential mapping (3.8).

Remark: By expressing the “phase transformation” flow rule and the elastic response on the intermediate configuration, the formulation automatically satisfies material frame indifference. See Cuitino et al. [1992].

3.3 Constitutive Relations

Direct use of deformation gradient \mathbf{F} complicates the development of constitutive equations and it is common to introduce deformation measures which are related completely to either the reference or the current configuration. Accordingly, for the reference configuration the right Cauchy-Green deformation tensor, \mathbf{C} is introduced as

$$\mathbf{C} = \mathbf{F}^T \mathbf{F} = \mathbf{U}^2 \quad (3.10)$$

In the reference configuration, we define the Green strain tensor \mathbf{E} as

$$\mathbf{E} = \frac{1}{2}(\mathbf{C} - \mathbf{1}) \quad (3.11)$$

where $\mathbf{1}$ is the rank two identity tensor with respect to the reference configuration.

We can write the *elastic* right Cauchy-Green transformation tensor in the intermediate configuration as

$$\bar{\mathbf{C}}^e = \mathbf{F}^{i^{-T}} \bar{\mathbf{C}} \mathbf{F}^{i^{-1}} \quad (3.12)$$

where \bar{C} is the full, right Cauchy-Green deformation tensor defined over the intermediate configuration. Accordingly, we define the Green strain tensor on the intermediate configuration

$$\bar{\mathbf{E}} = \frac{1}{2}(\bar{C} - \mathbf{1}) \quad (3.13)$$

Since

$$\frac{1}{2}\log\bar{C} = \frac{1}{2}(\bar{C} - \mathbf{1}) - \frac{1}{2}(\bar{C} - \mathbf{1})(\bar{C} - \mathbf{1}) + \dots \quad (3.14)$$

So we define another strain measure on the intermediate configuration, called the Henky strain

$$\bar{\mathbf{E}}_{(\text{Henky})} = \frac{1}{2}\log\bar{C} \quad (3.15)$$

The second Piola-Kirchhoff stress tensor corresponding to the Henky strain measure defined over the intermediate configuration can be expressed as

$$\hat{\mathbf{S}} = \hat{\mathbf{S}} \left(\frac{1}{2}\log\bar{C} \right) \quad (3.16)$$

Equations (3.5), (3.8) and (3.16) define a system of nonlinear equations which, for given \mathbf{F}_{n+1} can be solved for the updated state variables $\hat{\mathbf{S}}_{n+1}$, $\bar{\mathbf{F}}_{n+1}^i$ and λ . (Note $\lambda \equiv \Delta\xi$). As in the small strain case, it is possible to reduce the system to a single equation for λ , which can be solved by using the return mapping algorithm embedded in the Newton-Raphson iteration scheme.

Remark: The generalized strain measures introduced by Seth (1964a, 1964b) have successfully been applied to the development of material constitutive equations for plasticity, nonlinear viscoelasticity and rubber-like elasticity. In the material description, these strain measures are related to the right Cauchy-Green deformation tensor C through the expression

$$\mathbf{E}^{(m)} = \begin{cases} \frac{1}{m}(C^{m/2} - \mathbf{I}) & m \neq 0 \\ \frac{1}{2}\log C & m = 0 \end{cases} \quad (3.17)$$

where \mathbf{I} is the identity tensor and the exponent m may take on noninteger as well as integer values. For integer values of m these equations reduce to strain measures of Cauchy and Henky. In fact the validity of these equations (3.17) for nonintegral real values of m is assumed if $\frac{1}{m}(\mathbf{C}^{m/2} - \mathbf{I})$ is defined to be coaxial with the right stretch tensor $\mathbf{U} \equiv \mathbf{C}^{1/2}$ and having principal value $\frac{1}{m}(\lambda_\alpha^m - 1)$, ($\alpha = 1, 2, 3$), λ_α being the eigenvalues corresponding to \mathbf{U} . As pointed out by Seth [1964a, 1964b], by introducing a degree of freedom in the exponent m , it is possible to condense the nonlinear effects of deformation into the definition of strain, and thus rely less on representing the nonlinear behaviour in the constitutive equations.

3.4 Radial Return Algorithm

Within the context of radial return algorithm, the right Cauchy-Green deformation tensor for elastic predictor, i.e., the step in which the phase transformation is frozen and a purely elastic deformation is assumed is defined as

$$\bar{\mathbf{C}}_{n+1}^e = \mathbf{F}_{n+1}^{eT} \mathbf{F}_{n+1}^e \quad (3.18)$$

while \mathbf{F}^e is defined in equation (3.4). Using (3.5) and (3.8) with $\lambda = 0$ and substituting in (3.18)

$$\bar{\mathbf{C}}_{n+1}^{e^*} = \mathbf{F}_n^{i^{-T}} \bar{\mathbf{C}}_{n+1} \mathbf{F}_n^{i^{-1}} \quad (3.19)$$

This is the large strain counterpart of the elastic predictor as can be derived from (2.37). We can write the Henky strain (3.15) for the elastic trial state as

$$\mathbf{E}_{(Henky)_{n+1}} = \frac{1}{2} \log \bar{\mathbf{C}}_{n+1}^{e^*} \quad (3.20)$$

The corresponding second Piola-Kirchhoff stress tensor defined on the intermediate configuration is

$$\hat{\mathbf{S}} = \hat{\mathbf{S}} \left(\frac{1}{2} \log \bar{\mathbf{C}}_{n+1}^{e^*} \right) \quad (3.21)$$

We use a J_2 type norm for the elastic trial state defined as

$$S^{\text{tr}} = \|\hat{S}\| = \sqrt{\hat{S}_{n+1} : \hat{S}_{n+1}} \quad (3.22)$$

At this stage it is checked if the state is in the phase transformation range, i.e., if

$$S^{\text{tr}} \notin \{S_{M_s}, S_{M_f}\} \quad \text{for all } \dot{S} > 0 \quad (3.23)$$

and

$$S^{\text{tr}} \notin \{S_{A_s}, S_{A_f}\} \quad \text{for all } \dot{S} < 0 \quad (3.24)$$

then we have the solution at time t_{n+1} and the second part of the algorithm is skipped.

However if

$$S_{M_s} \leq S^{\text{tr}} \leq S_{M_f} \quad \text{for } \dot{S} > 0 \quad (3.25)$$

or

$$S_{A_s} \leq S^{\text{tr}} \leq S_{A_f} \quad \text{for } \dot{S} < 0 \quad (3.26)$$

then phase transformation conditions have to be satisfied to find the solution at time t_{n+1} .

After checking which transformation is possibly active, the parameter λ^* is obtained by enforcing the satisfaction of the corresponding phase transformation model. The elastic right Cauchy-Green deformation tensor can now be written using equation (3.8).

$$\hat{C}_{n+1}^e = \exp(-\lambda^* e_L^t \bar{N}_{n+1}^T) \bar{C}_{n+1}^{e^*} \exp(-\lambda^* e_L^t \bar{N}_{n+1}^T) \quad (3.27)$$

where

$$\bar{N}_{n+1} = \frac{\hat{S}_{n+1}}{\|\hat{S}_{n+1}\|} \quad (3.28)$$

However, if \bar{N}_{n+1} commutes with $\bar{C}_{n+1}^{e^*}$, taking logarithms in (3.27) we get

$$\frac{1}{2} \log \hat{C}_{n+1}^e = \frac{1}{2} \log \bar{C}_{n+1}^{e^*} - \lambda^* \text{sym } \bar{N}_{n+1} \quad (3.29)$$

which is identical to the small-strain kinematic relation that can be derived from (2.39).

It is important to note that the steps proceeding and following the small-strain update are purely kinematic in nature, and hence, material independent. Thus, when it applies,

this procedure provides a material independent prescription for extending small-strain updates into the finite deformation range within the framework of multiplicative plasticity.

The main underlying assumption in arriving at (3.29) is that the phase transformation flow direction \bar{N}_{n+1} commutes with the elastic predictor for large deformation as described in (3.19). Because of the symmetry of $\bar{C}_{n+1}^{\epsilon^*}$, this immediately requires that \bar{N}_{n+1} be likewise symmetric, i.e., that the inelastic spin vanish, and that \bar{N}_{n+1} have the same principal directions as $\bar{C}_{n+1}^{\epsilon^*}$. Correspondingly, n_{n+1} must commute with $\epsilon_{n+1}^{\epsilon^l}$ as can be derived from (2.37), for the small strain formulation. Using (2.32) in (2.39) implies that n_{n+1} commutes with $\epsilon_{n+1}^{\epsilon^l}$ if and only if n_{n+1} commutes with ϵ_{n+1} . By substituting elastic relations $\sigma_{n+1} = \sigma(\epsilon_{n+1}^{\epsilon^l})$ in the phase transformation flow direction $n_{n+1}(\sigma)$, it can be thought of as a function of $n(\epsilon^{\epsilon^l})$ of the elastic strain ϵ^{ϵ^l} . Then the required condition is that the function $n(\epsilon^{\epsilon^l})$ have the same principal directions as ϵ^{ϵ^l} , for all values of its arguments. A general representation of a tensor-valued function satisfying this requirement is

$$n(\epsilon^{\epsilon^l}) = \lambda_1(\epsilon^{\epsilon^l})I + \lambda_2(\epsilon^{\epsilon^l})\epsilon^{\epsilon^l} + \lambda_3(\epsilon^{\epsilon^l})\epsilon^{\epsilon^l} \quad (3.30)$$

where the scalar functions $\{\lambda_1, \lambda_2, \lambda_3\}$, of ϵ^{ϵ^l} need not be isotropic (Cuitino et al. [1992]). Thus the direction of the phase transformation flow n regarded as a function of (ϵ^{ϵ^l}) , while restricted to be of the form (3.30), can still possess some measure of anisotropy (Cuitino et al. [1992]). It bears emphasis that these requirements place no restrictions on the elastic relation $\sigma_{n+1} = \sigma(\epsilon_{n+1}^{\epsilon^l})$, which can be specified arbitrarily. In particular, the elastic response can be anisotropic.

3.5 Boundary Value Problem

In order to formulate a well-defined problem, in addition to the constitutive relations we need to consider the momentum balance equation and suitable boundary and initial conditions.

3.5.1 Strong form of the problem

Let Ω_0 be an open set in \mathcal{R}^3 representing the image of a body B at time t_0 . The study of the motion and deformation of the physical body B then reduces to the study of mappings $\Phi(\mathbf{X}, t) : \Omega_0 \subset \mathcal{R}^3 \rightarrow \mathcal{R}^3$. We assume a constitutive relation on Ω_0 so that the first Piola-Kirchhoff stress tensor \mathbf{P} is a function of $\dot{\mathbf{P}}$ of $\Phi_t(\mathbf{X})$. Let the deformation mapping Φ_t be prescribed on the Dirichlet boundary $\partial_u \Omega_0$ as $\Phi_t|_{\partial_u \Omega_0} = \bar{\Phi}$. The space of configurations is defined as

$$\mathcal{C} = \{\Phi : \Omega_0 \times]0, T[\rightarrow \mathcal{R}^3 \mid \Phi = \Phi_u \text{ on } \partial_u \Omega_0\} \quad (3.31)$$

As usual we require that

$$\partial_u \Omega_0 \cup \partial_\sigma \Omega_0 = \partial \Omega_0 \quad (3.32)$$

$$\partial_u \Omega_0 \cap \partial_\sigma \Omega_0 = \emptyset \quad (3.33)$$

where $\partial_u \Omega_0$ corresponds to the portion of the boundary with prescribed essential boundary conditions, while where $\partial_\sigma \Omega_0$ corresponds to the portion of the boundary with prescribed natural boundary conditions.

The formal statement of the strong form of the problem is: Given a set of boundary conditions, find the motion $\Phi(\mathbf{X}, t) : \Omega_0 \times]0, T[\rightarrow \mathcal{R}^3$, such that

$$\text{DIV}(\mathbf{P}) + \rho \mathbf{f} = \rho \ddot{\mathbf{U}} \quad \text{in } \Omega_0 \times]0, T[\quad (3.34)$$

$$\Phi = \bar{\Phi} \quad \text{on } \partial_u \Omega_0 \times]0, T[\quad (3.35)$$

$$\mathbf{P} \cdot \mathcal{N} = \mathbf{t} \quad \text{on } \partial_\sigma \Omega_0 \times]0, T[\quad (3.36)$$

$$\Phi(\mathbf{X}, 0) = \Phi_0(\mathbf{X}) \quad \text{all } \mathbf{x} \in \Omega_0 \quad (3.37)$$

$$\mathbf{V}(\mathbf{X}, 0) = \mathbf{V}_0(\mathbf{X}) \quad \text{all } \mathbf{x} \in \Omega_0 \quad (3.38)$$

where \mathbf{P} is the first Piola Kirchhoff stress tensor, \mathbf{f} is the body force per unit mass, ρ is the mass density, \mathcal{N} is the unit normal to the boundary, \mathbf{t} is the kirchhoff stress vector,

and $\Phi_0(\mathbf{X})$ and $\mathbf{V}_0(\mathbf{X})$ are the prescribed initial displacement and velocity conditions, respectively.

3.5.2 Weak form of the problem

The space of admissible variations is defined as

$$\mathcal{V} = \{\boldsymbol{\eta} : \Omega_0 \rightarrow \mathbb{R}^3 \mid \boldsymbol{\eta} = \mathbf{0} \text{ on } \partial_u \Omega_0\} \quad (3.39)$$

Let $\mathcal{G}(\Phi, \boldsymbol{\eta}) = \mathcal{C} \times \mathcal{V} \rightarrow \mathbb{R}$ be defined as

$$\mathcal{G}(\Phi, \boldsymbol{\eta}) = \int_{\Omega_0} \rho \mathbf{A} \cdot \boldsymbol{\eta} dV_0 + \int_{\Omega_0} \mathbf{P} : \nabla_0 \boldsymbol{\eta} dV_0 - \int_{\Omega_0} \mathbf{f} \cdot \boldsymbol{\eta} dV_0 - \int_{\partial_e \Omega_0} \mathbf{t} \cdot \boldsymbol{\eta} dS_0 = 0 \quad (3.40)$$

where $\mathbf{A} \doteq \ddot{\mathbf{U}}$. Since the treatment of the transient dynamic problem plays no role in the present discussion, we shall ignore inertia effects and confine our attention to the static case.

Consider a solid initially occupying a reference configuration Ω_0 , and a process of incrementally loading whereby the deformation mapping over Ω_0 changes from Φ_{t_n} , at time t_n , to $\Phi_{t_{n+1}} = \Phi_{t_n} + \mathbf{u}$, at time $t_{n+1} = t_n + \Delta t$. We enforce equilibrium at time t_{n+1} weakly by recourse to the principle of virtual work. The formal statement of the weak form of the boundary value problem is: Find $\Phi \in \mathcal{C}$ such that $\mathcal{G}(\Phi, \boldsymbol{\eta}) = 0$ for all $\boldsymbol{\eta} \in \mathcal{V}$.

$$\int_{\Omega_0} \mathbf{P}_{n+1} : \nabla_0 \boldsymbol{\eta} dV_0 - \int_{\Omega_0} \mathbf{f}_{n+1} \cdot \boldsymbol{\eta} dV_0 - \int_{\partial_e \Omega_0} \mathbf{t}_{n+1} \cdot \boldsymbol{\eta} dS_0 = 0 \quad (3.41)$$

where

\mathbf{P}_{n+1} : denotes the first Piola-Kirchhoff stress field at time t_{n+1} .

\mathbf{f}_{n+1} : is the body force,

\mathbf{t}_{n+1} : are the boundary tractions,

$\boldsymbol{\eta}$: is an admissible virtual displacement field,

∇_0 : denotes the material gradient.

Assuming for now that we have determined a rule to update the stress field of the general form

$$\mathbf{P}_{n+1} = \hat{\mathbf{P}}(\mathbf{F}_{n+1}; \text{state at } t_n, \Delta t) \quad (3.42)$$

where the deformation gradient

$$\mathbf{F}_{n+1} = \nabla_0 \Phi_{n+1} \quad (3.43)$$

is assumed given.

The “consistent tangents” $\hat{\mathbf{K}}_{n+1}$ follow by linearization of the stress updates (3.42) as

$$\hat{\mathbf{K}}_{n+1} = \frac{\partial \hat{\mathbf{P}}}{\partial \mathbf{F}_{n+1}}(\mathbf{F}_{n+1}; \text{state at } t_n, \Delta t) \quad (3.44)$$

The corresponding “spatial consistent tangents” $\hat{\mathbf{k}}_{n+1}$ are obtained by push forward to the current configuration

$$\hat{\mathbf{k}}_{ijkl} = \hat{\mathbf{K}}_{ijkl} F_{kL} F_{jL} F_{lL} \quad (3.45)$$

It is important to note that the use of consistent tangent matrices can be computationally advantageous because of their symmetry, and that they also have superior local approximation properties. For small strains the computation of the consistent tangents reduces to a straightforward exercise for many commonly used models. However in the finite deformation range the calculations are considerably more cumbersome. So in the remaining of this chapter we extend small-strain updates and consistent tangents to the finite deformation range by operating strictly at the level of the kinematics.

3.6 Stress update strategy

Within the context of finite element analysis the solution of problem (3.40) is accomplished by an iterative scheme such as the Newton’s method. Typically one solves a sequence of linearized problems defined as

$$\begin{aligned} \mathbf{D}\mathcal{G}(\Phi_{n+1}^{(i)}, \boldsymbol{\eta}) \cdot \mathbf{u}_{n+1}^{(i)} &\equiv \int_{\Omega_0} \left[\text{tr}(\nabla \boldsymbol{\eta} \tau \nabla \mathbf{u}) + \nabla \boldsymbol{\eta} : (\hat{\mathbf{d}}_{n+1}^{(i)} : \nabla \mathbf{u}_{n+1}^{(i)}) \right] dV_0 \\ &= -\mathcal{G}(\Phi_{n+1}^{(i)}, \boldsymbol{\eta}) \end{aligned} \quad (3.46)$$

until the residual $\mathcal{G}(\Phi_{n+1}^{(i)}, \eta)$ vanishes to within a prescribed tolerance.

The convergence rate of iterative scheme is essentially governed by the choice of tangent moduli $\hat{d}_{n+1}^{(i)}$ which depends in turn on the iteration scheme adopted. In a typical iteration $i + 1$ within a time step $[t_n, t_{n+1}]$, the variables $(\cdot)_{n+1}^{(i+1)}$ may be obtained from either

- the values $(\cdot)_{n+1}^{(i)}$ corresponding to the previous non-converged iteration, or
- the converged values $(\cdot)_n$ from the previous time step.

Both procedures define algorithms which are consistent with the field equations. However, scheme (i) introduces a ‘history dependence’ of the converged values on intermediate non-converged iterates. This may pose difficulties due to the strong path dependence of shape memory models. Spurious unloadings at some Gauss points may also occur as a result of this procedure. By contrast, history dependence on intermediate non-converged values is eliminated with the use of scheme (ii), and fictitious numerical unloading is therefore prevented. For a detailed account of these issues see Simo et al. [1985].

3.7 Derivation of the Consistent Tangent

A lengthy but straightforward calculation of the finite deformation spatial tangents, Cuitino & Ortiz [1992], gives the following expression.

$$\hat{k}_{ijkl} = \hat{d}_{ijkl} - \tau_{nj} A_{inkl} - \tau_{ni} A_{jnkl} + \delta_{ik} \tau_{ij} \quad (3.47)$$

where τ is the Kirchhoff stress tensor. The various terms in (3.47) are defined as below.

$$\hat{d}_{ijkl} = F_{iI}^e F_{jJ}^e \hat{D}_{IJMN} L_{MNKL} (F_{IL}^{e*} F_{kK}^{e*} + F_{kL}^{e*} F_{lK}^{e*}) \quad (3.48)$$

$$\begin{aligned} A_{inkl} &= F_{iI}^e F_{Bn}^{-1} \frac{\partial F_{IB}^i}{\partial F_{KD}} F_{lD} \\ &= F_{iI}^e F_{Bn}^{-1} E_{IBRS} H_{RSMN} L_{MNKL} (F_{IL}^{e*} F_{kK}^{e*} + F_{kL}^{e*} F_{lK}^{e*}) \end{aligned} \quad (3.49)$$

where \hat{D} represents the small-strain tangent defined as

$$\hat{D} = \frac{\partial \sigma}{\partial \epsilon} \quad (3.50)$$

which is the only material dependent quantity in eq (3.47). \mathbf{F}^{ϵ^*} may be thought of as an elastic predictor for \mathbf{F}^ϵ , and

$$\mathbf{C}^\epsilon = \frac{\partial \mathbf{e}^\epsilon}{\partial \sigma} \quad (3.51)$$

are the tangent elastic compliances.

In component form

$$\mathbf{F}_{iJ}^{\epsilon^*} = \mathbf{F}_{iA}(\mathbf{F}_n^{i-1})_{AJ} \quad (3.52)$$

$$L_{MNKL} = \frac{\partial (\log \sqrt{\bar{C}^\epsilon})_{MN}}{\partial \bar{C}^\epsilon} \quad (3.53)$$

$$\begin{aligned} E_{IBRS} &= \frac{\partial F_{IB}^i}{\partial (\lambda^* e_L^t \bar{N})_{RS}} \\ &= \frac{\partial [\exp(\lambda^* e_L^t \bar{N})]_{IJ}}{\partial (\lambda^* e_L^t \bar{N})_{RS}} (F_n^i)_{JB} \end{aligned} \quad (3.54)$$

$$\begin{aligned} H_{RSMN} &= \frac{\partial (\lambda^* e_L^t \bar{N})_{RS}}{\partial \epsilon_{MN}^{\epsilon^*}} \\ &= (\delta_{RM} \delta_{SN} + \delta_{RN} \delta_{SM}) - C_{RSAB}^{\epsilon} \hat{D}_{ABMN} \end{aligned} \quad (3.55)$$

$$C_{RSAB}^{\epsilon} = \frac{1}{2\mu} (\delta_{RA} \delta_{SB}) - \frac{\lambda}{3\lambda + 2\mu} (\delta_{BA} \delta_{RS}) \quad (3.56)$$

where λ and μ in the last equation are the Lame's constants.

3.7.1 Derivation of L_{MNKL}

$$\mathbf{L} = \frac{\partial (\log \sqrt{\bar{C}^\epsilon})}{\partial \bar{C}^\epsilon} \quad (3.57)$$

By the spectral theorem for symmetric positive definite tensors we have

$$\bar{C}^\epsilon = \sum_{a=1}^3 \lambda_a^2 \mathbf{N}^{(a)} \otimes \mathbf{N}^{(a)} \quad (a = 1, 2, 3) \quad (3.58)$$

The invariants of \bar{C}^ϵ are related to the coefficients in the characteristic polynomial $p(\lambda^2)$ of \bar{C}^ϵ as follows,

$$p(\lambda_a^2) := -\lambda_a^6 + I_1 \lambda_a^4 - I_2 \lambda_a^2 + I_3 = 0 \quad (a = 1, 2, 3) \quad (3.59)$$

where $\lambda_a^2 > 0$ are the roots of the characteristic polynomial. Therefore

$$\begin{aligned}\sqrt{\bar{C}^\epsilon} &= \sum_{a=1}^3 \lambda_a \mathbf{N}^{(a)} \otimes \mathbf{N}^{(a)} \\ \Rightarrow \log \sqrt{\bar{C}^\epsilon} &= \sum_{a=1}^3 \log \lambda_a \mathbf{N}^{(a)} \otimes \mathbf{N}^{(a)}\end{aligned}\quad (3.60)$$

Note: If $\mathbf{N}^{(A)}$ is a proper vector of \bar{C}^ϵ , it is also a proper vector of $\log \sqrt{\bar{C}^\epsilon}$. The principal invariants of $\bar{C}^\epsilon \in \mathcal{S}_+^3$ are denoted by

$$I_1 := \text{tr}[\bar{C}^\epsilon]; \quad I_2 := \frac{1}{2} [I_1^2 - \text{tr}(\bar{C}^{\epsilon^2})]; \quad I_3 := \det[\bar{C}^\epsilon] = J^2 \quad (3.61)$$

where

$$\mathcal{S}_+^3 = \left\{ \bar{C}^\epsilon \in \mathcal{M}_+^3 \mid \bar{C}^\epsilon = \bar{C}^{\epsilon^T} \right\} \quad (3.62)$$

Following standard usage, we denote by $\mathcal{L}(\mathcal{R}^3, \mathcal{R}^3)$ the vector space of linear transformation in $\mathcal{R}^3, \mathcal{M}^3$ is defined as

$$\mathcal{M}_+^3 = \left\{ \mathbf{F} \in \mathcal{L}(\mathcal{R}^3, \mathcal{R}^3) \mid \det[\mathbf{F}] > 0 \right\} \quad (3.63)$$

By the chain rule

$$\frac{\partial \log \sqrt{\bar{C}^\epsilon}}{\partial C} = \frac{\partial \log \sqrt{\bar{C}^\epsilon}}{\partial I_1} \frac{\partial I_1}{\partial C} + \frac{\partial \log \sqrt{\bar{C}^\epsilon}}{\partial I_2} \frac{\partial I_2}{\partial C} + \frac{\partial \log \sqrt{\bar{C}^\epsilon}}{\partial I_3} \frac{\partial I_3}{\partial C} \quad (3.64)$$

In order to evaluate the above expression we need the following results.

$$\frac{\partial \log \sqrt{\bar{C}^\epsilon}}{\partial I_a} = \frac{\partial \log \sqrt{\bar{C}^\epsilon}}{\partial \lambda_1} \frac{\partial \lambda_1}{\partial I_a} + \frac{\partial \log \sqrt{\bar{C}^\epsilon}}{\partial \lambda_2} \frac{\partial \lambda_2}{\partial I_a} + \frac{\partial \log \sqrt{\bar{C}^\epsilon}}{\partial \lambda_3} \frac{\partial \lambda_3}{\partial I_a} \quad (3.65)$$

3.7.1.1 Proposition: Assume that $\lambda_1 \neq \lambda_2 \neq \lambda_3$. By (3.59) λ_a is a function of the invariants of \bar{C}^ϵ , denoted by

$$\lambda_a = \lambda_a(I_1, I_2, I_3) \quad (a = 1, 2, 3) \quad (3.66)$$

Then the following relations hold:

$$\frac{\partial \lambda_a}{\partial I_1} = \frac{\lambda_a^3}{2D_a}; \quad \frac{\partial \lambda_a}{\partial I_2} = \frac{-\lambda_a}{2D_a}; \quad \frac{\partial \lambda_a}{\partial I_3} = \frac{\lambda_a^{-2}}{D_a} \quad (3.67)$$

where $D_a = (\lambda_a^2 - \lambda_b^2)(\lambda_a^2 - \lambda_c^2)$. See proof in Simo et al. [1991], p. 227.

Consequently, we can derive the following relations as follows

$$\begin{aligned}\frac{\partial}{\partial I_1} \log \sqrt{\bar{C}^\epsilon} &= \frac{\partial}{\partial I_1} \sum_{a=1}^3 \log \lambda_a \mathbf{N}^{(a)} \otimes \mathbf{N}^{(a)} \\ &= \sum_{a=1}^3 \frac{1}{\lambda_a} \left(\frac{\lambda_a^3}{2D_a} \right) \mathbf{N}^{(a)} \otimes \mathbf{N}^{(a)} \\ &= \frac{1}{2} \sum_{a=1}^3 \left(\frac{\lambda_a^2}{D_a} \right) \mathbf{N}^{(a)} \otimes \mathbf{N}^{(a)}\end{aligned}\quad (3.68)$$

Similarly, for the second term we get

$$\begin{aligned}\frac{\partial}{\partial I_2} \log \sqrt{\bar{C}^\epsilon} &= \sum_{a=1}^3 \frac{1}{\lambda_a} \left(\frac{-\lambda_a}{2D_a} \right) \mathbf{N}^{(a)} \otimes \mathbf{N}^{(a)} \\ &= \frac{-1}{2} \sum_{a=1}^3 \left(\frac{1}{D_a} \right) \mathbf{N}^{(a)} \otimes \mathbf{N}^{(a)}\end{aligned}\quad (3.69)$$

and

$$\frac{\partial}{\partial I_3} \log \sqrt{\bar{C}^\epsilon} = \frac{1}{2} \sum_{a=1}^3 \left(\frac{\lambda_a^{-2}}{D_a} \right) \mathbf{N}^{(a)} \otimes \mathbf{N}^{(a)} \quad (3.70)$$

Using the chain rule for the second term in equ (3.64)

$$\frac{\partial I_\alpha}{\partial \bar{C}^\epsilon} = \frac{\partial I_\alpha}{\partial \lambda_1} \frac{\partial \lambda_1}{\partial \bar{C}^\epsilon} + \frac{\partial I_\alpha}{\partial \lambda_2} \frac{\partial \lambda_2}{\partial \bar{C}^\epsilon} + \frac{\partial I_\alpha}{\partial \lambda_3} \frac{\partial \lambda_3}{\partial \bar{C}^\epsilon} \quad (3.71)$$

where

$$\frac{\partial I_\alpha}{\partial \lambda_\beta} = 2\lambda_\beta \frac{\partial I_\alpha}{\partial \lambda_\beta^2} \quad (\beta = 1, 2, 3) \quad (3.72)$$

3.7.1.2 Proposition: Let the spectral decomposition of \bar{C}^ϵ be defined by eq. (3.58) So λ_a is a function of \bar{C}^ϵ and we write $\lambda_a = \lambda_a(\bar{C}^\epsilon)$. Upon defining

$$\begin{aligned}\mathbf{M}^{(a)} &:= \lambda_a^{-2} \mathbf{N}^{(a)} \otimes \mathbf{N}^{(a)} \\ &= \mathbf{F}^{-1} [\mathbf{N}^{(a)} \otimes \mathbf{N}^{(a)}] \mathbf{F}^{-T}\end{aligned}\quad (3.73)$$

we have the basic relations

$$(1) \quad \frac{\partial \lambda_a}{\partial \bar{C}^e} = \frac{1}{2} \lambda_a M^{(a)} \quad (a = 1, 2, 3) \quad \text{iff } \lambda_1 \neq \lambda_2 \neq \lambda_3 \quad (3.74)$$

$$(2) \quad \frac{\partial \lambda_1}{\partial \bar{C}^e} = \frac{1}{2} \lambda_1 [\bar{C}^{e^{-1}} - M^{(3)}] \quad \text{iff } \lambda_1 = \lambda_2 \neq \lambda_3 \quad (3.75)$$

$$\frac{\partial \lambda_3}{\partial \bar{C}^e} = \frac{1}{2} \lambda_3 M^{(3)} \quad (3.76)$$

$$(3) \quad \frac{\partial \lambda_1}{\partial \bar{C}^e} = \frac{1}{2} \lambda_1 \bar{C}^{e^{-1}} \quad \text{iff } \lambda_1 = \lambda_2 = \lambda_3 \quad (3.77)$$

Consequently, using these relations in (3.71), we get

$$\begin{aligned} \frac{\partial I_1}{\partial \bar{C}^e} &= \sum_{b=1}^3 2\lambda_b \left(\frac{1}{2} \lambda_b M^{(b)} \right) \\ &= \sum_{b=1}^3 \lambda_b^2 \left(\lambda_b^{-2} N^{(b)} \otimes N^{(b)} \right) \\ &= \sum_{b=1}^3 N^{(b)} \otimes N^{(b)} \end{aligned} \quad (3.78)$$

Similarly, for the second term we get

$$\begin{aligned} \frac{\partial I_2}{\partial \bar{C}^e} &= \sum_{b=1}^3 \frac{\partial I_2}{\partial \lambda_b} \cdot \frac{\partial \lambda_b}{\partial \bar{C}^e} \\ &= \sum_{b=1}^3 2\lambda_b (I_1 - \lambda_b^2) \cdot \left(\frac{1}{2} \lambda_b M^{(b)} \right) \\ &= \sum_{b=1}^3 (I_1 - \lambda_b^2) N^{(b)} \otimes N^{(b)} \end{aligned} \quad (3.79)$$

and

$$\begin{aligned} \frac{\partial I_3}{\partial \bar{C}^e} &= \sum_{b=1}^3 \frac{\partial I_3}{\partial \lambda_b} \cdot \frac{\partial \lambda_b}{\partial \bar{C}^e} \\ &= \sum_{b=1}^3 \frac{2I_3}{\lambda_b} \left(\frac{1}{2} \lambda_b M^{(b)} \right) \\ &= \sum_{B=1}^3 I_3 \lambda_B^{-2} N^{(B)} \otimes N^{(B)} \end{aligned} \quad (3.80)$$

Remark: For a general framework see Marsden & Hughes [1983], pp. 220–222.

Substituting the corresponding expressions in (3.64)

$$\begin{aligned}\frac{\partial(\log\sqrt{\bar{C}^\epsilon})}{\partial\bar{C}^\epsilon} &= \left(\frac{1}{2}\sum_{a=1}^3\left(\frac{\lambda_a^2}{D_a}\right)\mathbf{N}^{(a)}\otimes\mathbf{N}^{(a)}\right)\cdot\left(\sum_{b=1}^3\mathbf{N}^{(b)}\otimes\mathbf{N}^{(b)}\right) \\ &+ \left(\frac{-1}{2}\sum_{a=1}^3\left(\frac{1}{D_a}\right)\mathbf{N}^{(a)}\otimes\mathbf{N}^{(a)}\right)\cdot\left(\sum_{b=1}^3(I_1 - \lambda_b^2)\mathbf{N}^{(b)}\otimes\mathbf{N}^{(b)}\right) \\ &+ \left(\frac{1}{2}\sum_{a=1}^3\left(\frac{\lambda_a^{-2}}{D_a}\right)\mathbf{N}^{(a)}\otimes\mathbf{N}^{(a)}\right)\cdot\left(\sum_{b=1}^3I_3\lambda_b^{-2}\mathbf{N}^{(b)}\otimes\mathbf{N}^{(b)}\right)\end{aligned}\quad (3.81)$$

where $D_a = (\lambda_a^2 - \lambda_b^2)(\lambda_a^2 - \lambda_c^2)$

The closed form expression for $\mathbf{N}^{(a)}\otimes\mathbf{N}^{(a)}$ is

$$\mathbf{N}^{(a)}\otimes\mathbf{N}^{(a)} = \lambda_a^2 \left\{ \frac{\bar{C}^\epsilon - (I_1 - \lambda_a^2)\mathbf{I} + I_3\lambda_a^{-2}\bar{C}^{\epsilon^{-1}}}{D_a} \right\} \quad (3.82)$$

3.7.1.3 First Order Approximation

A first order approximation for $\sqrt{\bar{C}^\epsilon}$ can be expressed as

$$\sqrt{\bar{C}^\epsilon} \cong \frac{1}{2}(\mathbf{I} + \bar{C}^\epsilon) \quad (3.83)$$

Consequently, a first order approximation for $\log\sqrt{\bar{C}^\epsilon}$ can be written as

$$\log\sqrt{\bar{C}^\epsilon} \cong \log\left(\frac{1}{2}(\mathbf{I} + \bar{C}^\epsilon)\right) = \frac{1}{2}(\bar{C}^\epsilon - \mathbf{I}) - \frac{1}{8}(\bar{C}^\epsilon - \mathbf{I})^2 + \dots \quad (3.84)$$

Therefore

$$\begin{aligned}\frac{\partial(\log\sqrt{\bar{C}^\epsilon})_{MN}}{\partial\bar{C}_{KL}^\epsilon} &= \frac{\partial}{\partial C_{KL}} \left\{ \frac{1}{2}(\bar{C}^\epsilon - \mathbf{I})_{MN} - \frac{1}{8}(\bar{C}^\epsilon - \mathbf{I})_{MN}^2 \right\} \\ &= \frac{3}{4}\delta_{MK}\delta_{NL} - \frac{1}{8}(\delta_{MK}\bar{C}_{LN}^\epsilon + \delta_{NL}\bar{C}_{MK}^\epsilon)\end{aligned}\quad (3.85)$$

3.7.2 Derivation of H_{RSMN}

$$\mathbf{H} = \frac{\partial(\exp(\lambda^* e_L^t \bar{\mathbf{N}}(\bar{\mathbf{S}})))}{(\lambda^* e_L^t \bar{\mathbf{N}}(\bar{\mathbf{S}}))} \mathbf{F}_n^i \quad (3.86)$$

Let $(\lambda^* e_L^t \bar{\mathbf{N}}(\bar{\mathbf{S}})) = \mathbf{K}$. Employing the spectral theorem for symmetric positive definite tensors, (3.58), we can write

$$\exp(\mathbf{K}) = \sum_{a=1}^3 \exp(\lambda_a^2) \mathbf{N}^{(a)} \otimes \mathbf{N}^{(a)} \quad (3.87)$$

λ_a 's in (3.88) should not be confused with previously defined λ_a 's. The principal invariants of $\mathbf{K} \in \mathcal{S}_+^3$ are denoted by

$$I_1 := \text{tr}[\mathbf{K}]; \quad I_2 := \frac{1}{2} [I_1^2 - \text{tr}(\mathbf{K}^2)]; \quad I_3 := \det[\mathbf{K}] = J^2 \quad (3.88)$$

where $\mathcal{S}_+^3 = \{\mathbf{K} \in \mathcal{M}_+^3 | \mathbf{K} = \mathbf{K}^T\}$. We denote by $\mathcal{L}(\mathcal{R}^3, \mathcal{R}^3)$ the vector space of linear transformation in \mathcal{R}^3 , \mathcal{M}^3 is defined in eq. (3.63). Therefore

$$\frac{\partial \exp(\mathbf{K})}{\partial \mathbf{K}} = \frac{\partial \exp(\mathbf{K})}{\partial I_1} \frac{\partial I_1}{\partial \mathbf{K}} + \frac{\partial \exp(\mathbf{K})}{\partial I_2} \frac{\partial I_2}{\partial \mathbf{K}} + \frac{\partial \exp(\mathbf{K})}{\partial I_3} \frac{\partial I_3}{\partial \mathbf{K}} \quad (3.89)$$

Once again, in order to evaluate the above expression we need the following results.

$$\frac{\partial \exp(\mathbf{K})}{\partial I_a} = \frac{\partial \exp(\mathbf{K})}{\partial \lambda_1} \frac{\partial \lambda_1}{\partial I_a} + \frac{\partial \exp(\mathbf{K})}{\partial \lambda_2} \frac{\partial \lambda_2}{\partial I_a} + \frac{\partial \exp(\mathbf{K})}{\partial \lambda_3} \frac{\partial \lambda_3}{\partial I_a} \quad (3.90)$$

Assuming that $\lambda_1 \neq \lambda_2 \neq \lambda_3$. By (3.59) λ_a is a function of the invariants of \mathbf{K} , denoted by

$$\lambda_a = \lambda_a(I_1, I_2, I_3) \quad (a = 1, 2, 3) \quad (3.91)$$

Then the following relations hold:

$$\frac{\partial \lambda_a^2}{\partial I_1} = \frac{\lambda_a^2}{D_a}; \quad \frac{\partial \lambda_a^2}{\partial I_2} = \frac{-\lambda_a^2}{D_a}; \quad \frac{\partial \lambda_a^2}{\partial I_3} = \frac{1}{D_a}$$

where D_a is defined earlier. For proof see Simo et al. [1991], p. 227.

Consequently,

$$\begin{aligned}\frac{\partial}{\partial I_1} \exp(\mathbf{K}) &= \frac{\partial}{\partial I_1} \sum_{a=1}^3 \exp(\lambda_a^2) \mathbf{N}^{(a)} \otimes \mathbf{N}^{(a)} \\ &= \sum_{a=1}^3 \exp(\lambda_a^2) \left(\frac{\lambda_a^4}{D_a} \right) \mathbf{N}^{(a)} \otimes \mathbf{N}^{(a)}\end{aligned}\quad (3.92)$$

Similarly,

$$\frac{\partial}{\partial I_2} \exp(\mathbf{K}) = \sum_{a=1}^3 \exp(\lambda_a^2) \left(\frac{-(\lambda_a^2)}{D_a} \right) \mathbf{N}^{(a)} \otimes \mathbf{N}^{(a)} \quad (3.93)$$

and

$$\frac{\partial}{\partial I_3} \exp(\mathbf{K}) = \sum_{a=1}^3 \exp(\lambda_a^2) \left(\frac{1}{D_a} \right) \mathbf{N}^{(a)} \otimes \mathbf{N}^{(a)} \quad (3.94)$$

Employing the chain rule for the second term in (3.90),

$$\frac{\partial I_\alpha}{\partial \mathbf{K}} = \frac{\partial I_\alpha}{\partial \lambda_1^2} \frac{\partial \lambda_1^2}{\partial \mathbf{K}} + \frac{\partial I_\alpha}{\partial \lambda_2^2} \frac{\partial \lambda_2^2}{\partial \mathbf{K}} + \frac{\partial I_\alpha}{\partial \lambda_3^2} \frac{\partial \lambda_3^2}{\partial \mathbf{K}} \quad (3.95)$$

where

$$\begin{aligned}\frac{\partial \lambda_\beta^2}{\partial \mathbf{K}} &= \frac{\partial \lambda_\beta^2}{\partial \lambda_\beta} \cdot \frac{\partial \lambda_\beta}{\partial \mathbf{K}} \\ &= 2\lambda_\beta \cdot \frac{\partial \lambda_\beta}{\partial \mathbf{K}}\end{aligned}\quad (3.96)$$

Substituting in (3.90), we get

$$\begin{aligned}\frac{\partial(\exp \mathbf{K})}{\partial \mathbf{K}} &= \left(\sum_{a=1}^3 \exp(\lambda_a^2) \left(\frac{(\lambda_a^2)}{D_a} \right) \mathbf{N}^{(a)} \otimes \mathbf{N}^{(a)} \right) \cdot \left(\sum_{b=1}^3 \mathbf{N}^{(b)} \otimes \mathbf{N}^{(b)} \right) \\ &+ \left(\sum_{a=1}^3 \exp(\lambda_a^2) \left(\frac{-(\lambda_a^2)}{D_a} \right) \mathbf{N}^{(a)} \otimes \mathbf{N}^{(a)} \right) \cdot \left(\sum_{b=1}^3 (I_1 - \lambda_b^2) \mathbf{N}^{(b)} \otimes \mathbf{N}^{(b)} \right) \\ &+ \left(\sum_{a=1}^3 \exp(\lambda^2) \left(\frac{1}{D_a} \right) \mathbf{N}^{(a)} \otimes \mathbf{N}^{(a)} \right) \cdot \left(\sum_{b=1}^3 (I_3 \lambda_b^{-2}) \mathbf{N}^{(b)} \otimes \mathbf{N}^{(b)} \right)\end{aligned}\quad (3.97)$$

where $D_a = (\lambda_a^2 - \lambda_b^2)(\lambda_a^2 - \lambda_c^2)$ Using (97) in (86) we get the desired result.

3.7.2.1 First Order Approximation

In component form, we can write $\exp(K_{ij})$ as follows

$$\exp(K_{ij}) \cong \delta_{ij} + K_{ij} + \frac{1}{2!} K_{ik} K_{kj} + \frac{1}{3!} K_{ik} K_{kl} K_{lj} + \dots \quad (3.98)$$

Retaining up to quadratic terms in (3.99) we get

$$\frac{\partial(\exp K)_{ij}}{\partial K_{kl}} = \delta_{ik} \delta_{jl} + \frac{1}{2} (\delta_{ik} K_{lj} + K_{ik} \delta_{jl}) \quad (3.99)$$

3.7.3 Finite Deformation Update

Once all terms in eq. (3.48) and (3.49) are calculated, the full finite deformation update comprises three steps:

1. *Preprocessor step.* Compute the predictor logarithmic elastic strains $\frac{1}{2}\log\bar{C}_{n+1}^e$ from the given updated deformation gradients F_{n+1} as in (3.19). Set ϵ_{n+1}^e equal to $\frac{1}{2}\log\bar{C}_{n+1}^e$. Identify σ_n with \bar{S}_n .
2. *Small strain update.* Effect a small-strain update driven by ϵ_{n+1}^e with initial conditions σ_n , to compute σ_{n+1} and λ^* .
3. *Postprocessor step.* Identify \bar{S}_{n+1} with σ_{n+1} and compute F_{n+1}^i by the exponential mapping (3.8).

It is important to note that the steps preceding and following the small-strain update are purely kinematic in nature, and hence, material independent.

3.8 Numerical Results

In order to test the integration algorithm in the finite deformation range, we performed a series of uniaxial simulations under displacement control. The material properties are

$$E = 7500 \text{ kPa}, \quad \nu = 0.3 \quad (3.100)$$

while the transformation ranges are:

$$\sigma_{M_s} = 50, \quad \sigma_{M_u} = 70, \quad \sigma_{A_s} = 75, \quad \sigma_{A_u} = 90 \quad (3.101)$$

with

$$C_M = 1, C_A = 1, \quad \epsilon_L = 0.6 \quad (3.102)$$

The tests are organized as follows:

- **Test 1:** we run a loading-unloading test with complete $A \rightarrow M$ transformation and complete $M \rightarrow A$ transformation (see Figures 3.8.1 – 3.8.5).
- **Test 2:** we run a loading-unloading test with incomplete $A \rightarrow M$ transformation and complete $M \rightarrow A$ transformation (see Figures 3.8.6 – 3.8.10).
- **Test 3:** we run a loading-unloading test with complete $A \rightarrow M$ transformation and incomplete $M \rightarrow A$ transformation (see Figures 3.8.11 – 3.8.15).
- **Test 4:** we run a loading-unloading test with incomplete $A \rightarrow M$ transformation and incomplete $M \rightarrow A$ transformation (see Figures 3.8.16 – 3.8.20).

3.8.1 Test 1: Complete $A \rightarrow M$ and $M \rightarrow A$ transformations

Figure 3.8.1 presents the stress-strain plot for complete phase transformations in either case. The applied strain as a function of the time parameter is presented next. Variable loading increments can be applied under the present technique. The specimen is loaded to a certain strain and unloaded to zero stress condition in each loading cycle. Figure 3.8.3 presents the stress variation at a Gauss point as a function of t . Figures 3.8.4–5 show the variation in the internal *phase transformation* parameter ξ as a function of strain ϵ at the Gauss point and of time (t), respectively.

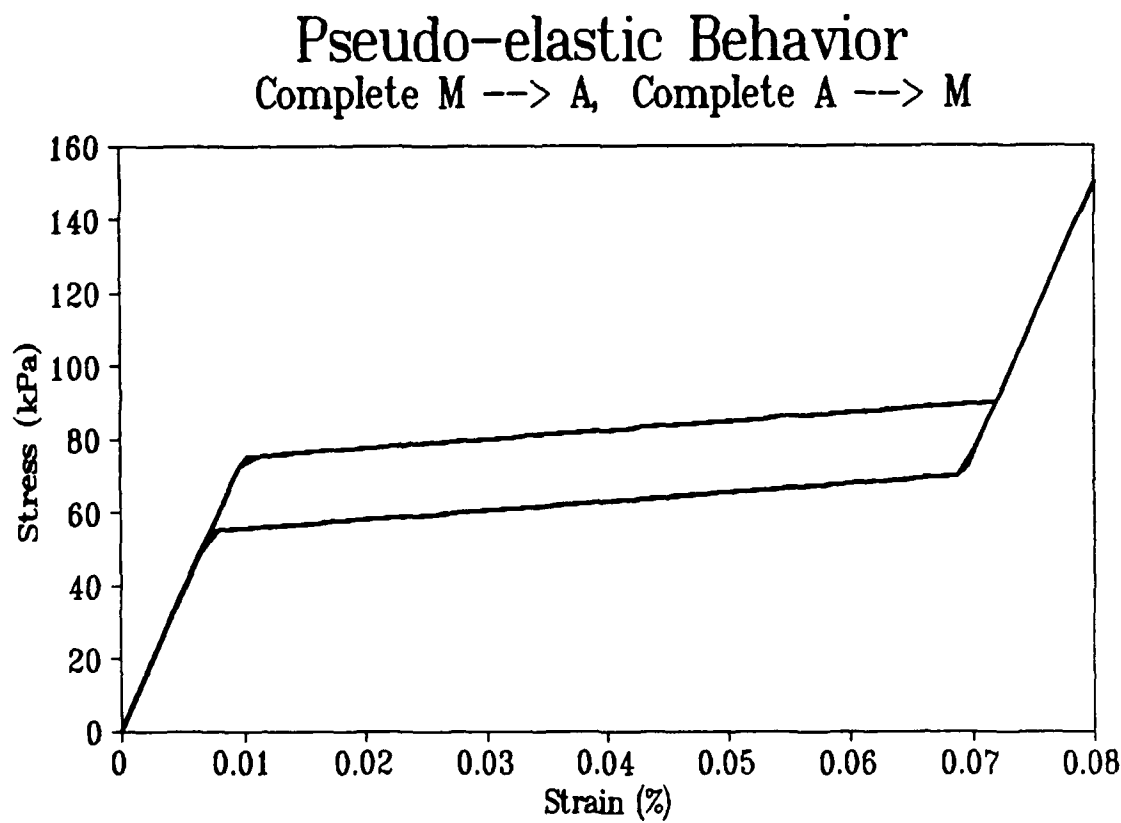


Fig. 3.8.1 Stress Vs strain plot. Complete $M \rightarrow A$ and complete $A \rightarrow M$ transformations.

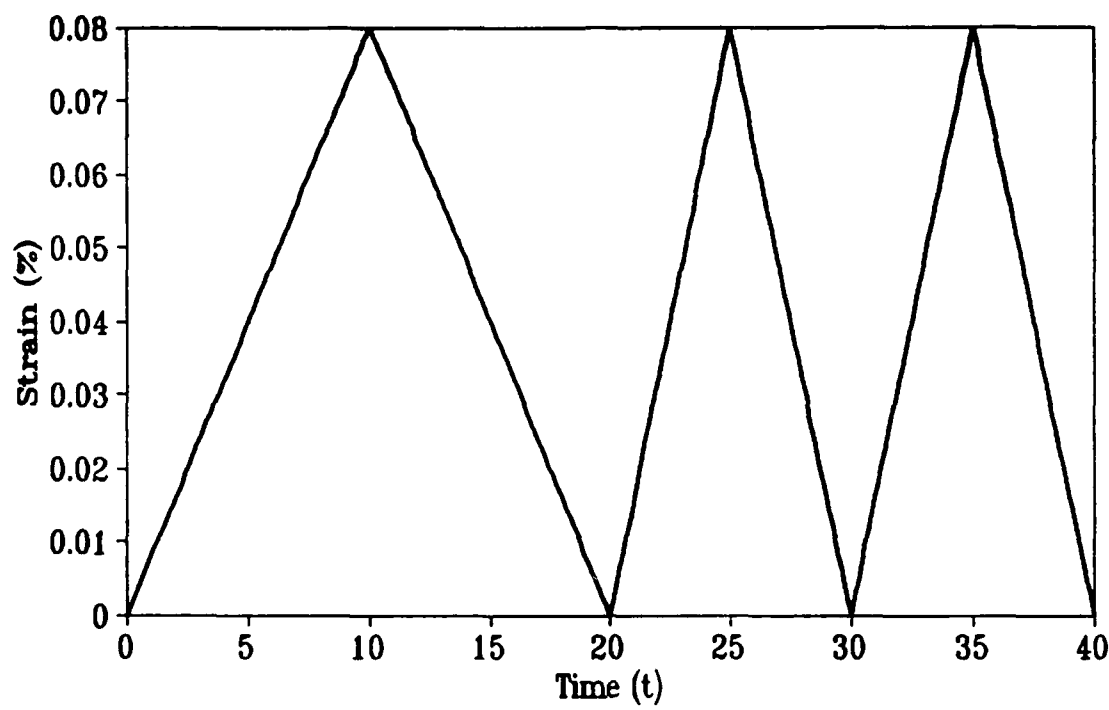


Fig. 3.8.2 Strain Vs time plot. Complete $M \rightarrow A$ and complete $A \rightarrow M$ transformations.

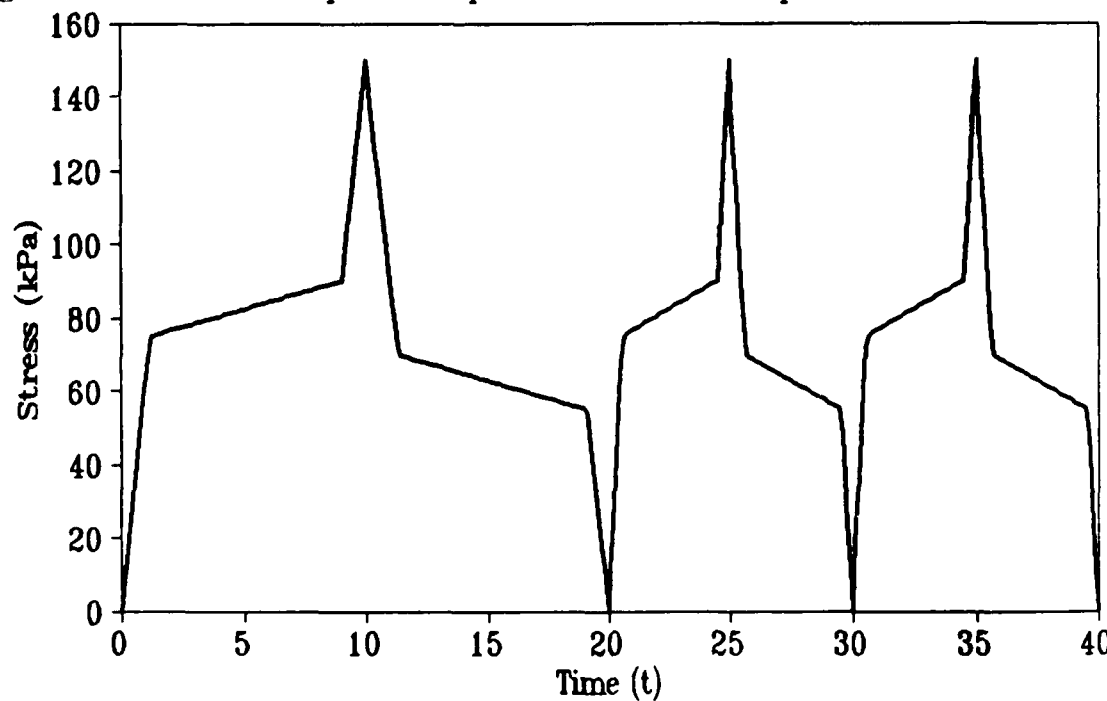


Fig. 3.8.3 Stress Vs time plot. Complete $M \rightarrow A$ and complete $A \rightarrow M$ transformations.

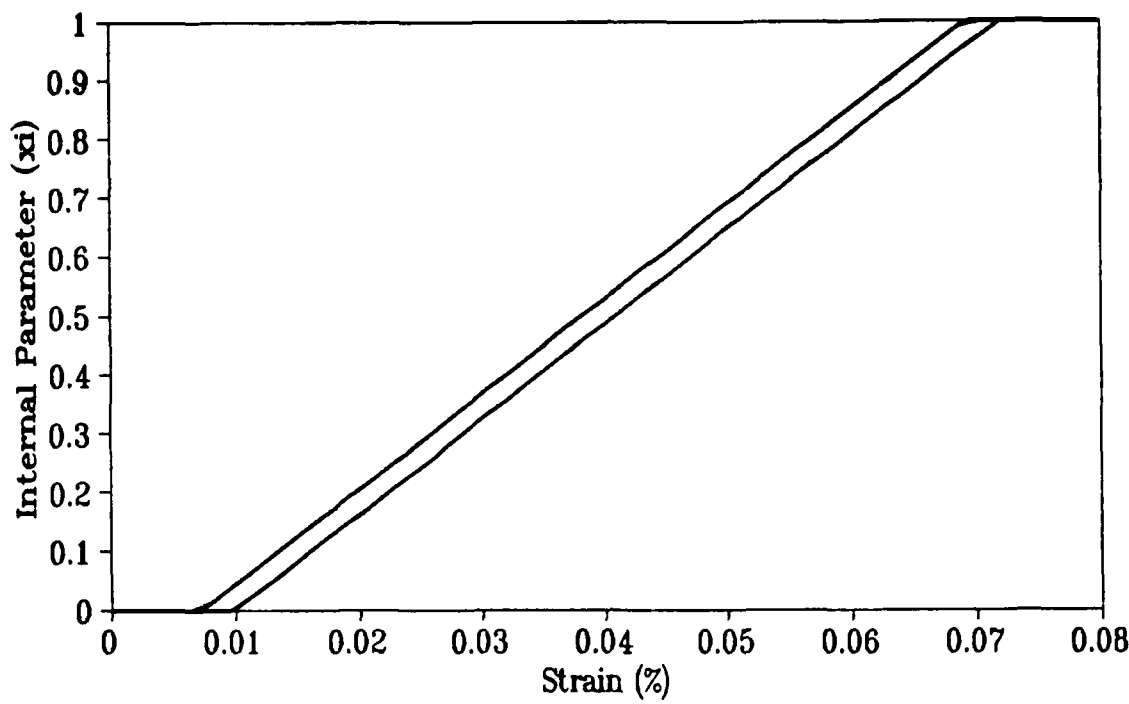


Fig. 3.8.4 Internal parameter Vs strain. Complete $M \rightarrow A$ and complete $A \rightarrow M$ transformations.

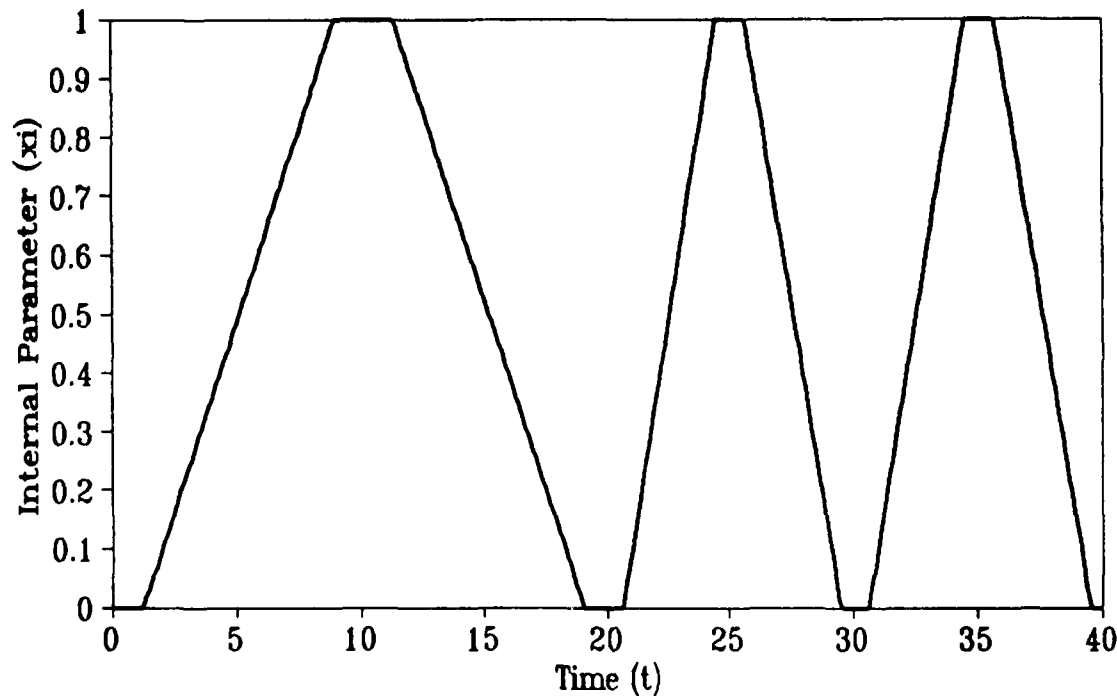


Fig. 3.8.5 Internal parameter Vs time. Complete $M \rightarrow A$ and complete $A \rightarrow M$ transformations.

3.8.2 Test 2: Incomplete $A \rightarrow M$ and complete $M \rightarrow A$ transformations

Figure 3.8.6 presents the stress-strain plot for incomplete $A \rightarrow M$ and complete $M \rightarrow A$ transformation. The applied strain as a function of the time parameter is presented next. The strain is increased gradually and the specimen is unloaded to zero stress condition in each cycle. Figure 3.8.8 presents the stress variation at a Gauss point as a function of t . Figures 3.8.9–10 show the variation in the internal *phase transformation* parameter ξ as a function of strain ϵ at the Gauss point and of time (t), respectively.

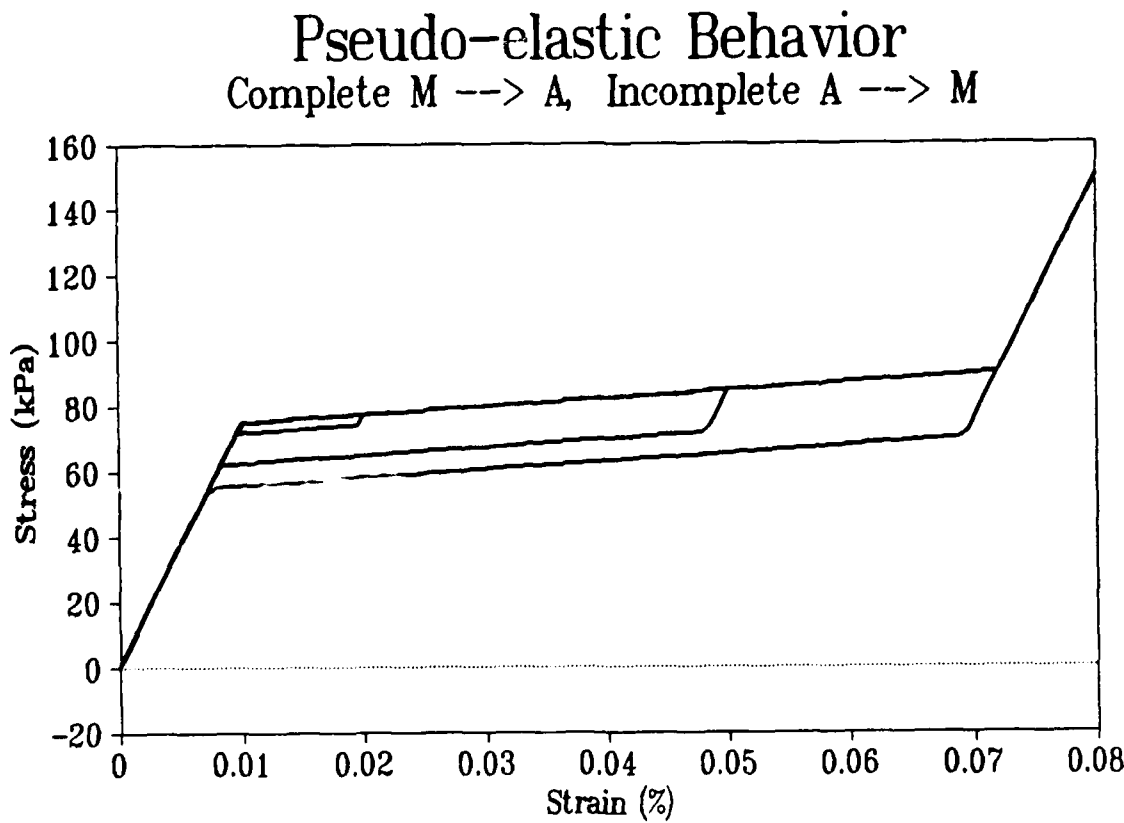


Fig. 3.8.6 Stress Vs strain plot. Complete $M \rightarrow A$ and incomplete $A \rightarrow M$ transformations.

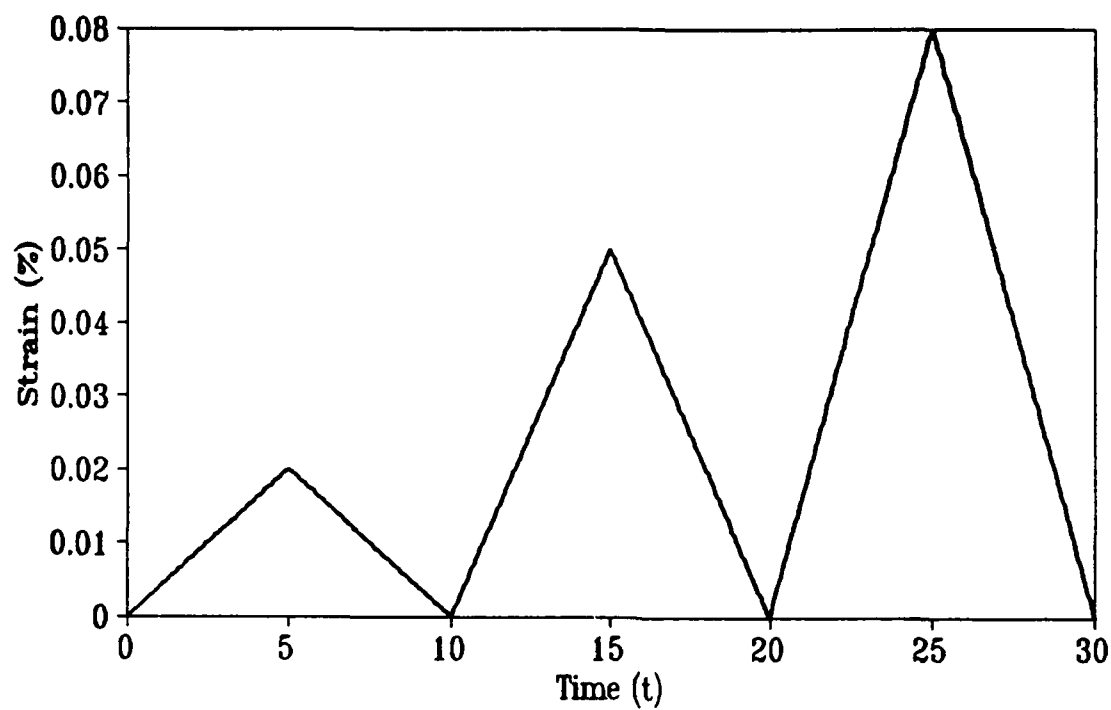


Fig. 3.8.7 Strain Vs time plot. Complete $M \rightarrow A$ and incomplete $A \rightarrow M$ transformations.

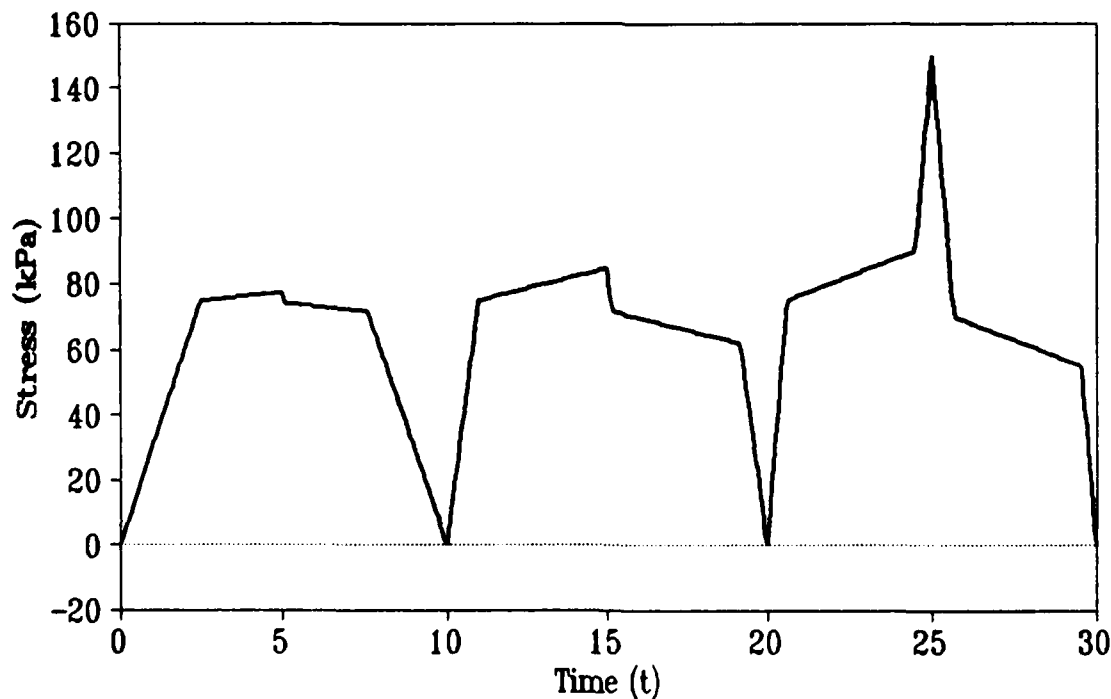


Fig. 3.8.8 Stress Vs time plot. Complete $M \rightarrow A$ and incomplete $A \rightarrow M$ transformations.

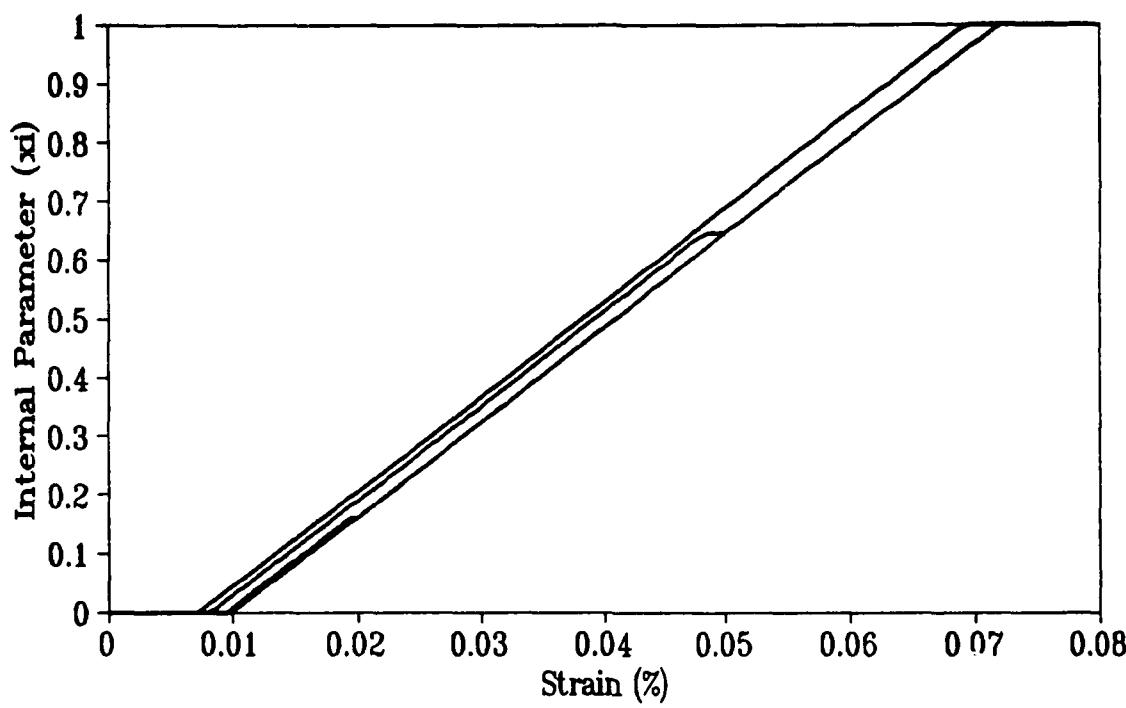


Fig. 3.8.9 Internal parameter Vs strain. Complete $M \rightarrow A$ and incomplete $A \rightarrow M$ transformations.

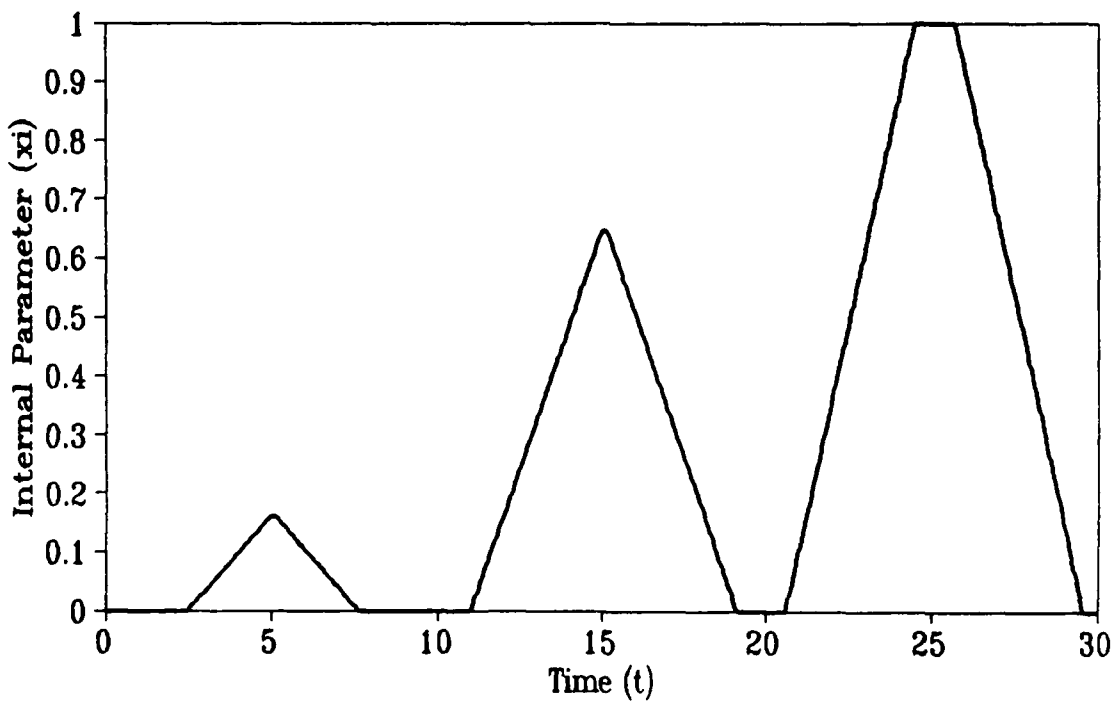


Fig. 3.8.10 Internal parameter Vs time. Complete $M \rightarrow A$ and incomplete $A \rightarrow M$ transformations.

3.8.3 Test 3: Complete $A \rightarrow M$ and incomplete $M \rightarrow A$ transformations

Figure 3.8.11 presents the stress-strain plot for complete $A \rightarrow M$ and incomplete $M \rightarrow A$ transformation. The applied strain as a function of the time parameter is presented next. The specimen is unloaded to zero stress condition at the end of the final loading cycle. Figure 3.8.13 presents the stress variation at a Gauss point as a function of t . Figures 3.8.14–15 show the variation in the internal *phase transformation* parameter ξ as a function of strain ϵ at the Gauss point and of time (t), respectively.

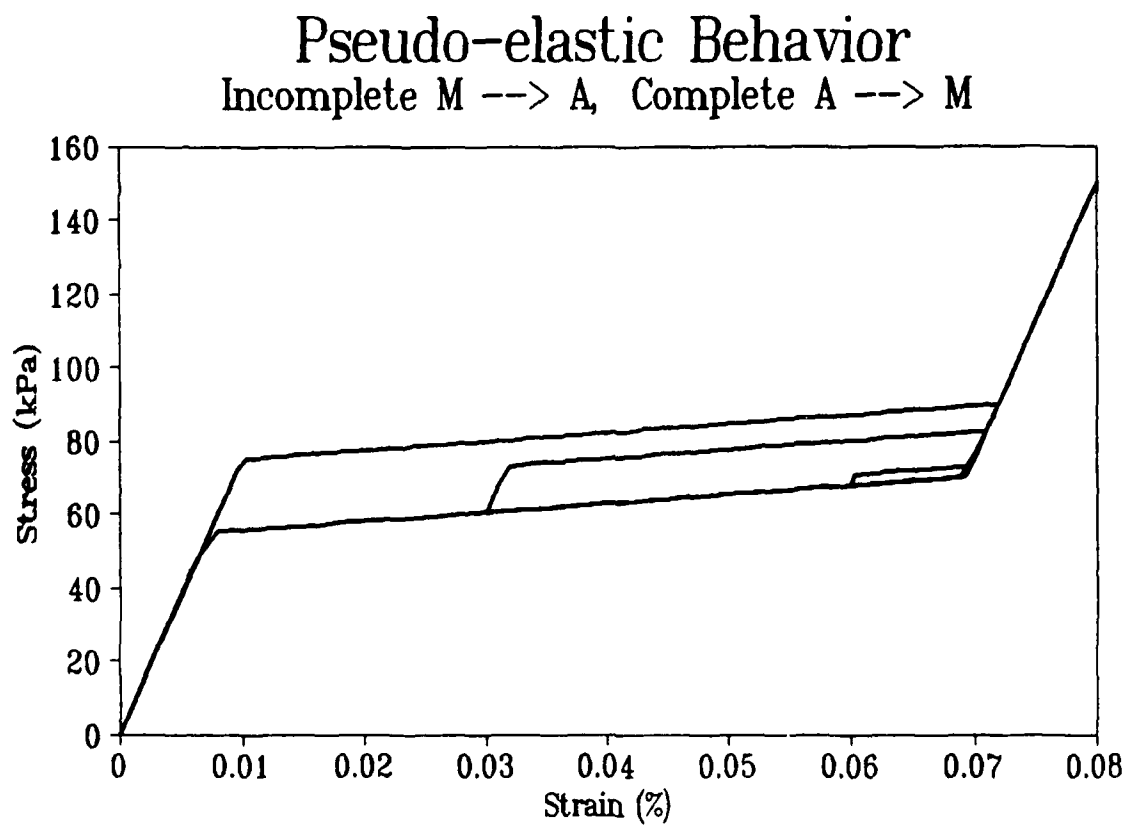


Fig. 3.8.11 Stress Vs strain plot. Incomplete $M \rightarrow A$ and complete $A \rightarrow M$ transformations.

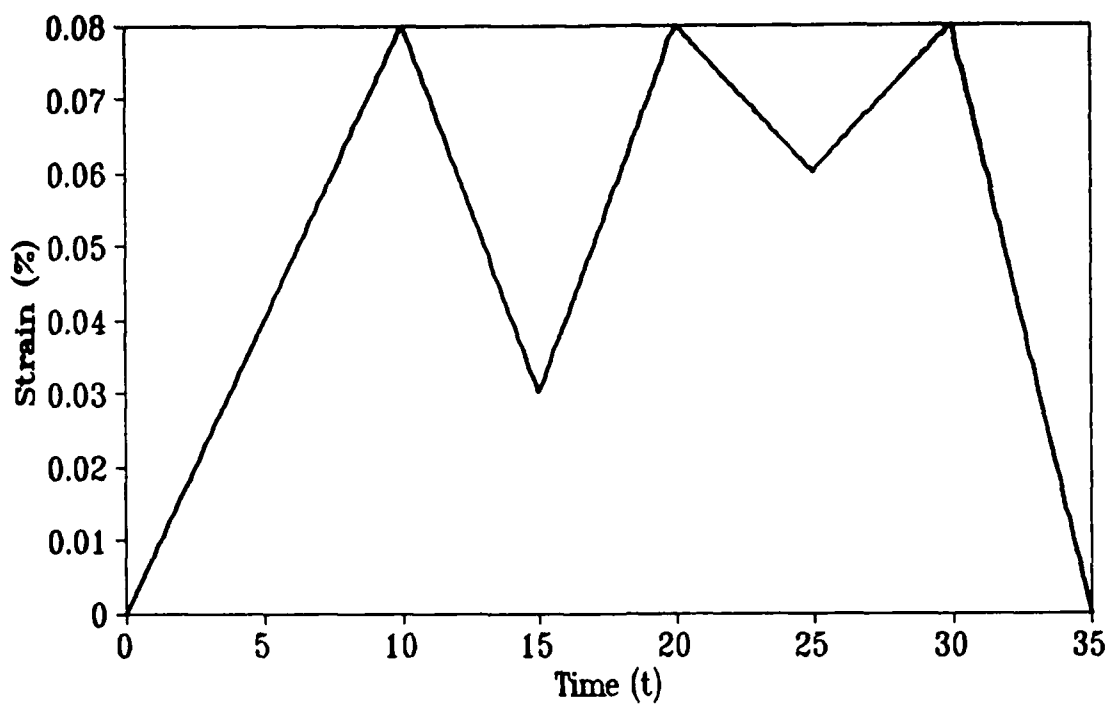


Fig. 3.8.12 Strain Vs time plot. Incomplete $M \rightarrow A$ and complete $A \rightarrow M$ transformations.

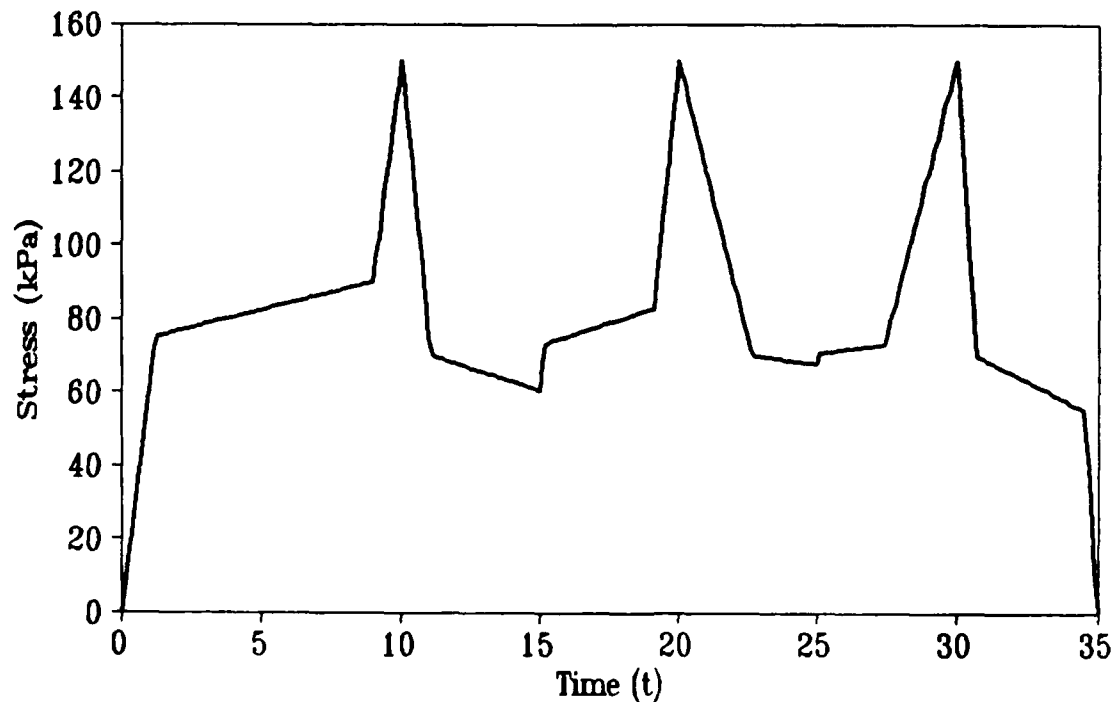


Fig. 3.8.13 Stress Vs time plot. Incomplete $M \rightarrow A$ and complete $A \rightarrow M$ transformations.

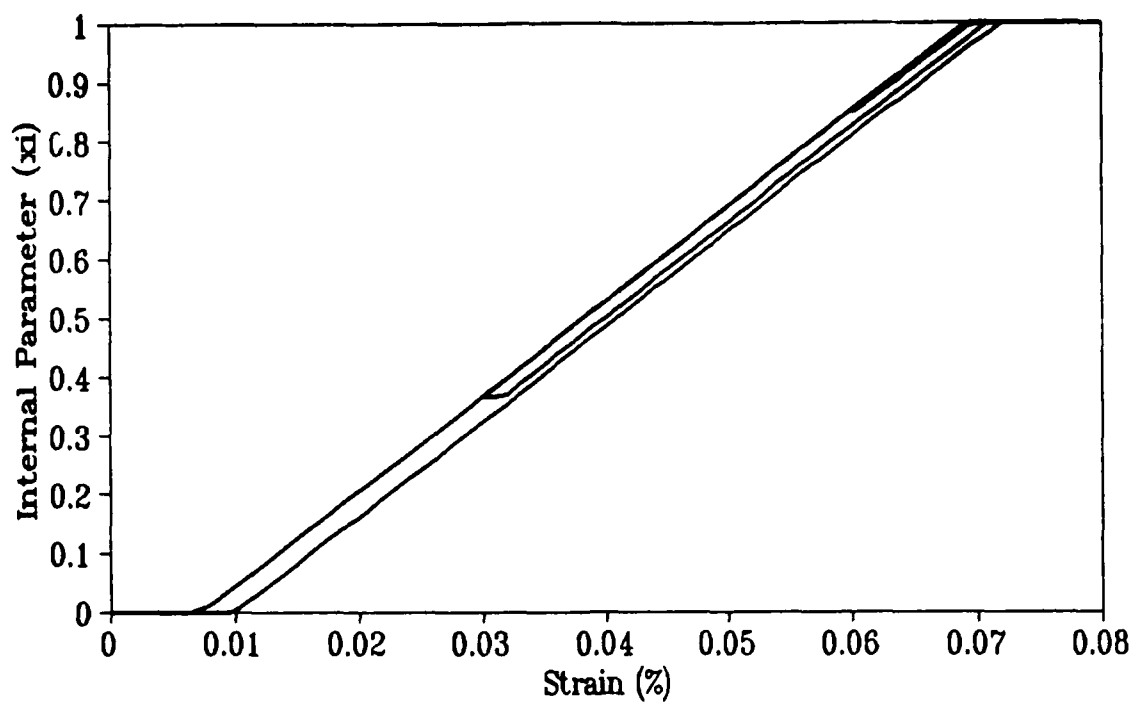


Fig. 3.8.14 Internal parameter Vs strain. Incomplete $M \rightarrow A$ and complete $A \rightarrow M$ transformations.

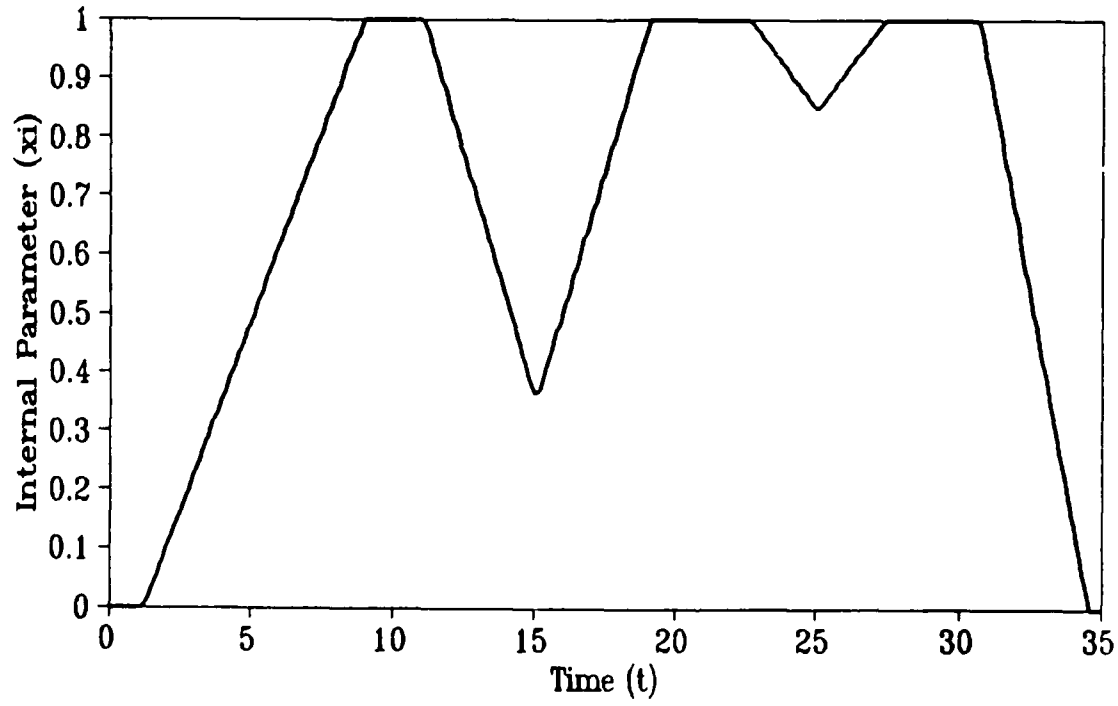


Fig. 3.8.15 Internal parameter Vs time. Incomplete $M \rightarrow A$ and complete $A \rightarrow M$ transformations.

3.8.4 Test 4: Incomplete $A \rightarrow M$ and incomplete $M \rightarrow A$ transformations

Figure 3.8.16 presents the stress-strain plot for incomplete $A \rightarrow M$ and incomplete $M \rightarrow A$ transformations. A random strain loading is applied as a function of the time parameter and the specimen shows a *strong path dependence*, depicted in Fig. 3.8.16. Figure 3.8.18 presents the stress variation at a Gauss point as a function of t . Figures 3.8.14–15 show the variation in the internal *phase transformation parameter* ξ as a function of strain ϵ at the Gauss point and of time (t), respectively.

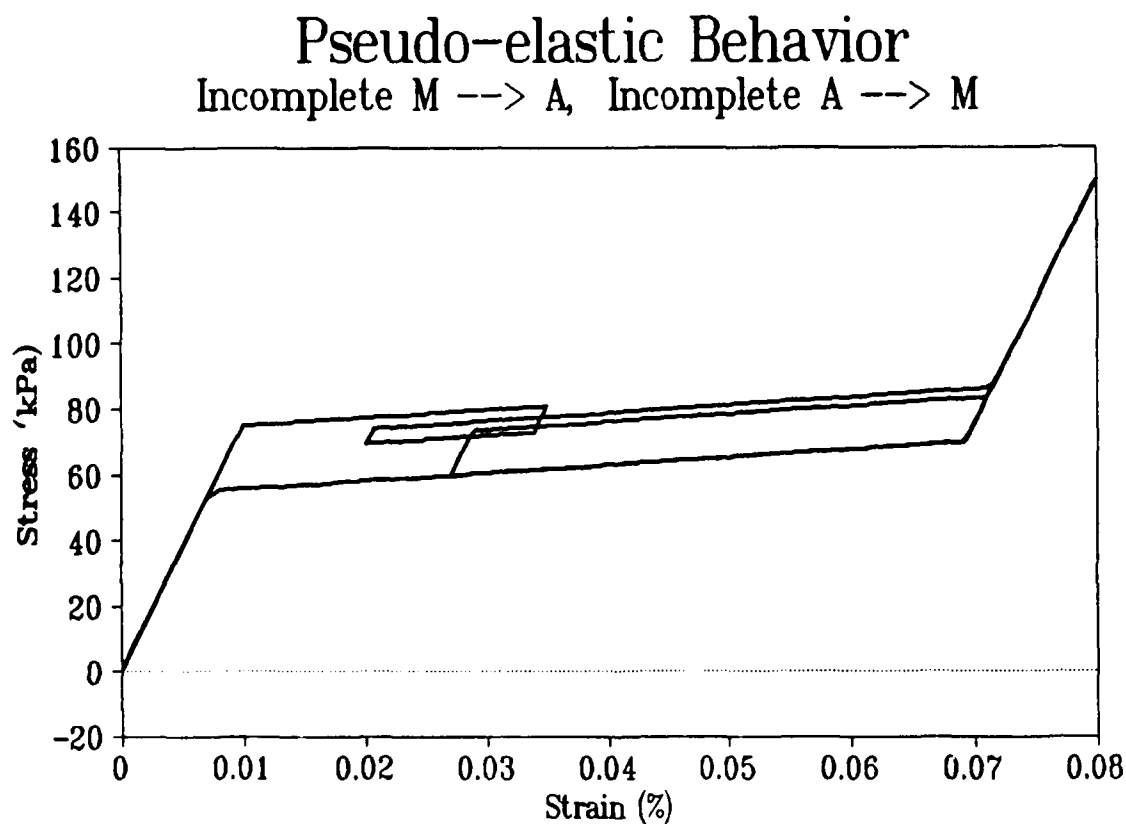


Fig. 3.8.16 Stress Vs strain plot. Incomplete $M \rightarrow A$ and incomplete $A \rightarrow M$ transformations.

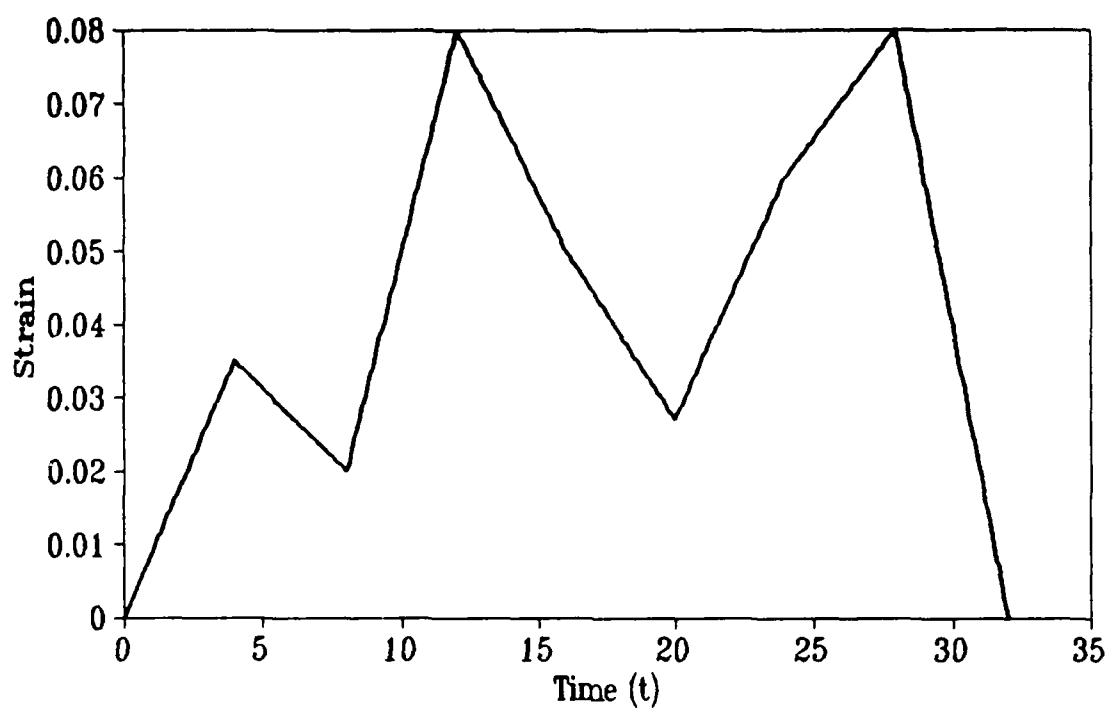


Fig. 3.8.17 Strain Vs time plot. Incomplete $M \rightarrow A$ and incomplete $A \rightarrow M$ transformations.

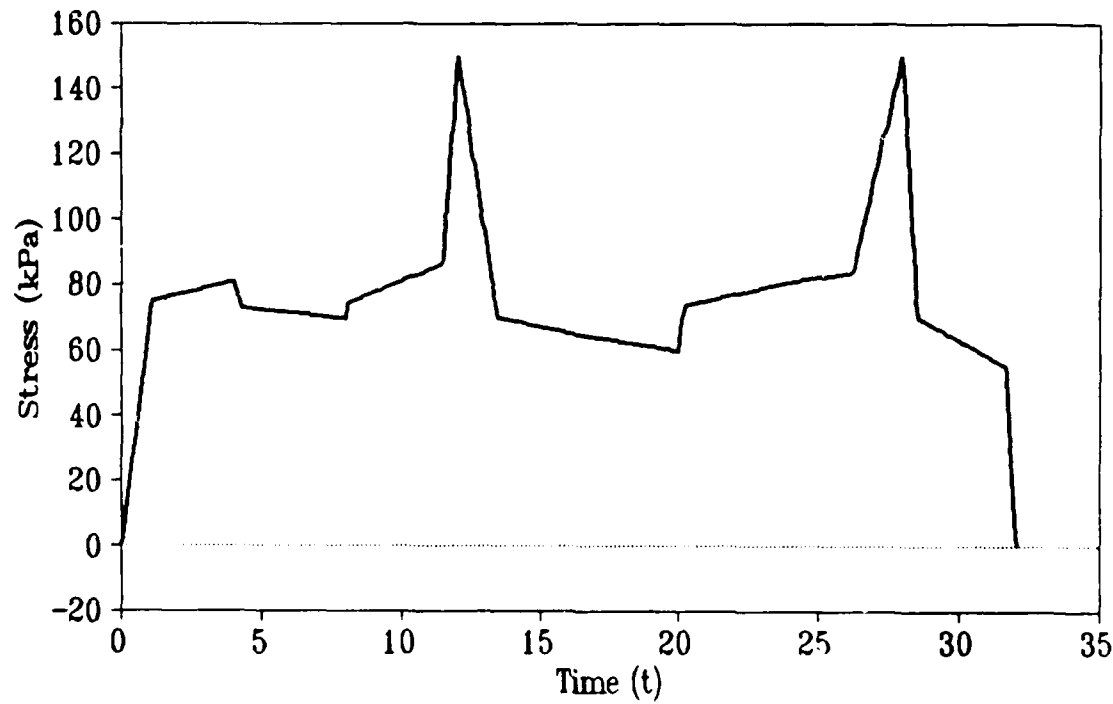


Fig. 3.8.18 Stress Vs time plot. Incomplete $M \rightarrow A$ and incomplete $A \rightarrow M$ transformations.

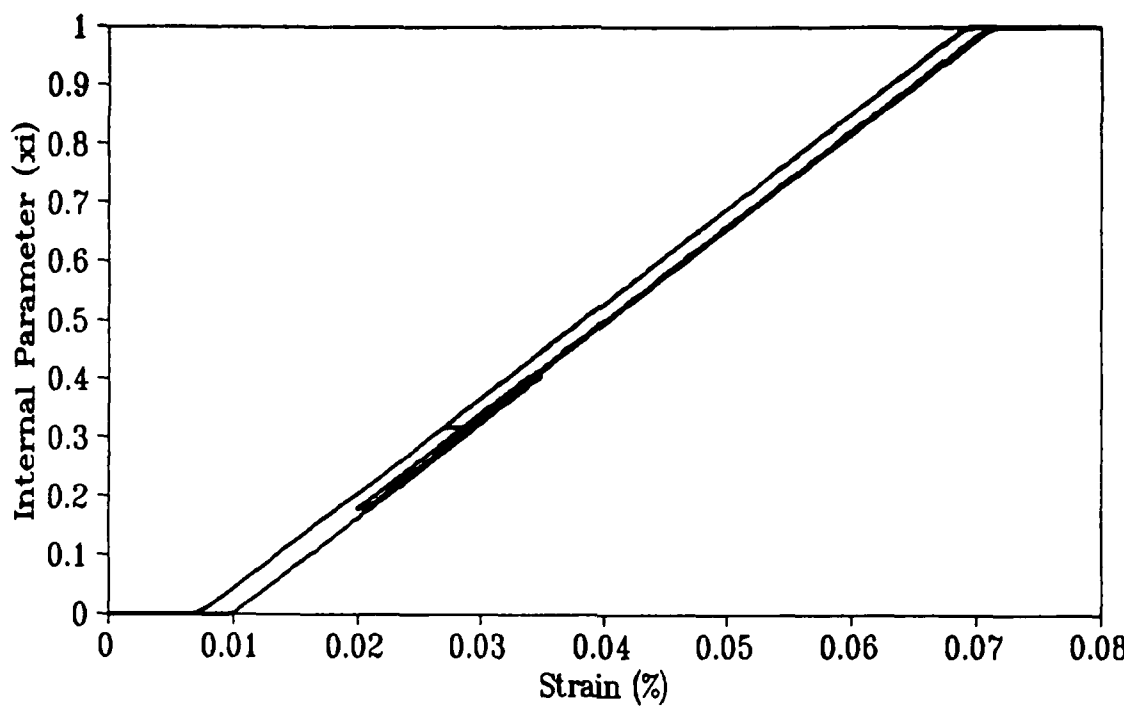


Fig. 3.8.19 Internal parameter Vs strain. Incomplete $M \rightarrow A$ and incomplete $A \rightarrow M$ transformations.

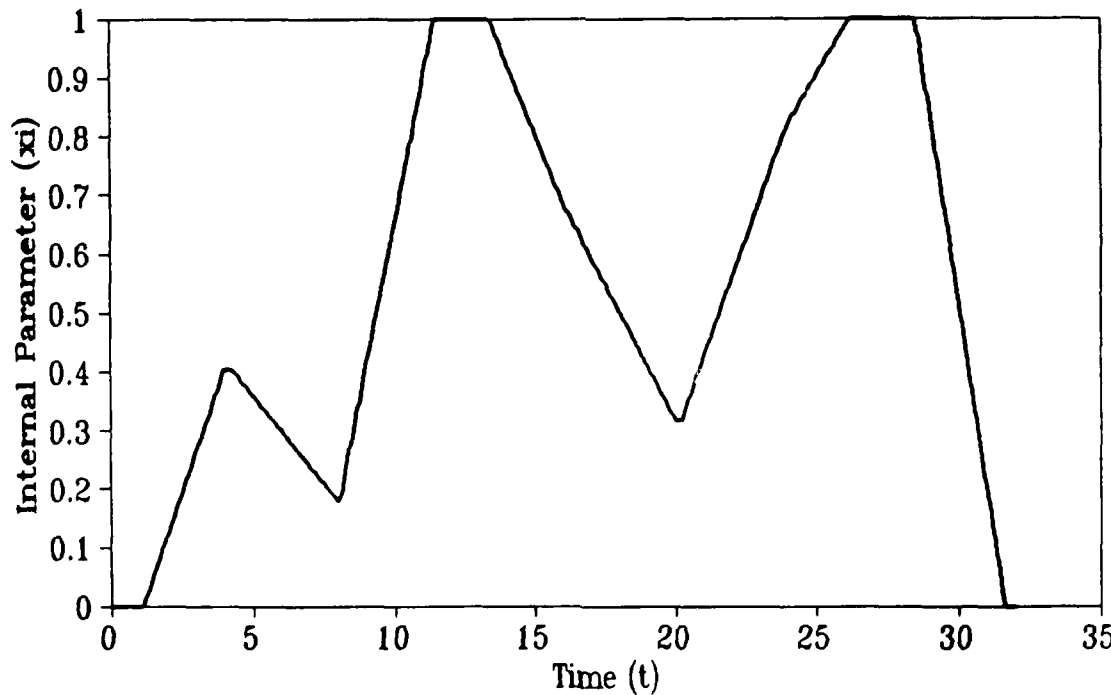


Fig. 3.8.20 Internal parameter Vs time. Incomplete $M \rightarrow A$ and incomplete $A \rightarrow M$ transformations.

CHAPTER 4

A FINITE ELEMENT THEORY FOR COMPOSITE LAMINATES SPECIALIZED TO FLAT GEOMETRIES

4.1 Introduction

In the last two decades, composites have found increasing application in many engineering structures. Recent advances in the technologies of manufacturing and materials have enhanced the current application of composite materials from being used as secondary structural elements to becoming primary load-carrying structural components. Due to the inherent inhomogeneity and anisotropy of the materials, analysis of these composite structures imposes new challenges to engineers (Noor & Burton [1989,1990]).

Plate and shell structures made of laminated composite materials are often modeled as an equivalent single layer using classical laminated theory (C.L.T) (Christensen [1979], Jones [1975], Pagano [1989], Pipes & Pagano [1970]) in which the thickness stress components are ignored. The classical laminate theory is a direct extension of classical plate theory in which the well known Kirchhoff-Love kinematic hypothesis is assumed enforced. This theory is adequate when the thickness (to side or radius ratio) is small. However, laminated plates and shells made of advanced filamentary composite materials are susceptible to thickness effects because their effective transverse moduli are significantly smaller than the effective elastic modulus along the fiber direction. Furthermore, the classical theory of plates which assumes that the normals to the midplane before deformation remain straight and normal to the plane after deformation, underpredicts deflections and overpredicts natural frequencies and buckling loads. These discrepancies are due to the neglect of transverse shear strains. The errors in deflection, stresses, natural frequencies, and buckling loads are even higher for plates made of advanced composites. The range

of applicability of the C.L.T. solution has been well established for laminated flat plates (Noor [1989], Pagano [1989], Reddy [1993]). These analyses have indicated that a theory which accounts for the transverse shear deformation effects would be adequate to predict the gross behavior of the laminate.

In order to overcome these deficiencies in C.L.T., refined laminate theories have been proposed (Byun & Kapania [1992], Noor & Burton [1989], Reddy [1984, 1993], Robbins et al. [1991], Whitney [1970]). These are single layer theories in which the transverse shear stresses are taken into account. They provide improved global response estimates for deflections, vibration frequencies and buckling loads of moderately thick composites when compared to the classical laminate theory. A Mindlin type first-order transverse shear deformation theory (S.D.T.) was first developed by Whitney and Pagano [1970] for multilayered anisotropic plates, and by Dong and Tso [1972] for multilayered anisotropic shells. Both approaches (C.L.T. and S.D.T.) consider all layers as one equivalent single anisotropic layer; thus they are inadequate to model the warping of cross-sections, that is, the distortion of the deformed normal due to transverse shear stresses. Furthermore, the assumption of nondeformable normal results in incompatible shearing stresses between adjacent layers. The later approach also requires the introduction of an arbitrary shear correction factor which is dependent on the lamination parameters for obtaining accurate results.

The exact analyses performed by Pagano [1970, 1973, 1989] on the composite flat plates have indicated that the distortion of the deformed normal is dependent not only on the laminate thickness, but also on the orientation and the degree of orthotropy of the individual layers. Therefore the hypothesis of nondeformable normals, while acceptable for isotropic plates and shells is often quite unacceptable for multilayered anisotropic plates and shells with very large ratio of Young's modulus to shear modulus, even if they are relatively thin (Chang et al. [1990], Reddy [1989, 1993]). Thus a *transverse shear defor-*

mation theory which also accounts for the distortion of the deformed normal is required for accurate prediction of the elastic linear behavior (deflections, thickness distribution of the in-plane displacements, natural frequencies, etc.) of multilayered anisotropic plates and shells.

In view of these issues a variationally sound theory that accounts for the 3-D effects, allows thickness variation, and permits the warping of the deformed normal is required for refined and accurate analysis of thick and thin composites. Embedding of shape memory alloys and study of its interaction with composite laminates only in the context of such a theory will be feasible.

4.2 New Ideas Proposed in the Present Theory

This section presents the noteworthy attributes of the proposed theory that directly address some of the technical drawbacks present in most of the finite element theories that have been proposed for composite analysis.

- (i) The displacement field is continuous through the thickness of the composite while the rotation field is layer-wise continuous (in 2-D) and can be discontinuous across the finite element layers through the thickness direction. This displacement field fulfills *a priori* the geometric continuity conditions between contiguous layers.
- (ii) The assumed displacement field is capable of modeling the distortion of the deformed normal, without increasing the order of the partial differential equations with respect to the first-order transverse shear deformation theory.
- (iii) The assumed displacement field has a 3-D feature, thereby modeling accurately the interlaminar conditions and predicting the 3-D edge effects.
- (iv) Like the shear deformable theory the proposed composite shell theory provides flexibility in the specification of the boundary conditions, Hughes [1987].
- (v) In this theory, at most, only first derivatives of displacement and rotation fields appear

in the variational equations. The practical consequence of this fact is that only C^0 continuity of finite element functions is required which is readily satisfied by the family of Lagrange elements, Hughes [1987].

- (vi) It is feasible to employ this formulation for constructing plate and shell finite elements via the *finite element displacement method*, Hughes [1987].

4.3 Assumptions of the Layer-wise Shear Deformable Shell Theory

1. The domain Ω is of the following special form

$$\Omega = \left\{ (x, y, z) \in \mathcal{R}^3 \mid z^{(l)} \in \left[\frac{-t}{2}, \frac{t}{2} \right]^{(l)}, T = \sum_l z^{(l)}, (x, y)^{(l)} \in A^{(l)} \subset \mathcal{R}^2 \right\} \quad (4.1)$$

where $A^{(l)}$ is the area of the reference surface for layer ' l ' and T is the total thickness of the composite shell.

2. The displacement field is assumed to take the following form

$$U_{\alpha}^{(l)}(x, y, z) = u_{\alpha}^{(l)}(x, y, z) + z^{(l)} \zeta \theta_{\alpha}^{(l)}(x, y) \quad (4.2)$$

where $u_{\alpha}^{(l)}(x, y, z)$ are the translations and $\theta_{\alpha}^{(l)}(x, y)$ are the out of plane director rotations for the l^{th} layer reference surface, and $\zeta \in]0, 1[$ is a parameter that establishes the position of a point from the reference surface.

3. The displacement field in the thickness direction is assumed to be a function of z , i.e.,

$$U_3^{(l)} = u_3(x, y, z) \quad (4.3)$$

and by virtue of this assumption the transverse displacement, U_3 , does vary through the thickness, thereby producing through the thickness strains which result in thickness variation in the shell.

4. As a consequence of the above relaxation

$$\sigma_{33} \neq 0 \quad (4.4)$$

i.e., we do not invoke the plane stress hypothesis.

5. We know from the elasticity theory that the displacements and stresses at the interface between l^{th} and $(l+1)^{st}$ bounded layers must satisfy the following contact conditions.

$$U_{\alpha}^{(l)} = U_{\alpha}^{(l+1)} \quad (4.5)$$

$$U_3^{(l)} = U_3^{(l+1)} \quad (4.6)$$

In addition, the following stress conditions need to be satisfied

$$\tau_{\alpha 3}^{(l)} = \tau_{\alpha 3}^{(l+1)} \quad (4.7)$$

$$\tau_{33}^{(l)} = \tau_{33}^{(l+1)} \quad (4.8)$$

where $\tau_{\alpha \beta}^{(l)}$ denotes the interlaminar stress for layer l .

A consequence of the second assumption is that each finite element layer is associated with non-normal cross-sectional rotations in accordance with the Mindlin kinematic assumption. Another consequence of the second assumption is that it results in independent shear deformation of the director in each layer and allows the warping of the composite cross-section. It also results in discontinuous strain fields across the different material sets, thereby creating the provision of stress continuity across the material interfaces. Consequently, equations (4.7) and (4.8) are inherently satisfied.

4.4 Kinematic Description of Multi-layered Shells

Figure 4.1 shows a composite laminate with 'm' number of material layers. (In Fig. 4.1, $m = 3$). Consequently, the total thickness T is divided into 'm' finite elements through the thickness. Each layer of finite elements is associated with a reference surface which, for ease of discussion, is assumed to be coincident with the lower surface of that layer. It is important to note that the director rotation (i.e., θ_{α}) and the slope (i.e., $u_{3,\alpha}$) are not necessarily the same and thus transverse shear strains are accommodated. This is to be contrasted with the classical lamination theories (C.L.T.) in which $\theta_{\alpha} = u_{3,\alpha}$ and

therefore the transverse shear strains are zero. Within each layer (of finite elements), the director rotates by $\theta_{\alpha}^{(l)}$, generating shear strain $\gamma_{\alpha 3}^{(l)}$. Consequently, in the deformed configuration, node 2 (see Fig. 4.1) moves to location 2'. Now, the director in the second layer rotates by an angle $\theta_{\alpha}^{(l+1)}$, generating shear strain $\gamma_{\alpha 3}^{(l+1)}$. This kinematics repeats in the successive layers and due to the continuity of the displacement field in the thickness direction we obtain the new locations of finite element nodal points as 1', 2', 3' and 4'. This new location of points produces a higher order variation of displacement field through the thickness direction, and thus precludes the need for introducing arbitrary polynomial expressions to model the higher order variation of displacement field through the thickness.

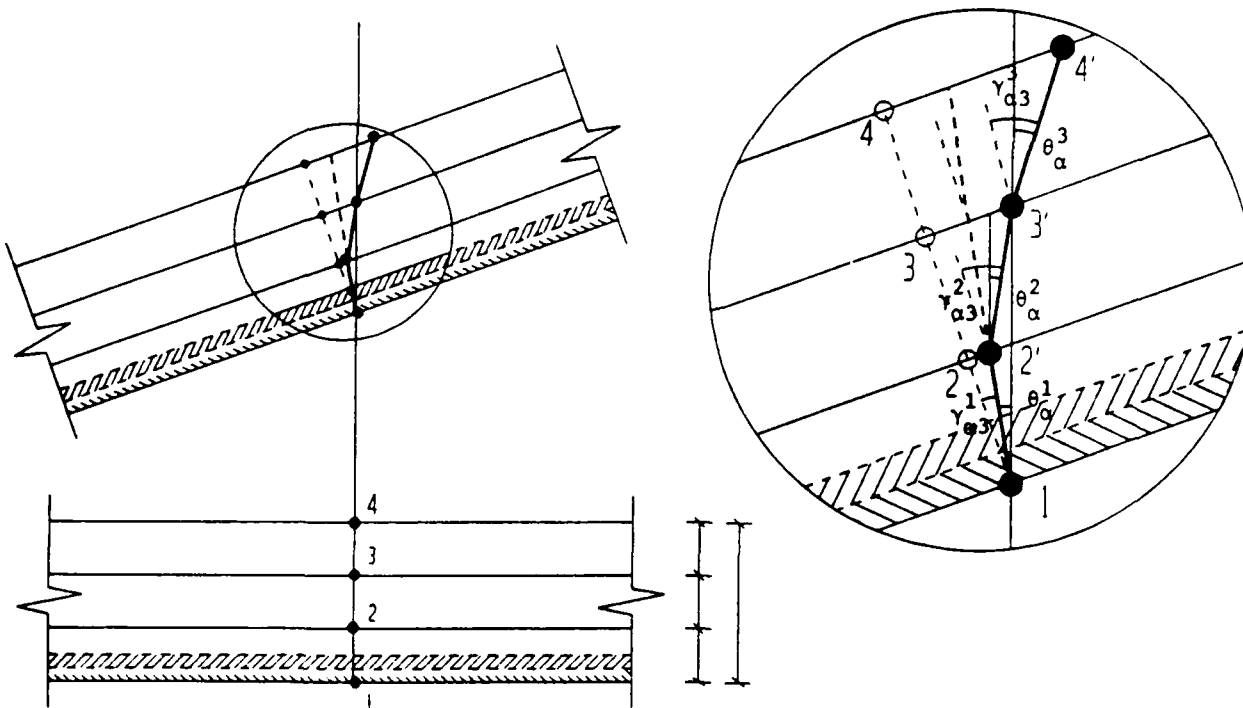


Figure 4.1 Shell kinematics. Variation of transverse shear strains through the thickness.

4.4.1 Kinematics in the context of finite element method

The displacement of the shell is defined by the following relations

$$\mathbf{u}^{(l)}(\xi, \eta, \zeta) = \bar{\mathbf{u}}^{(l)}(\xi, \eta) + \mathbf{U}^{(l)}(\xi, \eta, \zeta) \quad (4.9)$$

$$\bar{\mathbf{u}}^{(l)}(\xi, \eta) = \sum_{a=1}^{n_{en}} N_a(\xi, \eta) \bar{\mathbf{u}}_a^{(l)} \quad (4.10)$$

$$\mathbf{U}^{(l)}(\xi, \eta, \zeta) = \sum_{a=1}^{n_{en}} N_a(\xi, \eta) \mathbf{U}_a^{(l)}(\zeta) \quad (4.11)$$

$$\mathbf{U}_a^{(l)}(\zeta) = Z_a^{(l)}(\zeta) \tilde{\mathbf{U}}_a^{(l)} \quad (\text{no sum}) \quad (4.12)$$

where

$\mathbf{u}^{(l)}$: is the displacement of a generic point in the shell layer l ,

$\bar{\mathbf{u}}^{(l)}$: is the displacement of a point on the reference surface of the shell layer l ,

$\mathbf{U}^{(l)}$: is the 'director displacement' for the shell layer l , and

$Z^{(l)}$: is the thickness function.

The director nodal displacement vector is constructed so that the director can rotate and stretch, shown by an additive decomposition as follows

$$\tilde{\mathbf{U}}_a^{(l)} = \hat{\mathbf{U}}_a^{(l)} + \tilde{\mathbf{U}}_a^{(l)} \quad (4.13)$$

The through thickness stretch component can be expressed as

$$\tilde{\mathbf{U}}_a^{(l)} = (\bar{\mathbf{u}}_{a3} - \bar{\mathbf{u}}_{(a+n_{en})3}) \mathbf{e}_{a3}^{(l)f} \quad (4.14)$$

where $\bar{\mathbf{u}}_{a3}$ and $\bar{\mathbf{u}}_{(a+n_{en})3}$ are the translations in the thickness direction of the lower and upper surfaces belonging to layer ' l '. The out of plane rotation component of the director is constructed such that it may rotate, viz.,

$$\hat{\mathbf{U}}_a^{(l)} = \theta_{a2}^{(l)} \mathbf{e}_{a1}^{(l)f} - \theta_{a1}^{(l)} \mathbf{e}_{a2}^{(l)f} \quad (4.15)$$

The quantities $\theta_{a1}^{(l)}$ and $\theta_{a2}^{(l)}$ represent the rotations of the director about the basis vectors $e_{a1}^{(l)f}$ and $e_{a2}^{(l)f}$, for shell layer l , respectively.

4.5 Geometric Description of Multi-layered Shells

Figure 4.2 shows a typical configuration of a doubly curved composite shell. It can be made of numerous plies with variable material properties, ply orientations and ply thicknesses. In the proposed modeling of the mechanics of shell, no such assumption has been made which would limit the number of individual plies, ply thicknesses, their orientation or their stacking sequence.

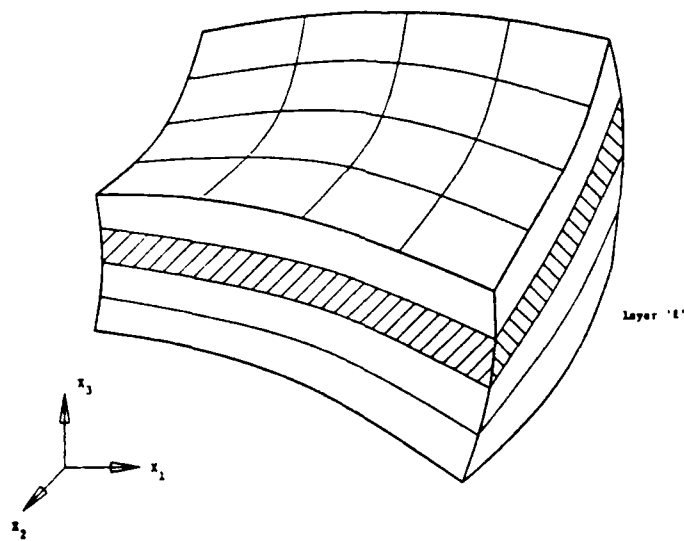


Figure 4.2 Micro and macro structure of the composite.

Let us concentrate our attention to the case in which the composite is composed of four laminates (see Fig. 4.3), each being modeled via a finite element layer. Figure 4.3 shows a schematic diagram of the geometry of an individual layer

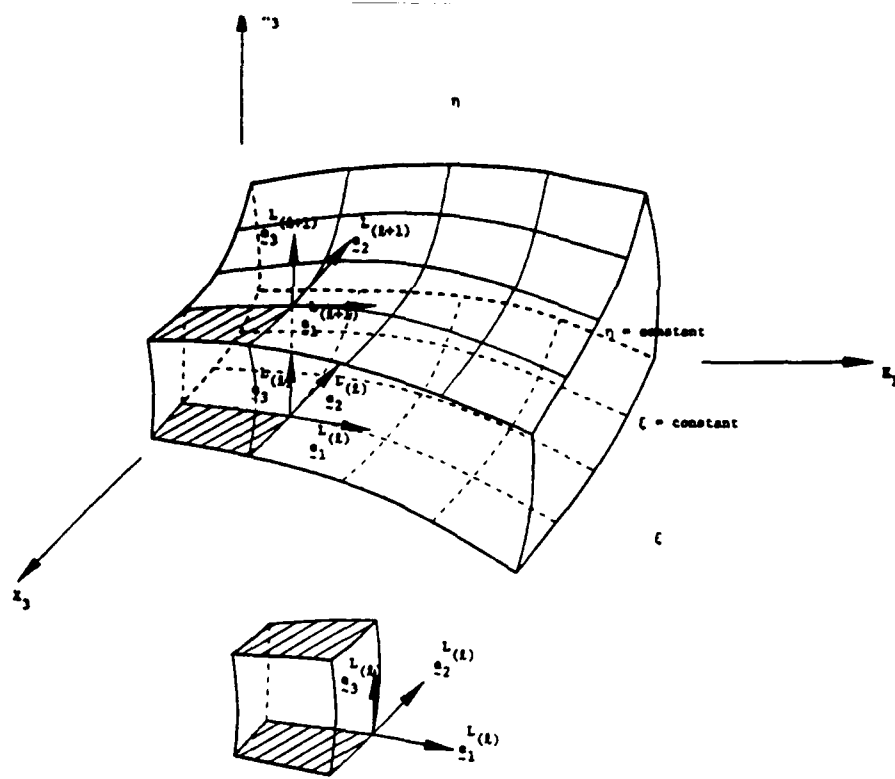


Figure 4.3 Geometric description of an individual layer.

4.5.1 Geometric description in the context of the finite element method

The geometry of a typical laminate of the composite shell element is defined by the following relations

$$\mathbf{z}^{(l)}(\xi, \eta, \zeta) = \bar{\mathbf{z}}^{(l)}(\xi, \eta) + \mathbf{X}^{(l)}(\xi, \eta, \zeta) \quad (4.16)$$

$$\bar{\mathbf{z}}^{(l)}(\xi, \eta, \zeta) = \sum_{a=1}^{n_a} N_a(\xi, \eta) \bar{\mathbf{z}}_a^{(l)} \quad (4.17)$$

$$\mathbf{X}^{(l)}(\xi, \eta, \zeta) = \sum_{a=1}^{n_a} N_a(\xi, \eta) \mathbf{X}_a^{(l)}(\zeta) \quad (4.18)$$

$$\mathbf{X}_a^{(l)}(\zeta) = Z_a^{(l)}(\zeta) \hat{\mathbf{X}}_a^{(l)} \quad (\text{no sum}) \quad (4.19)$$

$\mathbf{z}^{(l)}$: the position vector of a generic point of the shell for layer l ,

$\bar{\mathbf{z}}^{(l)}$: the position vector of a point in the reference surface for layer l ,

$\mathbf{X}^{(l)}$: a position vector of a generic point relative to $\bar{\mathbf{z}}^{(l)}$ which defines the director through the point for layer l . (In computational shell literature, $\mathbf{X}^{(l)}$ is referred to as fiber direction),

$\bar{\mathbf{x}}_a^{(l)}$: the position vector of nodal point 'a' in layer l ,

N_a : two-dimensional shape function associated with node 'a',

n_{en} : the number of element nodes in the reference surface of layer l ,

$\hat{\mathbf{X}}_a^{(l)}$: a unit vector emanating from node 'a' in the director direction,

Z_a : a 'thickness function' associated with node 'a', which is defined by the location of the reference surface.

The above relations represent a smooth mapping of the biunit cube into the physical shell domain. For ' ζ ' fixed, the surface defined by (4.16) is called a *lamina* and for $\{\xi, \eta\}$ fixed, the line described by (4.16) is called the *director*. The director is, in general, not perpendicular to the laminae. Sometimes the director is referred to as the 'pseudonormal'.

For a particular choice of two-dimensional shape functions, eqs. (4.16)-(4.19) are precisely defined upon specification of $\bar{\mathbf{x}}_a^{(l)}$, $\hat{\mathbf{X}}_a^{(l)}$, $Z_a^{(l)+}$ and $Z_a^{(l)-}$ ($a = 1, 2, \dots, n_{en}$). It is convenient in practice to take as input the coordinates of the top and bottom surfaces of the shell layer along each nodal director ($\mathbf{x}_a^{(l)+}$ and $\mathbf{x}_a^{(l)-}$, respectively) and a parameter $\bar{\zeta} \in [-1, +1]$, which defines the location of the reference surface. For example if $\bar{\zeta} = -1, 0, +1$ (respectively), then the reference surface is taken to be the bottom, middle, top (respectively) of the shell layer l . From these data we may calculate

$$\bar{\mathbf{x}}_a^{(l)} = \frac{1}{2}(1 - \bar{\zeta})\mathbf{x}_a^{(l)-} + \frac{1}{2}(1 + \bar{\zeta})\mathbf{x}_a^{(l)+} \quad (4.20)$$

$$\hat{\mathbf{X}}_a^{(l)} = \frac{\mathbf{x}_a^{(l)+} - \mathbf{x}_a^{(l)-}}{\|\mathbf{x}_a^{(l)+} - \mathbf{x}_a^{(l)-}\|} \quad (4.21)$$

$$Z_a^{(l)}(\zeta) = \frac{1}{2}(1 + \zeta)Z_a^{(l)+} + \frac{1}{2}(1 - \zeta)Z_a^{(l)-} \quad (4.22)$$

where $\|\cdot\|$ denotes the Euclidean norm (i.e., $\|\mathbf{x}\| = (x_1^2 + x_2^2 + x_3^2)^{1/2}$).

4.5.2 Lamina coordinate system

At each integration point in the element a Cartesian reference frame is erected so that two axes are tangent to the lamina through the point. The frame is defined by its

orthonormal basis vectors e_1^L, e_2^L, e_3^L in which e_3^L is perpendicular to the lamina. The basis vectors are calculated as follows

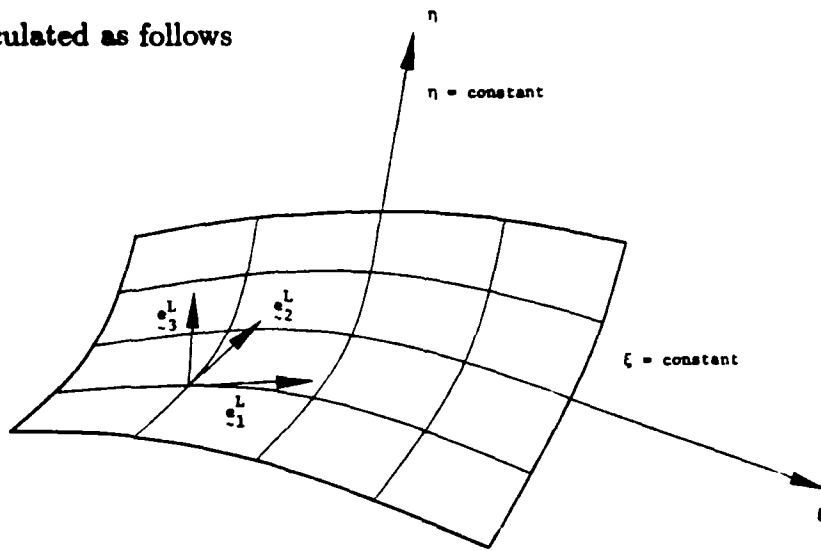


Figure 4.4 Typical lamina coordinate system (ζ = constant surface)

Construct unit tangent vectors to the ξ - and η - coordinate directions:

$$e_\xi^{(l)} = \frac{\mathbf{x}_{,\xi}^{(l)}}{\|\mathbf{x}_{,\xi}^{(l)}\|} \quad (4.23)$$

$$e_\eta^{(l)} = \frac{\mathbf{x}_{,\eta}^{(l)}}{\|\mathbf{x}_{,\eta}^{(l)}\|} \quad (4.24)$$

Consequently

$$e_3^L = \frac{e_\xi^{(l)} \times e_\eta^{(l)}}{\|e_\xi^{(l)} \times e_\eta^{(l)}\|} \quad (4.25)$$

The vectors tangent to the lamina are selected so that the angle between e_1^L and $e_\xi^{(l)}$ is the same as the angle between $e_\eta^{(l)}$ and e_2^L and so that the e_1^L, e_2^L -basis is as 'close' as possible to the $e_\xi^{(l)}, e_\eta^{(l)}$ basis. Thus

$$e_1^L = \frac{\sqrt{2}}{2} (e_\alpha^{(l)} - e_\beta^{(l)}) \quad (4.26)$$

$$e_2^L = \frac{\sqrt{2}}{2} (e_\alpha^{(l)} + e_\beta^{(l)}) \quad (4.27)$$

where

$$e_\alpha^{(l)} = \frac{\frac{1}{2}(e_\xi^{(l)} + e_\eta^{(l)})}{\|\frac{1}{2}(e_\xi^{(l)} + e_\eta^{(l)})\|} \quad (4.28)$$

$$\mathbf{e}_\beta^{(l)} = \frac{\mathbf{e}_3^L \times \mathbf{e}_\alpha^{(l)}}{\|\mathbf{e}_3^L \times \mathbf{e}_\alpha^{(l)}\|} \quad (4.29)$$

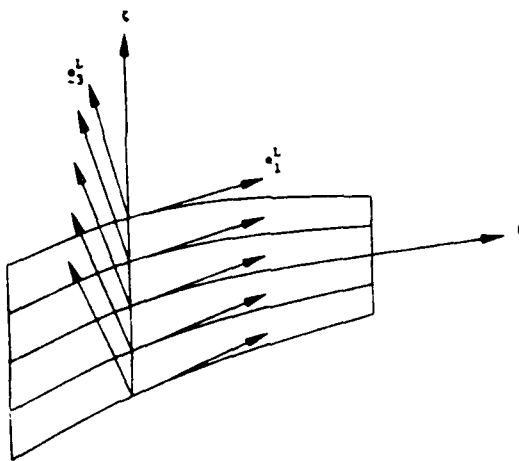


Figure 4.5 $\eta = \text{constant}$ surface.

Furthermore, we also define the orthogonal matrix to transform quantities from the global coordinate system to the lamina system

$$\mathbf{q} = [q_{ij}] = [\mathbf{e}_1^L \ \mathbf{e}_2^L \ \mathbf{e}_3^L]^T \quad (4.30)$$

For the present case

$$\mathbf{e}_1^L = \mathbf{A}_1, \quad \mathbf{e}_2^L = \mathbf{A}_2, \quad \mathbf{e}_3^L = \mathbf{D} \quad (4.31)$$

4.6 Constitutive Relations

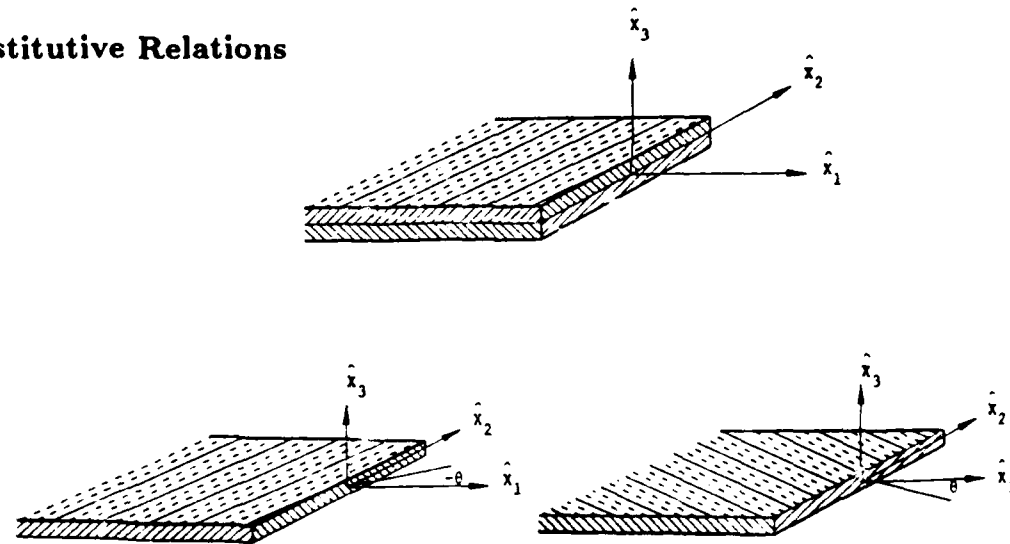


Figure 4.6 Schematic diagram of a composite and its constituent laminates.

Suppose the composite is made of two laminates of the same material but oriented at $+\theta$ and $-\theta$ degrees with respect to the extension direction. Let $C_{(\alpha)}$ represent the C matrix (constitutive matrix) for the laminate with regard to its mutually perpendicular planes of elastic symmetry. In general it can be written as

$$C_{(\alpha)} = \begin{bmatrix} C_{11} & C_{12} & C_{13} & 0 & 0 & C_{16} \\ C_{12} & C_{22} & C_{23} & 0 & 0 & C_{26} \\ C_{13} & C_{23} & C_{33} & 0 & 0 & C_{36} \\ 0 & 0 & 0 & C_{44} & C_{45} & 0 \\ 0 & 0 & 0 & C_{45} & C_{55} & 0 \\ C_{16} & C_{26} & C_{36} & 0 & 0 & C_{66} \end{bmatrix} \quad (4.32)$$

where α represents the laminate in the composite.

Let X_1 represent the direction along the loading for the composite element and let X_3 represent its thickness direction. This axis is assumed to be perpendicular to the plane of elastic symmetry. The $C(\alpha)$ for a laminate can be projected from its mutually perpendicular planes of elastic symmetry onto the composite coordinate system (X_1, X_2, X_3) about the X_3 axis via the following transformation matrix.

$$Q_{(\alpha)} = \begin{bmatrix} C^2 & S^2 & 0 & 0 & 0 & CS \\ S^2 & C^2 & 0 & 0 & 0 & -CS \\ 0 & 0 & 1 & 0 & 0 & 0 \\ 0 & 0 & 0 & C & -S & 0 \\ 0 & 0 & 0 & S & C & 0 \\ -2CS & 2CS & 0 & 0 & 0 & (C^2 - S^2) \end{bmatrix} \quad (4.33)$$

where $C = \cos \theta$, $S = \sin \theta$. The transformed constitutive matrix is obtained as

$$C'_{(\alpha)} = Q_{(\alpha)}^T C_{(\alpha)} Q_{(\alpha)}$$

In general, $C'_{(\alpha)}$ will have the following form

$$C'_{(\alpha)} = \begin{bmatrix} C'_{11} & C'_{12} & C'_{13} & 0 & 0 & C'_{16} \\ C'_{12} & C'_{22} & C'_{23} & 0 & 0 & C'_{26} \\ C'_{13} & C'_{23} & C'_{33} & 0 & 0 & C'_{36} \\ 0 & 0 & 0 & C'_{44} & C'_{45} & 0 \\ 0 & 0 & 0 & C'_{45} & C'_{55} & 0 \\ C'_{16} & C'_{26} & C'_{36} & 0 & 0 & C'_{66} \end{bmatrix} \quad (4.34)$$

We evaluate the $C_{(\text{macro elem.})}$, i.e., the constitutive relation for the composite via the expression

$$C_{(\text{macro elem.})} = m C'_{(1)} + (1 - m) C'_{(2)}$$

where $m = \xi_1/\xi_2 < 1$, ($\xi_1 = z(1)$, $\xi_2 = z(1) + z(2)$).

4.7 Finite Element Formulation

4.7.1 Strong form of the problem

The governing field equations of composite laminates are discussed in detail in Panahandeh, Masud and Ghanimati [1993]. To the general equilibrium equations we add the boundary conditions

$$\mathbf{u}_\alpha = \hat{\mathbf{u}}_\alpha \quad \text{on } \Gamma_u \quad (4.35)$$

$$u_3 = \hat{u}_3 \quad \text{on } \Gamma_{u_3} \quad (4.36)$$

$$\theta_\alpha = \hat{\theta}_\alpha \quad \text{on } \Gamma_\theta \quad (4.37)$$

In addition

$$\tau^{\alpha\beta} n_\beta = \bar{\tau}^\alpha \quad \text{on } \Gamma_r^\alpha \quad (4.38)$$

$$q^\alpha n_\alpha = \bar{q} \quad \text{on } \Gamma_q \quad (4.39)$$

$$S^{\alpha\beta} n_\beta = \bar{S}^\alpha \quad \text{on } \Gamma_s \quad (4.40)$$

where $\Gamma_u \cup \Gamma_{u_3}$ represents the boundary where translation boundary conditions are applied; $\Gamma_r^\alpha \cup \Gamma_q$ represents to the boundary where traction boundary conditions are applied; Γ_θ corresponds to the boundary with prescribed rotation, and Γ_s corresponds to the portion of boundary with applied moments.

As usual

$$\mathbf{n} = n_\alpha \mathbf{E}_\alpha \equiv n_\alpha \mathbf{A}_\alpha \quad (4.41)$$

denotes the unit outward normal to the boundary $\partial\Omega$ of domain Ω .

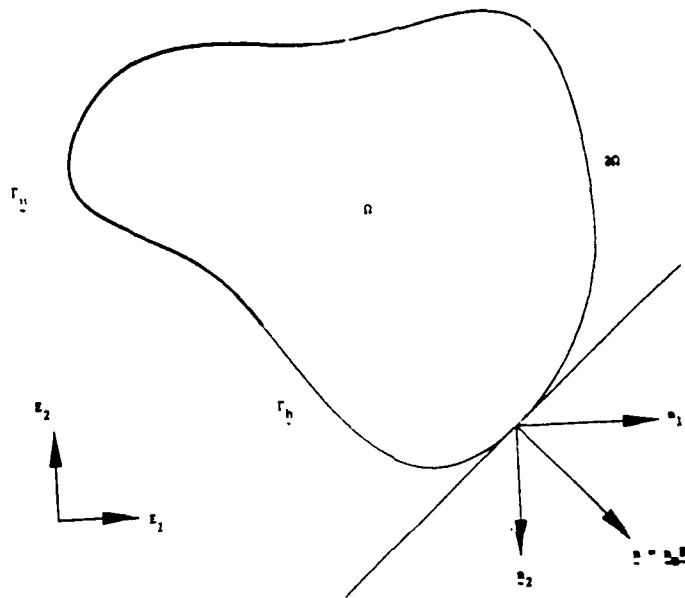


Figure 4.7 Schematic diagram of the domain of computation.

4.7.2 Weak form of the problem

Multiplying the strong form of the problem with the admissible variations, integrating by parts and using the prescribed essential and the natural boundary conditions we arrive at the weak form of the problem. The spaces relevant to the problem are

$$S = \{(\mathbf{u}, u_3, \theta) | (\mathbf{u}, u_3, \theta) \in H^1(\Omega), (\mathbf{u}, u_3, \theta) : S \rightarrow \mathcal{R} \times \mathcal{R} \times \mathcal{R} : \\ \text{s.t. } \mathbf{u} = \hat{\mathbf{u}} \text{ on } \Gamma_u, u_3 = \hat{u}_3 \text{ on } \Gamma_{u_3}, \theta_\alpha = \hat{\theta}_\alpha \text{ on } \Gamma_\theta\} \quad (4.42)$$

and

$$V = \{(\bar{\mathbf{u}}, \bar{u}_3, \bar{\theta}) | (\bar{\mathbf{u}}, \bar{u}_3, \bar{\theta}) \in H_0^1(\Omega), (\bar{\mathbf{u}}, \bar{u}_3, \bar{\theta}) : S \rightarrow \mathcal{R} \times \mathcal{R} \times \mathcal{R} : \\ \text{s.t. } \bar{\mathbf{u}} = \mathbf{0} \text{ on } \Gamma_u, \bar{u}_3 = 0 \text{ on } \Gamma_{u_3}, \bar{\theta}_\alpha = 0 \text{ on } \Gamma_\theta\} \quad (4.43)$$

where S is the space of trial displacements and trial rotations, and V is the associated space of weighting functions, respectively. $H^1(\Omega)$ denotes the space of square-integrable functions along with their generalized derivatives defined over Ω , and $H_0^1(\Omega)$ is the subset of $H^1(\Omega)$ whose members satisfy zero essential boundary conditions.

4.7.3 Finite element matrices and vectors

The finite element stiffness matrix and load vector may be obtained directly from the matrix form of the variational equation. The finite element approximations for \mathbf{u} , $\bar{\mathbf{u}}$, $\boldsymbol{\theta}$ and $\bar{\boldsymbol{\theta}}$ are denoted by \mathbf{u}^h , $\bar{\mathbf{u}}^h$, $\boldsymbol{\theta}^h$ and $\bar{\boldsymbol{\theta}}^h$, respectively. In a typical element, possessing n_{en} nodes,

$$\mathbf{u}^h = \sum_{a=1}^{n_{en}} N_a \mathbf{u}_a^h \quad (4.44)$$

$$\bar{\mathbf{u}}^h = \sum_{a=1}^{n_{en}} N_a \bar{\mathbf{u}}_a^h \quad (4.45)$$

$$\boldsymbol{\theta}^h = \sum_{a=1}^{n_{en}} N_a \boldsymbol{\theta}_a^h \quad (4.46)$$

$$\bar{\boldsymbol{\theta}}^h = \sum_{a=1}^{n_{en}} N_a \bar{\boldsymbol{\theta}}_a^h \quad (4.47)$$

where N_a is the shape function associated with node 'a', \mathbf{u}_a^h , $\bar{\mathbf{u}}_a^h$, $\boldsymbol{\theta}_a^h$, and $\bar{\boldsymbol{\theta}}_a^h$ are the a^{th} nodal values of \mathbf{u}^h , $\bar{\mathbf{u}}^h$, $\boldsymbol{\theta}^h$, and $\bar{\boldsymbol{\theta}}^h$, respectively. It is not necessary to assume that $\boldsymbol{\theta}^h$ and \mathbf{u}^h be defined in terms of the same shape functions and nodal patterns.

4.7.3.1 Stress vectors

The resultant stress vectors for an element which has the 3D-effects of an elasticity element and 2D effects of a shell like element are

$$\hat{\boldsymbol{\tau}} = \begin{Bmatrix} \tau_{11}^{(I)} \\ \tau_{22}^{(I)} \\ \tau_{12}^{(I)} \end{Bmatrix} \quad (\text{inplane}) \quad (4.48)$$

$$\hat{\mathbf{q}} = \begin{Bmatrix} q_1^{(I)} \\ q_2^{(I)} \end{Bmatrix} \quad (\text{shear}) \quad (4.49)$$

$$\hat{\sigma} = \begin{Bmatrix} \sigma_{11}^{(l)} \\ \sigma_{22}^{(l)} \\ \sigma_{12}^{(l)} \end{Bmatrix} \quad (\text{bending}) \quad (4.50)$$

$$\check{\tau} = \left\{ \tau_{33}^{(l)} \right\} \quad (\text{through-thickness}) \quad (4.51)$$

4.7.3.2 Strain vectors

The strain vectors corresponding to the stress vectors are

$$\hat{\epsilon} = \begin{Bmatrix} \gamma_{11}^{(l)} \\ \gamma_{22}^{(l)} \\ 2\gamma_{12}^{(l)} \end{Bmatrix} \quad (\text{inplane}) \quad (4.52)$$

$$\hat{\delta} = \begin{Bmatrix} \gamma_{13}^{(l)} \\ \gamma_{23}^{(l)} \end{Bmatrix} \quad (\text{shear}) \quad (4.53)$$

$$\hat{\kappa} = \begin{Bmatrix} \kappa_{11}^{(l)} \\ \kappa_{22}^{(l)} \\ 2\kappa_{12}^{(l)} \end{Bmatrix} \quad (\text{bending}) \quad (4.54)$$

$$\check{\epsilon} = \left\{ \gamma_{33}^{(l)} \right\} \quad (\text{through-thickness}) \quad (4.55)$$

We can combine equ. (7.3.2.1) and (7.3.2.4) to yield a vector that incorporates 3D effects

$$\epsilon = \begin{Bmatrix} \gamma_{11}^{(l)} \\ \gamma_{22}^{(l)} \\ \gamma_{33}^{(l)} \\ 2\gamma_{12}^{(l)} \end{Bmatrix} \quad (4.56)$$

4.7.3.3 Matrix Differential Operators

The strain vectors can be written in terms of differential operators as follows

$$\boldsymbol{\epsilon} = \begin{Bmatrix} \mathbf{A}_1^T \partial / \partial X^1 \\ \mathbf{A}_2^T \partial / \partial X^2 \\ \mathbf{D}^T \partial / \partial X^3 \\ \mathbf{A}_1^T \partial / \partial X^2 + \mathbf{A}_2^T \partial / \partial X^1 \end{Bmatrix} \mathbf{u} \quad (4.57)$$

For the case of flat geometry and linear analysis, the matrix differential form for the modified membrane effect becomes

$$\mathbf{B}_m = \begin{Bmatrix} \partial / \partial X^1 \\ \partial / \partial X^2 \\ \partial / \partial X^3 \\ \partial / \partial X^2 + \partial / \partial X^1 \end{Bmatrix} \quad (4.58)$$

Similarly, for the shear operator

$$\hat{\boldsymbol{\delta}}_\alpha = \gamma_{\alpha 3} = \frac{1}{2}(u_{3,\alpha} - \theta_\alpha) \quad (4.59)$$

$$= [\mathbf{D}^T \partial / \partial X^\alpha \quad \mathbf{A}_\alpha^T] \begin{Bmatrix} \mathbf{u} \\ \boldsymbol{\theta} \end{Bmatrix} \quad (4.60)$$

Therefore transverse shear strain vector for flat geometries can be specialized to

$$\begin{aligned} \hat{\boldsymbol{\delta}}_\alpha &= [\mathbf{B}_{sm} \quad \mathbf{B}_{sb}] \begin{Bmatrix} \mathbf{u} \\ \boldsymbol{\theta} \end{Bmatrix} \\ &= \begin{bmatrix} \partial / \partial X^1 & \mathbf{A}_1^T \\ \partial / \partial X^2 & \mathbf{A}_2^T \end{bmatrix} \begin{Bmatrix} \mathbf{u} \\ \boldsymbol{\theta} \end{Bmatrix} \end{aligned} \quad (4.61)$$

Following along the same lines, the bending strain vector can be written in terms of matrix differential operators

$$\hat{\boldsymbol{\delta}}_\alpha = [\mathbf{B}_{bm} \quad \mathbf{B}_{bb}] \begin{Bmatrix} \mathbf{u} \\ \boldsymbol{\theta} \end{Bmatrix} \quad (4.62)$$

where

$$\mathbf{B}_{bm} = \begin{Bmatrix} \mathbf{D}_1^T \partial / \partial X^1 \\ \mathbf{D}_2^T \partial / \partial X^2 \\ \mathbf{D}_1^T \partial / \partial X^2 + \mathbf{D}_2^T \partial / \partial X^1 \end{Bmatrix}; \mathbf{B}_{bb} = \begin{Bmatrix} \mathbf{A}_1^T \partial / \partial X^1 \\ \mathbf{A}_2^T \partial / \partial X^2 \\ \mathbf{A}_1^T \partial / \partial X^2 + \mathbf{A}_2^T \partial / \partial X^1 \end{Bmatrix} \quad (4.63)$$

Since for flat geometries $D_{,\alpha} = 0$

$$\hat{\mathbf{B}}_{bm} = [0] ; \quad \mathbf{B}_{bb} = \begin{bmatrix} \partial/\partial X^1 \\ \partial/\partial X^2 \\ \partial/\partial X^2 + \partial/\partial X^1 \end{bmatrix} \quad (4.64)$$

Finally, a total matrix differential operator \mathbf{B} can be defined which produces the total strain vector $\tilde{\boldsymbol{\epsilon}}$ when applied to the displacement field \mathbf{u} and the rotation field $\boldsymbol{\theta}$:

$$\tilde{\boldsymbol{\epsilon}} = \mathbf{B} \left\{ \begin{array}{c} \mathbf{u} \\ \boldsymbol{\theta} \end{array} \right\}$$

where

$$\mathbf{B} = \begin{bmatrix} \mathbf{B}_m & \mathbf{0} \\ \mathbf{B}_{sm} & \mathbf{B}_{sb} \\ \mathbf{B}_{bm} & \mathbf{B}_{bb} \end{bmatrix}$$

4.8 Numerical Examples

4.8.1 Free edge boundary-value problem. [45,-45]s

The first numerical simulation is a prismatic symmetric laminate having traction-free edges at $Y = \pm a$ and surfaces $Z = \pm h$, and loaded by strain applied only on its ends at $X = \text{constant}$. Each layer is composed of unidirectional fiber-reinforced material such that the fiber direction is defined by its angle θ with the X -axis.

The elastic properties of various composite materials used in this numerical simulation have been taken from Pagano [1989], p. 4. In this example a laminate consisting of four unidirectional fiberous composite layers, two with their axis of elastic symmetry (fiber direction) at $+45$ and two at -45 to the longitudinal laminate axis is considered. Figure 4.8 shows the laminate geometry and the coordinate system. 1% strain in opposite directions is applied at $X = -L$ and $X = L$ respectively, while it is restrained to move in the axial, lateral and thickness directions at $X = 0$. In order to solve this problem a finite element mesh comprising 1920 composite shell elements with 2665 nodes is generated. The physical dimensions for the numerical simulation are $X = 60$, $Y = 20$, $Z = 2.5$, with 12 elements in X direction, 40 elements in the Y direction and 4 elements through the thickness. For each finite element layer through the thickness, the reference surface is assumed to be associated with the bottom surface of the composite shell. We will be looking at a section cut at $X = 0$ for the displacement and the stress fields.

Figure 4.9 shows the axial displacement distribution at the top free surface of the section cut at $X = 0$, and the results are compared with Moires et al. and Pagano et al. [1989]. Figure 4.10 presents the interlaminar shear stress at material interface and their corresponding values from J.N. Reddy [1993]. Figure 4.11 shows the major stress components σ_{11} , σ_{12} , σ_{13} , and their corresponding values from the numerical simulations of Pipes et al. [1970]. In order to complete the discussion, we have also presented the minor stress components in Fig. 4.12.

4.8.2 Free edge boundary-value problem with a cylindrical hole. [45,-45]s

The composite laminate considered in this numerical simulation has the same physical dimensions, material properties and loading conditions as in the previous case. However the present laminate has a unit diameter cylindrical hole at (0,0,0) with the axis of the cylinder coincident with the Z axis (see Fig. 4.13). The ratio of the diameter of the hole to the width of the laminate is 0.1. To solve this problem a mesh containing 720 composite elements per finite element layer and with four layers through the thickness was generated. Total number of nodes in this problem are 3780. Traction-free boundary conditions are applied on the cylindrical surface of the hole. The laminate is constrained to move in the axial, lateral and transverse directions by appropriately constraining the nodes along the symmetry lines at $X = 0$.

Figure 4.14 presents the major stress components σ_{11} , σ_{12} , σ_{13} at a section cut at $X = 0$ in the top layer with +45 degrees ply orientation. These results have been compared with the 3D anisotropic calculations done with a mesh which is twice as refined as the composite mesh. It can be seen that close to the hole there is a sudden increase in the values of the stresses. In a region away from the free edge effects of the traction free boundary and the hole, the ratio of σ_{11} and σ_{12} agrees closely with that of the preceeding numerical simulation. Figure 4.15 shows the minor stress components which also show a good agreement with the results of the anisotropic 3D simulation.

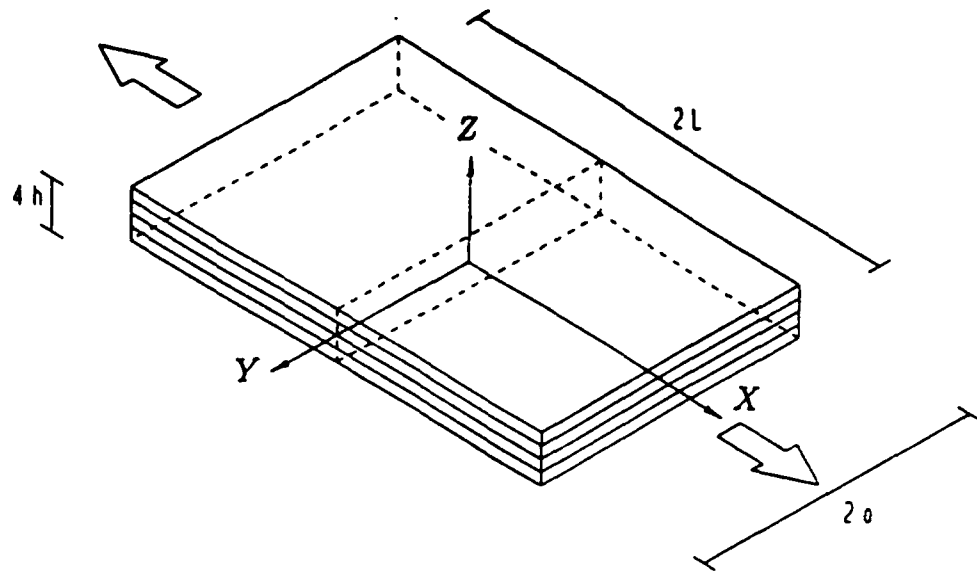


Figure 4.8 Laminate geometry and the coordinate system.

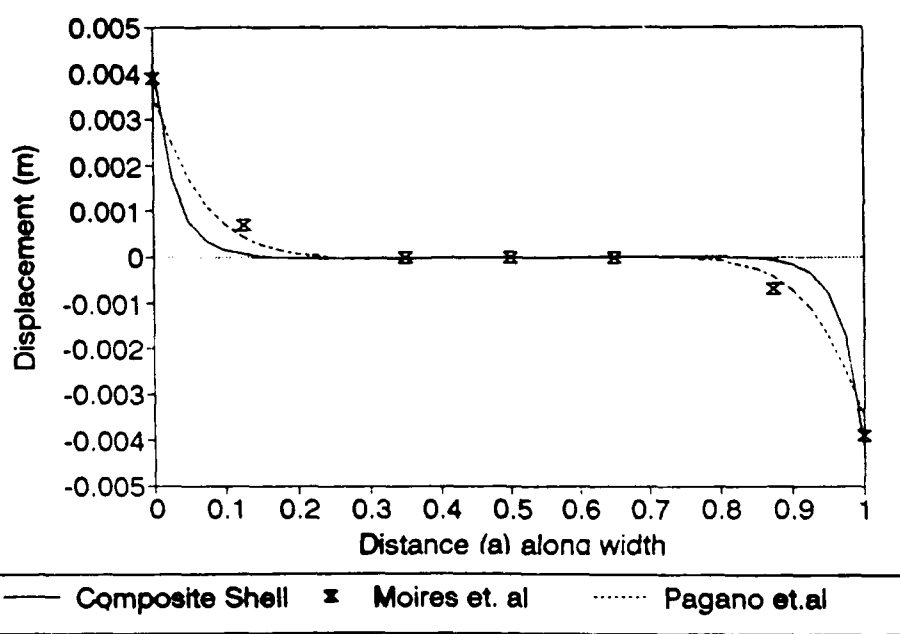


Figure 4.9 Axial displacement distribution at the top free surface.

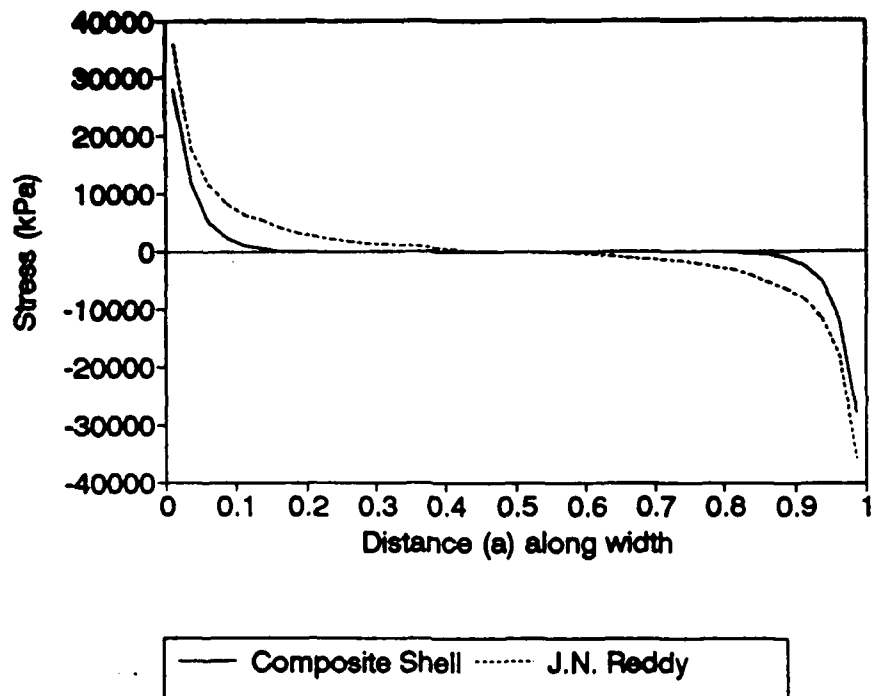


Figure 4.10 Interlaminar shear stress at material interface.

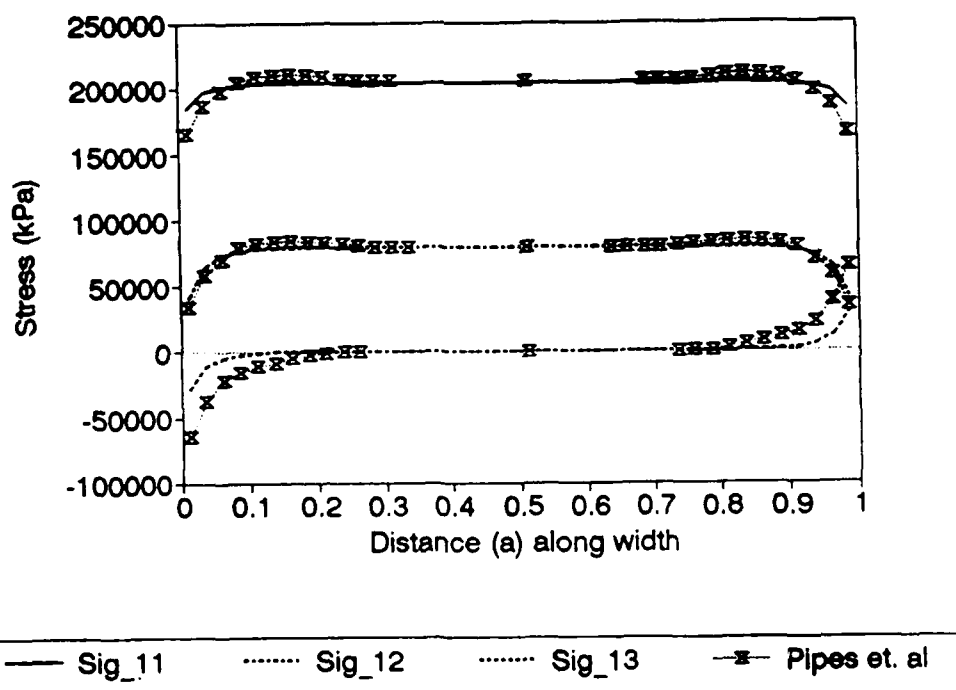


Figure 4.11 Major stress components in the top +45 laminate.

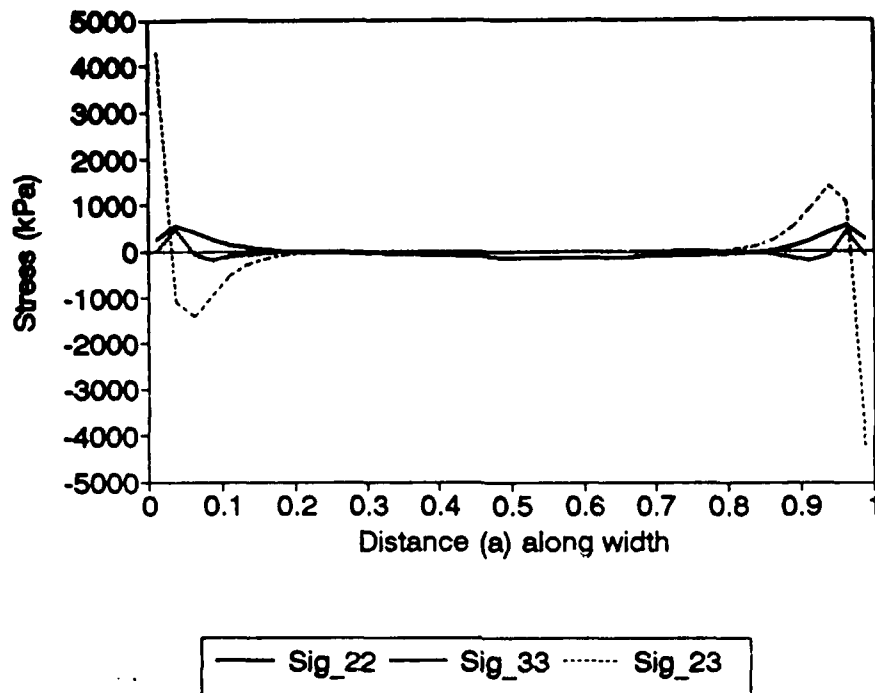


Figure 4.12 Minor stress components in the top +45 laminate.

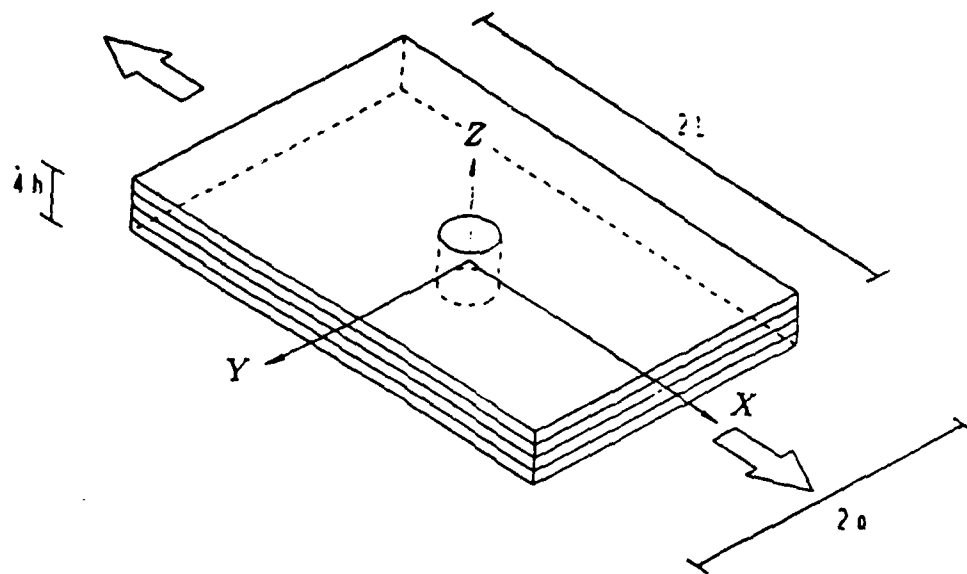


Figure 4.13 Laminate geometry with a cylindrical hole.

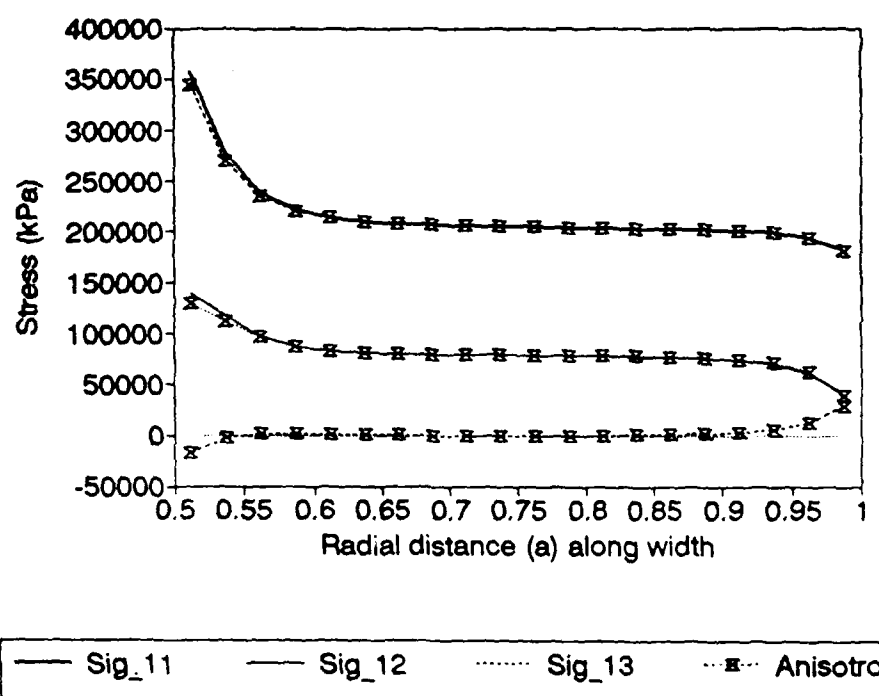


Figure 4.14 Major stress components in the top +45 laminate.

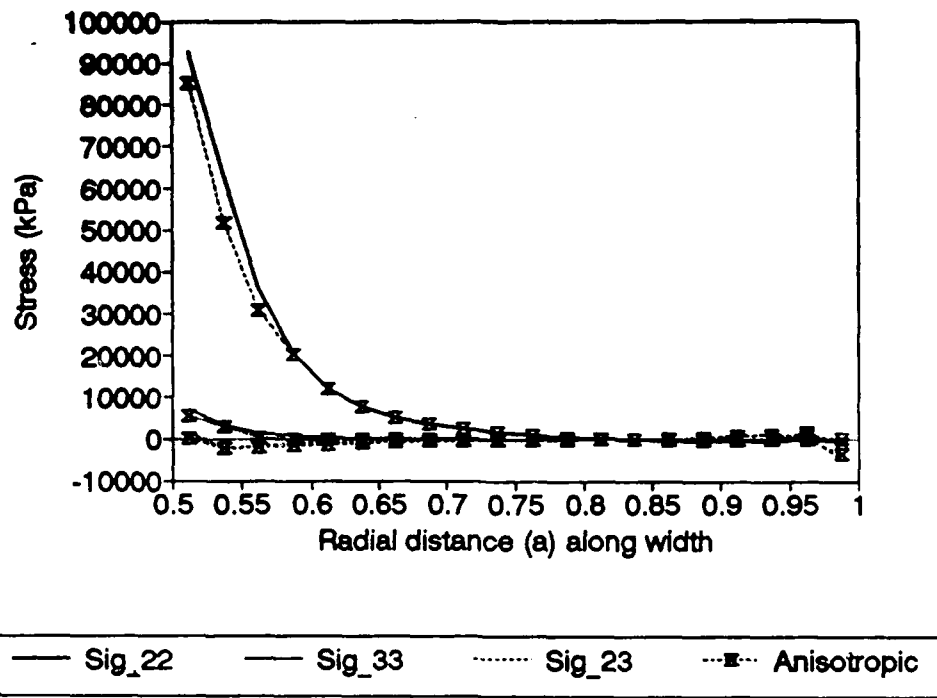


Figure 4.15 Minor stress components in the top +45 laminate.

4.9. Conclusions

In this chapter we have presented a finite element formulation which is suitable for the analysis of multi-director/multi-layered, shear-deformable flat composite laminates. The geometric description employed for the composite shells finds its roots in the so-called degenerated shell approach. A set of kinematic hypothesis is then introduced to accommodate the effects of transversal warping of the cross section due to shear deformation as well as fiber compressibility resulting from transverse normal stresses. The kinematics are individually and independently represented for each layer, and are coupled by the conditions of displacement continuity between the layers. The rotation field is layer-wise continuous and is discontinuous across the layers in the thickness direction. Transversal warping of the composite cross-section is described by individual layer directors which simultaneously rotate and stretch. This results in discontinuous strain fields across the different material sets, thereby creating the provision of stress continuity across the material interfaces. Since the formulation resolves all strains, all stresses are computed through the three-dimensional constitutive equations and the usual ‘zero normal stress’ shell hypothesis is not employed. The different material layers with arbitrary fiber orientations may occupy arbitrary layer locations in the composite. In this theory, at most, only first derivatives of displacement and rotation fields appear in the variational equations. The practical consequence of this fact is that only C^0 continuity of finite element functions is required which is readily satisfied by the family of Lagrange elements (Hughes [1987]). In displacement formulation of plates and shells, special attention needs to be given to transverse shear and membrane terms to prevent the occurrence of ‘mesh locking’. We have employed the selective reduced integration technique on membrane and transverse-shear terms to avoid this problem. Numerical results are presented to demonstrate the performance of the proposed theory.

The present theory is suited for the study of smart plate and shell structures with

embedded sensors and actuators. In particular the use of shape memory alloys in smart systems can be modeled through the present theory and the developments presented in Chapters 2 and 3.

CHAPTER 5

FUTURE RESEARCH AND POTENTIAL POST APPLICATIONS

It is expected that wide spread application of the intelligent materials technology using the present generation of actuators, sensors, processors, and control methods will occur. The breadth of application of this technology is expected to not only include the aerospace industry but to become widespread in the home construction, automotive, and machine tool industries as well.

At the present time, all of the technologies needed for cost-effective application of intelligent structures have not been sufficiently developed. There are a number of difficult problems which remain to be solved. In this section some of the more important of these problems are briefly discussed.

Actuation Materials: In order to truly achieve the desirable level of control for many structural applications, actuation materials which have 3 to 10 times larger strain than those currently commercially available must be developed, Crawley [1992], or materials should be developed similar to shape memory alloys, but with much higher bandwidth than those currently available. The proposed research work will provide a powerful analysis tool to study the optimum characteristics of these actuation materials.

Development of optimization algorithms in order to compute the most efficient sensor and actuators positions is another objective for the mathematical modeling of adaptive structures. Some of these optimal placement strategies can be based on finite element analysis output such as Independent Modal Space Control which utilizes the eigenvectors from a finite element modal analysis. The proposed work has the potential to be extended to study the optimal position of active elements in intelligent structures.

Many structural components in aerospace industry have curved geometries. The cou-

pling of in-plane and out-of-plane strain measures in these structures will affect the interaction between sensors/actuators and the host materials. In particular for the case of shape memory alloys with large actuation strains, the results of this research could be used to investigate the effect of curved geometries.

Further investigation on constitutive modeling of shape memory alloys under cyclic thermomechanical loadings with various preload conditions is needed for evaluation of the integrity of smart structural systems in the long term.

5.1 Potential Applications

Incorporating active materials into the structure of various aerospace vehicles will allow designers new flexibility with which to increase the vehicle performance. These performance enhancements will allow future aircraft systems to outperform their adversaries and better accomplish their missions. Potential applications for active structures span many disciplines including aerodynamics, propulsion, aeroelasticity, vibration and acoustics as discussed in Agnes & Silva [1992].

Aerodynamics applications for active structures technologies require changing structural contours of the aircraft to influence the airflow. Studies have shown that only small changes in airfoil shape can result in significant drag reduction. This application is similar to the Mission Adaptive Wing. Actuation requirements are for quasi-static control therefore shape memory alloys may prove best for this application.

Another possible aerodynamic application is the control of unsteady aerodynamics seen in either high angle of attack flight or in turbulent boundary layers. This application would require local changes in the airfoil skin that would interact with the unsteady airflow, reduce drag, and increase performance.

Another set of aerodynamic applications are in propulsion. Active flow field control could be used to keep combustion optimal in future engine designs. Active materials could

also be utilized in thrust vectoring nozzles to provide higher frequency control capability and lighter weight. Materials development will have to proceed these applications due to the high temperatures found in aircraft engines. The externals of engines, however, have lower temperatures, on the order to 300 – 400° F, and suffer from many vibration problems, particularly in the region of turbine rotor frequencies (30-100 Hz). Active damping of the external components could provide life cycle cost savings for propulsion systems.

Solution of the engine externals vibration environment would be similar to other structural dynamics applications in vibration, acoustics and aeroelasticity. The high vibratory environment of aircraft systems presents a range of challenges to the designer. Possible applications would include active isolation of stores, equipment, sensors, or pods; skin panel fatigue life extension; tail buffeting reduction, active landing gear and gun-fire vibration reduction. These and other vibration applications vary in frequency, bandwidth, temperature and control authority requirements. Solutions could involve active isolation, damping, control, or any combination of the three.

Another class of structural dynamics applications is aeroelastic. Coupling between the aerodynamic flow and structural dynamics can result in flutter. Active structures may be able to attack this problem from both directions: aerodynamic and structural. Novel control surfaces or active wing twisting may be possible. Direct active flutter control through wing twisting will require an increase in the control authority currently available from piezoceramics or an increase in the bandwidth of shape memory alloys.

Acoustic applications comprise the last subset of structural dynamic applications. Two areas which have been demonstrated are cabin noise reduction and cavity resonance problems. In summation, a wide array of aircraft applications for active structures technology exist; albeit at the conceptual stage. Further study in this area is therefore required, and this research is a step toward this direction.

REFERENCES

1. Abeyaratne, R., Knowles, J.K., (1993), "A continuum model of thermoelastic solid capable of undergoing phase transitions," *Journal of the mechanics and physics of solids*, 41, 541-571.
2. Agnes, G.S., Silva, K., (1992), "Aircraft Smart Structures Research in the USAF Wright Laboratory," AGARD 75.
3. Armero, F., Simo, J.C., (1991), "A new unconditionally stable fractional step method for nonlinear coupled thermomechanical problems," SUDAM Report No. 91-5, Stanford University. To appear in *Int. J. Num. Meth. Eng.*.
4. Auricchio, F., Lubliner, J., Taylor, R.L., (1993), "A Theory for Continua Undergoing Phase Transitions," University of California, Berkeley, Report No. UCB/SEMM-93/14.
5. Banks, R., Weres, O., (1976), *Shape Memory Effects in Alloys*, Plenum Press, New York.
6. Bell, J., Collela, P., Glaz, H., (1989), "A second-order projection method for the incompressible Navier-Stokes equations," *Journal of Computational Physics*, 85, 257-283.
7. Brandon, D., Rogers, R.C., (1992), "Constitutive laws for pseudo-elastic materials," *Journal of Intelligent Material Systems and Structures*, 3, 255-267.
8. Brezis, H., (1973), *Operateurs maximaux monotones et semi-groupes des contractions*, North Holland, Amsterdam.
9. Brinson, L.C., (1993), "One-dimensional constitutive behavior of shape memory alloys: Thermomechanical derivation with non-constant material functions and redefined martensite internal variables," *Journal of Intelligent Material Systems and Structures*, 4, 229-242.
10. Byun, C., Kapadia, R.K., (1992), "Prediction of interlaminar stresses in laminated plas-
tes using global orthogonal interpolation polynomials," *AIAA Journal*, vol. 20, no. 11.
11. Chang, F., Perez, J.L., Chang, K.Y., (1990), "Analysis of thick laminated composites," *Journal of composite materials*, vol. 24, pp. 801-822.
12. Chorin, A.J., Hughes, T.J.R., McCracken, M.F., Marsden, J.E., (1978), "Product for-
mulas and numerical algorithms," *Comm. Pure Appl. Math.*, 31, 205-256.
13. Christensen, R.M., (1979), "Mechanics of composite materials," John Wiley & Sons,
NY.
14. Cory, J.S., McNichols, J.R.Jr., (1985), "Nonequilibrium termostatics," *Journal of Ap-
plied Physics*, 58, 3282-3294.
15. Crawley, E.F., (1992), "Intelligent Structures, a Technology Overview and Assessment,"
AGRAD 75.

16. Cuitino, A., Ortiz, M., (1992), "A Material-Independent Method for Extending Stress Plasticity to Finite Plasticity with Multiplicative Kinematics," *Engineering Computations*, Vol. 9, 437-451.
17. Czarnek, R., Guo, Y., Bennet, K.D., Claus, R.O., (1988), "Interferometric measurements of strain concentrations induced by an optical fiber embedded in fiber reinforced composites." Proc. SPIE O/E Fiber Lase (Boston, MA).
18. Delaey, L, Krishnan, R.V., Tas, H., Warlimont, H., (1974), "Review - Thermoelasticity, pseudoelasticity and the memory effects associated with martensitic transformations - Part 2: The macroscopic mechanical behavior," *J. Mater. Sci.*, 9, 1536-1544.
19. Dong, S.B., Tso, F.K.W., (1972), "On a laminate orthotropic shell theory including transverse shear deformation," *Journal of Applied Mechanics*, vol. 39.
20. Eshelby, J.D., (1957), "The determination of the elastic field of an ellipsoidal inclusion, and related problem," *Proc. Roy. Soc. A*, 241, 376-396.
21. Eterovic, A. L., Bathe, K. J., (1990), "A hyperelastic-based large strain elasto-plastic constitutive formulation with combined isotropic-kinematic hardening using the logarithmic stress and strain measures," *Int. J. Num. Meth. Eng.*, 30, 1099-1114.
22. Falcioni, J. G., (1992), "Shape memory alloys," *Mech. Engrg.*, 114, 4.
23. Falk, F., Konopka, P., (1990), "Three-dimensional Landau theory describing the martensitic phase transformation of shape-memory alloys," *Journal of Physics: Condensed Matter*, 2, 61-77.
24. Fu, S., Muller, I., Xu, H., (1992), "The interior of psedoelastic hysteresis." *Mat. Res. Soc. Symp. Proc.* vol. 246.
25. Funakubo, H., (1987), *Shape Memory Alloys*, (translated from the Japanese by J. B. Kennedy), Gordon and Breach Science Publishers, New York.
26. Green, A.E., Naghdi, P.M., (1965), "A general theory fo an elastic-plastic continuum," *Arch. Rat. Mech. Anal.*, 18.
27. Grujicic, M., (1983), "Kinetic of martensitic interface motion," Ph.D. Thesis at MIT.
28. Hallquist, J.O., (1979), "NIKE2D: An implicit, finite deformation, finite element code for analyzing the static and dynamic response of two dimensional solids," Rept. UCRL-52678, Lawrence Livermore National Laboratory, University of California, Livermore, CA.
29. Hughes, T.J.R., (1983), "Numerical implementation of constitutive models: Rate independent deviatoric plasticity." Workshop on Theoretical Foundations for Large-scale Computations of Nonlinear Material Behavior, Northwestern University, Evanston, IL.
30. Hughes, T.J.R., (1987), "The finite element method: linear static and dynamic finite element analysis," Prentice-Hall, Englewood Cliffs, NJ.

31. Hughes, T.J.R., Pister, K., (1978), "Consistent linearization in mechanics of solids and structures," *Comput. & Struct.*, 8, 391-397.
32. Huo, Y., Muller, I., (1993), "Nonequilibrium Thermodynamics of Pseudoelasticity," *Continuum Mechanics and Thermodynamics*.
33. Ivshin, Y., Pence, J., (1993a), "A constitutive model for hysteretic phase transition behavior," *International Journal of Engineering Science*, to appear.
34. Ivshin, Y., Pence, J., (1993b), "A Simple mathematical model of two-way memory effect," in *Proceedings of the International Conference on Martensitic Transformations (ICOMAT)*.
35. Jensen, D.W., Pascual, J., August, J.A., (1992), "Performance of Graphite Bis-maleimide Laminates with Embedded Optical Fiber," *Smart Materials and Structures*, Vol. 1, No. 1.
36. Jones, R.M., (1975), "Mechanics of composite materials," McGraw-Hill Book Co., NY.
37. Kleiber, M., (1975), "Kinematics of deformation processes in materials subjected to finite elastoplastic strains," *Internat. J. Engrg. Sci.*, 13, 513-525.
38. Krieg, R.D., Krieg, D.B., (1977), "Accuracies of numerical solution methods for the elastic- perfectly plastic model," *Journal of Pressure Vessel Technology, Transaction of ASME*, 510.
39. Kroner, E., Teodosiu, C., (1972), "Lattice defect approach to plasticity and viscoplasticity," in *Problems of Plasticity*, A Sawczuk, ed., (Noordhoff, Leyden).
40. Lazarus, K.B., Napolitano, K.L., (1993), "Smart Structures, an Overview," Flight Dynamics Directorate Report WL-TR-93-3101.
41. Lee, E.H., (1969), "Elastic-plastic deformation at finite strains," *J. Appl. Mech.*, 36.
42. Lee, E.H., Liu, D.T., (1967), "Finite strain elastic-plastic theory particularly for plane wave analysis," *J. Appl. Phys.*, 38.
43. Lekhnitskii, S.S., (1981), "Theory of elasticity of an anisotropic body," Mir Publishers, Moscow.
44. Liang, C., Rogers, C.A., (1990), "One-dimensional thermomechanical constitutive relations for shape memory materials," *Journal of Intelligent Material Systems and Structures*, 1, 207-234.
45. Liang, C., Rogers, C.A., (1992), "A multi-dimensional constitutive model for shape memory alloys," *Journal of Engineering Mechanics*, 26, 429-443.
46. Liu, L.S., (1992), "On interface equilibrium and inclusion problems," *Cont. Mech. Thermodyn.*, 4, 177-186.
47. Lubliner, J., (1984), "A maximum-dissipation principle in generalized plasticity," *Acta Mechanica*, 52, 225-237.

48. Lubliner, J., (1993), "Generalized plasticity theory," unpublished work.
49. Maenchen, G., Sack, S., (1964), "The tensor code," Methods in computational physics (B. Alder, ed.), vol. 3, Academic Press, p. 181.
50. Marsden, J., (1973), "On Product Formulas for Nonlinear Semigroups," *Journal of Functional Analysis*, 13, 51-72.
51. Moran, B., Ortiz, M., Shih, C.F., (1990), "Formulation of implicit finite element methods for multiplicative finite deformation plasticity," *Int. J. Num. Meth. Eng.*, 29, 483-514.
52. Muller, I., Xu, H., (1991), "On the pseudo-elastic hysteresis," *Acta metallurgica et materialia*, 39, 263-271.
53. Nagtegaal, J.C., DeJong, J.E., (1981), "Some computational aspects of elastic-plastic large strain analysis," *Int. J. Num. Meth. Engrg.*, 17.
54. Nagtegaal, J., (1982), "On the implementation of inelastic constitutive equations with special reference to large deformation problems," *Comp. Meth. Appl. Mech. Engrg.*, 33, 469-484.
55. Noor, A.K., Burton, W.S., (1989), "Assessment of shear deformation theories for multi-layered composite plates," *Applied Mechanics Review*, vol. 42, no. 1, pp. 1-13.
56. Noor, A.K., Burton, W.S., (1990), "Assessment of computational models for multilayered composite shells," *Applied Mechanics Review*, vol. 43, no. 4.
57. Olson, G.B., Cohen, M., (1980), "Dislocation theory of martensitic transformations," in *Dislocations in solids*, N. Nabarro (ed.), North-Holland Publ., Amsterdam.
58. Ortiz, M., Martin, J.B., (1989), "Symmetry-preserving return mapping algorithms and incremental external paths: A unification of concepts," *Int. J. Num. Meth. Engrg.*, 28, 1839-1853.
59. Ortiz, M., Pinsky, P.M., Taylor, R.L., (1983), "Operation split methods for the numerical solution of the elastoplastic dynamic problem," *Comp. Meth. Appl. Mech. Engrg.*, 39, 137-157.
60. Ortiz, M., Popov, E., (1985), "Accuracy and stability of integration algorithms for elasto-plastic constitutive relations," *Int. J. Num. Meth. Engrg.*, 21, 1561-1576.
61. Pagano, N.J., (1989), "Interlaminar response of composite materials," Composite Materials Series, vol. 5, Elsevier, NY.
62. Pagano, N.J., Pipes, R.B., (1973), "Some observations on the interlaminar strength of composite laminates," *Int. J. Mech. Sci.*, vol. 15, p. 679.
63. Panahandeh, M., Masud, A., Ghanimati, G.R., (1993), "Development of an advanced continuum theory for composite laminates," Technical report prepared by Berkeley Applied Science and Engineering, Inc. for AFOSR.

64. Patoor, E., Eberhardt, A., Berveiller, (1988), "Thermomechanical behaviour of shape memory alloys," *Archives of Mechanics*, 40, 755-794.

65. Perkins, J., Edwards, G.R., Such, C.R., Johnson, J.M., Allen, R.R. (1976), "Thermo-mechanical characteristics of alloys exhibiting martensitic thermoelasticity," in *Shape Memory Effects in Alloys*, (edited by J. Perkins), Plenum Press, New York.

66. Pinsky, P. M., Ortiz, M., Taylor, R.L., (1983), "Operator split methods for the numerical solution of the finite deformation elastoplastic dynamic problem," *Comp. & Structure*, 13, 345-359.

67. Pipes, R.B., Pagano, N.J., (1970), "Interlaminar stresses in composite laminates under uniform axial extension," *J. Comp. Material*, vol. 4, p. 538.

68. Reddy, J.N., (1984), "A simple higher-order theory for laminated composite plates," *Journal of Applied Mechanics*, vol. 51, pp. 745-752.

69. Reddy, J.N., (1984), "A refined nonlinear theory of plates with transverse shear deformation," *Int. J. Solid Struct.*, vol. 20, pp. 881-896.

70. Robbins, D.H., Reddy, J.N., Murty, A.V.K., (1991), "On the modelling of delamination in thick composites." in Enhanced Analysis Techniques for Composite Materials, ed. L. Schwer, J.N. Reddy and A. Mal, at The Winter Annual Meeting of the American Society of Mechanical Engineers, Atlanta, Georgia.

71. Rogers, C. A., Liang, C., Jia, J., (1989), "Behavior of shape memory alloy reinforced composite plates - Parts I and II," in *Proceedings of the 30th Structures, Structural Dynamics and Materials Conference*, Mobile, Alabama, 3-5 April, pp. 2011-2017.

72. Rogers, C.A., Robertshaw, H.H., (1988), "Shape Memory Alloy Reinforced Composites," Engineering Science Preprints.

73. Simo, J.C., (1988a,b), "A framework for finite strain elastoplasticity based on maximum plastic dissipation and multiplicative decomposition: Part I. Continuum formulation; Part II. Computational aspects," *Comp. Meth. Appl. Mech. Eng.*, 66, 199-219 and 68, 1-31.

74. Simo, J.C., Armero, F., (1992), "Recent advances in the formulation and numerical analysis of thermoplasticity at finite strains," *Finite Inelastic Deformations: Theory and Applications, IUTAM Symposium, Hannover 1991*, ed. by D. Besdo and E. Stein, Springer Verlag, Berlin.

75. Simo, J.C., Govindjee, S., (1991), "Non-linear B-stability and symmetry preserving return mapping algorithms for plasticity and visco-plasticity," *International Journal for Numerical Methods in Engineering*, 31.

76. Simo, J.C., Miehe, C., (1991), "Coupled associative thermoplasticity at finite strains. Formulation, numerical analysis and implementation," *Comp. Meth. Appl. Mech. Eng.* (in press).

77. Simo, J.C., Hughes, T.J.R., (1993), "Elasto-plasticity and visco-plasticity: computational aspects," Springer-Verlag.
78. Simo, J.C., Ortiz, M., (1985), "A unified approach to finite deformation elastoplastic analysis based on the use of hyperelastic constitutive equations," *Comp. Meth. Appl. Mech. Eng.*, 49, 221-245.
79. Simo, J.C., Taylor, R.L., (1983), "Penalty function formulations for incompressible non-linear elastostatic," *Comp. Meth. Appl. Mech. Eng.*, 35, 107-118.
80. Simo, J.C., Taylor, R.L., Pister, K.S., (1984), "Rate independent finite deformation plasticity: Computational issues," Paper presented at FENOMECH-84.
81. Singh, H., Sirkis, J.S., Dagsputa, A., (1991), "Micro-interaction of Optical Fibers Embedded in Laminated Composites," SPIE Vol. 1588, Fiber Optic Smart Structures and Skins.
82. Tanaka, K., (1986), "A thermomechanical sketch of shape memory effect: one-dimensional tensile behavior," *Res. Mechanica*, 18, 251-263.
83. Tanaka, K., Hayashi, T., Itoh, T., Tobushi, H., (1992), "Analysis of thermomechanical behavior of shape memory alloys," *Mechanics of Materials*, 13, 207-215.
84. Tanaka, K., Iwasaki, R., (1985), "A phenomenological theory of transformation superplasticity," *Engineering Fracture Mechanics*, 21, 709-720.
85. Tanaka, K., Nagaki, S., (1982), "A thermomechanical description of materials with internal variables in the process of phase transitions," *Engineering Fracture Mechanics*, 21, 709-720.
86. Tobushi, H., Iwanaga, H., Tanaka, H., Hori, T., Sawada, T., (1991), "Deformation behavior of tini shape memory alloy subjected to variable stress and temperature", *Continuum mechanics and thermodynamics*, 3, 79-93.
87. Wayman, C.M., (1980), "Some applications of shape-memory alloys," *J. Metals*, 32, 129-137.
88. Wayman, C.M., (1992), "Shape memory and related phenomena," *Progress in Material Science*, 36, 203-224.
89. Wayman, C.M., Duerig, T.W., (1990), "An introduction to martensite and shape memory," in *Engineering Aspects of Shape Memory Alloys*, (edited by T.W. Duerig, K.N. Melton, D. Stockel and C. M. Wayman), pp. 3-20, Butterworth-Heinemann, Boston.
90. Whitney, J.M., (1987), "Structural analysis of laminated anisotropic plates," Technomic Publishing Company, Inc., PA.
91. Whitney, J.M., Pagano, N.J., (1970), "Shear deformation in heterogeneous anisotropic plates," *J. App. Mech.*, vol. 37, p. 1031.
92. Wilkins, M.L., (1964), "Calculation of elastic plastic flow," *Methods in computational physics*, (B. Alder, ed.), vol. 3, Academic Press, p. 211.
93. Wilmanski, K., (1993), "Symmetric model of stress-strain hysteresis loops in shape memory alloys," *International Journal of Engineering Science*, 31, 1121-1138.